INAUGURAL-DISSERTATION
zur Erlangung der Doktorwürde
der
Naturwissenschaftlich-Mathematischen
Gesamtfakultät
der Ruprecht-Karls-Universität
Heidelberg

vorgelegt von
Dipl.-Phys., MPhys Markus Christopher Kohler
geboren in Karlsruhe, Deutschland
Tag der Disputation: 29.06.2011

Frontiers of High-Harmonic Generation

Referees: **Prof. Dr. Christoph H. Keitel**
Prof. Dr. Dirk Dubbers

Zusammenfassung

In der vorliegenden Arbeit wird die Erzeugung von Höheren Harmonischen (HHG) theoretisch untersucht mit dem Ziel, das grundlegende Verständnis zu erweitern und gegenwärtige Hürden zu überwinden. Im Rahmen dessen werden Vorschläge erarbeitet, HHG zu höheren Photonenergien hin zu entwickeln und Röntgenpulse mit Pulslängen bis in den Zeptosekundenbereich zu erzeugen. Dafür werden Möglichkeiten diskutiert, Photonen mit mehreren Kilo-Elektronenvolt Energie mit Hilfe von relativistischen Laserintensitäten zu erzeugen und dabei sowohl das relativistische Drift- als auch das Phasenanpassungproblem zu überwinden. Eine andere Möglichkeit, die hochmoderne Attosekundenphysik in den Röntgenbereich zu überführen, ist das Atom während der Exkursion des Elektrons zu manipulieren. Dafür wird ein tieferliegendes Elektron kohärent angeregt, um dem Kontinuumelektron zu ermöglichen, in das frei gewordene Loch mit höherer Bindungsenergie zu rekombinieren. Auf der anderen Seite ist HHG die Technologie, mit der die kürzesten kohärenten Lichtpulse überhaupt erzeugt werden können. Problematisch ist jedoch, dass diese Pulse intrinsisch nicht bandbreitenbegrenzt emittiert werden. Es wird eine Methode vorgeschlagen, mit der bandbreitenbegrenzte harmonische Pulse erzeugt werden können mit möglichen Pulslängen unter einer Attosekunde. In einer grundlegenderen Arbeit wird HHG in einem Interferenzbild diskutiert. Innerhalb des Bildes können alle Übergänge, die zu HHG führen als Interferenz zweier Wellenpakete im Bindungspotential gesehen werden. Dabei wird die Differenzenergie der beiden Wellenpakete emittiert. Darüberhinaus wird ein neuartiger Kontinuum-Kontinuum Übergang untersucht und dessen Bedeutung im Sättigunsregime aufgezeigt.

Abstract

High-harmonic generation (HHG) is investigated theoretically aiming to improve its fundamental understanding and overcome current limitations. In the course of this, HHG is extended to higher energies and used to generate x-ray pulses with durations down to the zeptosecond regime. To this end, a route is discussed to generate multi-kilo-electronvolt harmonics with relativistic laser intensities circumventing both the phase-matching problem and relativistic drift. In a different approach, the state-of-the art attosecond science is transferred to the x-ray regime by manipulating the atom during the excursion of the continuum electron. By coherently exciting a core electron, the continuum electron is forced to recombine with the core hole with a much higher binding energy. HHG is the cutting-edge technology allowing for the creation of the shortest coherent light flashes of all. However, particularly problematic is the intrinsic chirp of the HHG light that requires the use of optical elements to compensate it. For this purpose, the harmonic generation process is altered such that chirp-free pulses are generated with possible pulse duration below one attosecond. Moreover, in a more fundamental work, the HHG process is set into the framework of a unified interference picture. In that picture, all possible HHG transitions can be viewed as an interference between two wave packets in the binding potential leading to photoemission at their difference energy. A novel continuum-continuum transition is studied and its importance in the saturation regime is pointed out.

Within the framework of this thesis, the following articles were published in refereed journals:

- M. C. Kohler, M. Klaiber, K. Z. Hatsagortsyan, C. H. Keitel,
  Phase-matched coherent hard x-rays from relativistic high-order harmonic generation,
  Euro. Phys. Lett. **94**, 14002 (2011), arXiv: 1008.0511.

- M. C. Kohler, C. H. Keitel, K. Z. Hatsagortsyan
  Attochirp-free high-order harmonic generation,
  Opt. Express **19**, 4411-4420 (2011), arXiv: 1101.5885.

- M. C. Kohler, C. Ott, P. Raith, R. Heck, I. Schlegel, C. H. Keitel, T. Pfeifer,
  High harmonic generation via continuum wave-packet interference,
  Phys. Rev. Lett **105**, 203902 (2010), arXiv: 1007.1308.

- C. Liu, M. C. Kohler, K. Z. Hatsagortsyan, C. Müller, C. H. Keitel,
  Laser-guided relativistic quantum dynamics,
  New J. Phys. **11**, 105045 (2009).

- C. Müller, K. Z. Hatsagortsyan, M. Ruf, S. J. Müller, H. G. Hetzheim, M. C. Kohler, C. H. Keitel,
  Relativistic nonperturbative above-threshold phenomena in strong laser fields,
  Laser Physics **19**, 1743-1752 (2009).

- K. Z. Hatsagortsyan, M. Klaiber, C. Müller, M. C. Kohler, Christoph H. Keitel,
  Laser-driven relativistic recollisions,
  J. Opt. Soc. Am. B **25**, B92-B103 (2008).

Articles submitted for publication in refereed journals:

- C. Buth, M. C. Kohler, J. Ullrich, C. H. Keitel,
  Novel light from high-order harmonic generation manipulated by XUV light,
  submitted (2011), arXiv: 1012.4930.

Articles in preparation:

- M. C. Kohler, C. H. Keitel, K. Z. Hatsagortsyan,
  Phase-matched relativistic high-order harmonic generation

- M. C. Kohler, C. H. Keitel, K. Z. Hatsagortsyan,
  Enhancing spectral windows in HHG spectra via wave-packet engineering

- C. Buth, M. C. Kohler, C. H. Keitel,
  High-order harmonic generation for x-ray free electron laser-induced Rabi flopping

Unrefereed publications:

- M. C. Kohler and K. Z. Hatsagortsyan,
  Relativistic high-order harmonic generation,
  Modern Optics and Photonics, Conf. Proceed. edited by G. Y. Kryuchkyan, G. G. Gurzadyan, A. V. Papoyan, 2010.

Contents

1 Introduction

The photon can be seen in many regards as an engine of technological progress for the 21st century [1, 2] — a success story that began with the advent of lasers about 50 years ago [3]. Technology has continuously developed and lasers have become an important tool in industry and in almost every physics laboratory, independent of its field of research. Besides other parameters, the achievable laser intensities are a significant means to depict the progress in laser technology. The first lasers in the 1960s exhibited intensities well below $10^{10}\,\mathrm{W/cm^2}$ [4]. An enormous interest of the scientific community in this tool and vivid research led to rapid progress of the highest laser intensities that can be obtained. Employing techniques as, e.g., chirped-pulse amplification [5] make it nowadays possible to create laser pulses [6,7] with peak intensities of $10^{22}\,\mathrm{W/cm^2}$ [8]. Intensities of more than $10^{24}\,\mathrm{W/cm^2}$ are envisaged for the upcoming *Extreme Light Infrastructure* (ELI) [9] within the next decade, with probable impact on many areas in physics such as laser plasma acceleration [10–12], laser fusion ignition [13], nuclear [14] and particle [15, 16] physics with lasers. Besides the high peak intensities, pulse durations down to only a single cycle have also been achieved [17–19], the carrier envelope phase can be stabilized [20,21], lasers have become more reliable and are available at a variety of wavelengths.

With the invention of the laser, a bright coherent light source became available that led to a renaissance in the field of optics, e.g., with the birth of the entirely new field of perturbative non-linear optics [22, 23]. *Perturbative* means that the energies exerted by the laser field are small compared to other transition energies in the system and can be treated simplify by perturbation theory, i.e., $E\,a/\Delta \ll 1$ where E is the laser field strength, a a typical atomic distance and Δ is the detuning. This branch of optics has motivated optical elements [23] that have become indispensable in modern laser technology. Lasers also had a huge impact on atomic physics, especially, when the laser field strengths became comparable with the electric field experienced by a bound electron in an atom happening in the 1980s. At that point, the non-perturbative regime was entered where the average electron energy in the laser field U_p is much larger than the binding potential I_p, i.e., $U_p/I_p \gg 1$, demanding an advanced theoretical treatment. Fields with such a strength are able to significantly change the electronic dynamics of atoms and molecules. In particular, large fractions of the electronic wave function can be transferred to the continuum. A number of new effects were discovered at that time, for instance, above-threshold ionization (ATI) [24], i.e., electrons tunnel-ionized by an IR-field were detected with a large kinetic energy. Moreover, recollisions of those electrons with the core were observed, leading either to the knock-out of a second electron, the non-sequential double ionization [25, 26], or to recombination along with the emission xuv light, called high-harmonic generation (HHG) [27] — the main process under consideration in this thesis.

HHG was discovered in 1987 [27]: a rare gas illuminated by a laser emitted photons

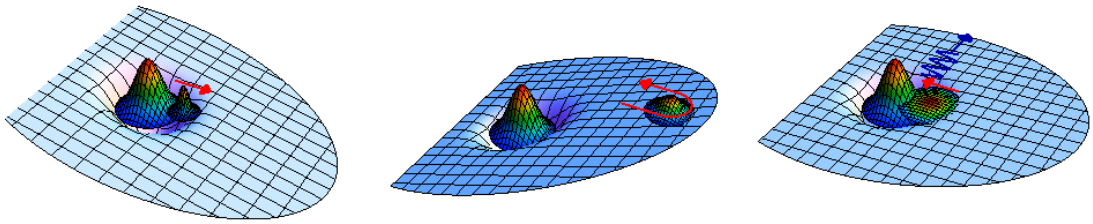

Figure 1.1: Schematic of the three-step model for the HHG process. The blue surface is the superposition of the atomic binding potential and the electrostatic potential of the laser field. The bound and continuum part of the wave function are rainbow-colored. A tiny part of the wave function (continuum part) is just freed and subsequently driven away. When the laser field reverses its sign, the continuum part is stopped and accelerated back towards the core. At recollision both parts of the wave function interfere and give rise to coherent photon emission denoted by the blue wiggled line.

with an energy of several odd multiples of the laser frequency. Remarkably, the emission spectrum exhibited a plateau-like structure extending far until a sudden cutoff rather than a continuous exponential decrease typical for perturbative non-linear processes. This rapidly led to a vivid discussion about the physical origin of the phenomenon and was eventually explained in 1993 [28, 29] with the three-step model (see Fig. 1.1). i) the electronic wave function of an atom is partially freed by a strong laser field, ii) then the ionized fraction is subsequently driven away in the continuum by the laser field, iii) finally, the wave packet is accelerated back to the ionic remnant, interfering with the bound part of the wave function giving rise to a strong, coherent, high-frequency response that can lead to the emission of a HHG photon along with the recombination of the electron into the bound state.

HHG is fascinating both from being a fundamental example of laser-atom dynamics and from a technological point of view, allowing one to create light flashes with exceptional properties: the energy of an emitted HHG photon is the sum of the binding energy and the kinetic energy acquired in the laser field. The photon energy can be extremely large reaching several kilo-electronvolts (keV) [30]. In a world where technology is currently miniaturizing, x-rays with their tiny wavelengths may become the light of the future and thus HHG of particular importance. Another property of HHG is its coherence, meaning that the phase is locked to the laser phase [31] and under optimal conditions the harmonic yield scales quadratically with the number of contributing atoms. The last point indicates that the process cannot be viewed only from a single-atom perspective. It is crucial for the emission that all atoms are phase-matched meaning that harmonics from different atoms have to emit with the same phase to allow for constructive interference between them. Moreover, the harmonic spectrum contains structural signatures of the emitting atom or molecule which can be assessed by measuring the spectrum [32–36]. Nowadays most importantly, the frequency up-conversion of the laser field makes the harmonics attractive for the generation of light bursts much shorter than the laser pulse duration. The harmonic pulses [37, 38] can have durations down to the attosecond regime [39–41].

Attoseconds is the time scale of electron dynamics in atoms and ions. For a long time, no tools have been available that were fast enough to resolve such dynamics. For this reason, HHG has become a key process in atomic and molecular physics and a state-of-the-art coherent light source being nowadays available in many research laboratories. With the emergence of extremely short pulses from HHG, an entirely new pathway in exploring and controlling the physics of atoms and ions [37, 42–45] was opened and HHG has become the most important tool for the field of attosecond physics.

A powerful scheme for time-resolved measurement relies on the pump-probe technique. A first pulse excites the system whereas the second pulse probes its properties. It has proven its strength in various experiments mainly for exploring fragmentation [46, 47] and vibrational [48] and chemical dynamics [49, 50] in molecules. In these experiments the time scales were femtoseconds and the excitation energies meV/few eV achievable by employing ultrashort lasers. To access systems with attosecond precision, pump-probe schemes with IR and attosecond pulses can be realized. The so-called streaking technique [51] is often employed where the IR and attosecond pulses overlap and the emitted photo-electron momentum spectrum is measured depending on the relative delay between the two pulses. The emitted photoelectron spectrum is measured allowing one to retrieve temporal information about the physical process under consideration. The technique renders it possible to characterize both IR [52] and attosecond pulses [39, 40, 53] and even to examine time-resolved inner-shell atomic dynamics [54]. In the early days of attosecond physics in 2002 [55], the characteristic Auger decay time in krypton was directly measured. Moreover, the temporal dynamics of tunneling was also investigated [56], time delays were measured between photoelectrons from the delocalized conduction band and the localized core states in solid-state tungsten [57] and it has been proposed to map the vibrations of nuclear wave packets in a molecule employing reaction microscopes [58–61]. Furthermore, the authors of [62] elaborate on the idea of measuring electron correlation in helium by means of attosecond pulses.

All these schemes require HHG that is state-of-the-art limited to energies around a few hundred eV and to pulse durations of several tens of attoseconds. An advancement of HHG to higher energies is highly desirable because it would allow one to investigate systems with higher energies such as, e.g., nuclear excitations [63], tightly bound core electrons or even time-resolved diffraction imaging [64] with sub-Ångström resolution. Even more important, the larger harmonic bandwidth would be necessary to generate pulses down to the zeptosecond regime and to resolve much faster processes than currently possible.

In principle, with free electron lasers (FEL), bright sources of soft and hard x-rays are at hand, but the radiation is limited in coherence and occurs typically in pulses in the femtosecond regime. Moreover, the large scale of these machines and costs allow only a limited number of experiments. It would be very attractive to extend the table-top HHG source to the hard x-ray domain and to pulse durations of a few atto- or zeptoseconds.

The straightforward way to increase the laser intensity in order to achieve higher HHG energies is not possible because soon the relativistic interaction regime above $10^{16}\,\mathrm{W/cm^2}$ is reached. Then the magnetic component of the laser field becomes relevant because of the high electron velocities in this regime and gives rise to a drift motion of the electron due to the Lorentz force [65–69] prohibiting recollision of the electron and HHG this way. Additionally, it is crucial for an efficient emission from a macroscopic gas target

that all atoms emit with the same phase. To achieve the so-called phase-matching, the phase front of the laser that triggers HHG and the phase front of the harmonic have to propagate at the same speed. However, because of the strong laser field, a large amount of the electrons is ionized leading to an enormous plasma dispersion prohibiting phase-matching. This is especially problematic because the phase fronts need to match on the tiny length scale of the HHG wavelength. Generating relativistic harmonics means overcoming both problems simultaneously. So far, only the relativistic drift problem has been addressed [67, 68, 70–83]. Neither problem has been tackled simultanously nor any quantitative analysis of the HHG yield from a macroscopic gas target in this regime has been drawn.

A few other methods were proposed to increase the maximum photon energy of HHG for a given non-relativistic laser intensity: First, the nonsequential double recombination in helium can lead to a second plateau with about 12 orders of magnitude lower yield than the primary HHG plateau [84]. Second, two-color HHG (optical plus UV) was studied theoretically in a one-electron model where the UV assists the ionization process leading to an overall increased yield [85–90], improved phase-matching [89], a suppressed relativistic drift [82, 91] and the emergence of a new plateau with larger energy [92, 93], the latter, however, at a much lower yield. Third, by femtosecond pulse shaping that was used to alter the HHG spectrum [94] or for relativistic HHG [80, 81], also the quantum path of the electron can be optimized. The HHG cutoff is increased by a factor of 2.5 [95, 96] this way. However, an efficient method to generate multi-keV harmonics is currently missing.

Doubtless, the most important property of HHG pulses is their duration. To allow for measurement of even faster processes, tremendous effort is exerted to shorten the pulse duration. Today, pulses with durations of several tens of attoseconds [39–41] have been demonstrated but harmonic bandwidths are available that would allow to synthesize pulses down to 10 as [97]. However, the nature of the harmonic generation is such that the created pulses are intrinsically chirped [98, 99]. To compensate this so-called attochirp, mainly filter elements of thin metal foils [100, 101] have been used suffering from losses, depending on the material properties and lacking in flexibility. It will be difficult to find filters with suitable dispersion properties, especially, for the large harmonic bandwidths that can hopefully be generated in the future. An alternative route to overcome the attochirp problem is highly desired.

A fundamental discussion of the HHG process is the first part of this thesis. The interference picture of HHG is unified to include contributions to the photon emission arising from continuum wave packets. Additionally, HHG at laser intensities large enough to ionize the entire wave function is examined and shown to be dominated by an unpredicted mechanism. In the second part of this thesis, several chapters are devoted to the current limitations in the highest harmonic photon energies and shortest harmonic pulses achievable. New routes are presented in order to overcome these limitations.

This thesis starts with elucidating the fundamental principles of the HHG process in Chapter 3. In a quantum mechanical description, the photon emission is caused by the interference of the recolliding wave packet with the portion of the wave function still being bound to the atom [33, 102]. Not included in this picture, the continuum wave

packet dynamics in the vicinity of the ionic remnant can also lead to HHG which is named continuum–continuum (CC) transition. CC transitions in atomic HHG have been studied before, restricted to the special cases of Bremsstrahlung emission from single wave packet recolliding with a bare core [103] and the interaction of a continuum wave packet ionized just shortly before the recollision time [104–108]. The former solely leads to low energy photon emission, the latter is weak and indistinguishable from the traditional HHG spectrum. Thus, both CC transitions are of minor importance.

In the present work it is pointed out that any two wave packets interfering in the core region lead to photon emission at their difference energy. This picture includes the three previously described HHG mechanisms but also a novel CC transition caused by two simultaneously recolliding continuum wave packets that were ionized from different half cycles. Remarkably, this transition can dominate over the standard HHG mechanism and is shown to be distinguishable via phase-matching. The transition is described within a numerical and an analytical framework with excellent agreement. It is pointed out that the spectrum contains new signatures which could be used to gain structural information about the emitting atom or molecule.

After this fundamental discussion of HHG, new strategies are developed to put forward this cutting edge technology, to achieve even shorter light pulses by mastering the attochirp problem and to extend HHG to the hard x-ray domain.

In Chapter 4, the problem of generating relativistic harmonics is approached and an adequate theoretical treatment is developed to describe emission from a macroscopic gas target in this regime. We tackle both problems simultaneously: the phase-matching problem and the relativistic drift. Two field geometries are analyzed in the context of a macroscopic gas target of multiply-charged ions. First, HHG is investigated from counterpropagating, linearly polarized attosecond pulse trains capable of suppressing the relativistic drift [82, 83]. In the second setup, in addition to the conventional IR driving laser, x-ray assistance is employed to compensate for the relativistic drift [82, 91]. Both schemes are appropriately modified to allow for a phase-matched emission of relativistic harmonics. The calculations for both optimized setups reveal a small but detectable HHG photon yield.

As the previous straightforward approach to generate hard x-rays via relativistic laser intensities is experimentally very challenging, a different scheme is presented to reach coherent hard x-rays pulses in Chapter 5. The present-day theory of HHG largely gravitates around single-electron calculations. Multi-electron contributions can influence the HHG spectrum [109, 110] but have not been exploited to control HHG in a desired way. A two-electron scheme is presented where the manipulation of the second electron has a major impact on the emission spectrum creating a second high-energy plateau. As in the one-electron schemes of Refs. [85–90], the atom is manipulated with xuv/x-ray fields from FELs. In contrast to previous studies, the light is employed to force the continuum electron to recombine to a core level with a high binding energy instead of to the valence level. To do so, a second core electron is resonantly excited to the valence hole that is created when the continuum electron was ionized. The whole HHG spectrum is upshifted in energy and the entire field of attosecond science could be transferred into the x-ray regime.

In order to reach shorter harmonic pulse durations, the bandwidth of the harmonic spectrum needs to be increased but at the same time the increasing attochirp has to be compensated on a much shorter time scale. In Chapter 6, a new scheme is proposed to modify the HHG process in such a way that the harmonic pulses are emitted without attochirp. Therefore, an xuv/x-ray field is added to the driving IR laser light. The photon energy has to be larger than the binding energy in order to ionize the wave packet by a single photon with a large initial momentum. Additionally, the fundamental IR laser field is shaped by adding a small number of harmonics with a maximum order of around 10. By means of the two modifications of the HHG process, a wave packet is formed after ionization that spatially recompresses along the wave packet propagation direction and has its minimum width exactly at the time of recollision. Because of the short time interval of overlap between the compressed electronic wave packet and the parent ion, the emitted light pulse is of the same short duration. It is shown that with present techniques the emission of pulses in the zeptosecond regime is possible.

With the same setup but a different pulse shape, it is demonstrated that it is also possible to create a mono-energetic wave packet to enhance a certain defined energy in the HHG spectrum.

Throughout this thesis, we employ atomic units (a.u.) where the electron mass, the reduced Planck constant and the charge of the electron are $m = \hbar = -e = 1\,\text{a.u.}$, respectively and the speed of light is $c = 137\,\text{a.u.}$. $1\,\text{a.u.}$ in time corresponds to $24.2\,\text{as}$, $1\,\text{a.u.}$ in length is $0.5\,\text{Å}$ and $1\,\text{a.u.}$ energy is $27.2\,\text{eV}$.

2 Fundamental aspects of HHG

2.1 Three-step model and phenomenology

As this thesis is devoted to the advancement of the HHG process, the phenomenology of this process is explained in detail in this introductory section. One of the most successful and intuitive models of HHG is the three-step model [28, 29] (see Fig. 1.1): the strong laser field tunnel ionizes the atom. Once freed, the electron propagates in the continuum driven by the laser field. After the laser field has changed its direction, the electron is accelerated back towards its parent ion and can eventually recombine. An energetic photon is then emitted containing the ionization energy plus the entire kinetic energy of the electron gained from the laser field previously.

In the following, the main features of the harmonic generation process are explained from a more quantum mechanical point of view. Before the laser interacts with the atom the whole electronic wave function is bound to the atom. As soon as the laser field is turned on, tunnel ionization takes place and, continuously, parts of the electronic wave function are freed. The tunneled parts of the wave function are quickly accelerated by the laser field in a one-dimensional motion along the polarization directions. The continuum evolution of the wave function can be viewed as a superposition of a bunch of classical trajectories [see Fig. 2.1 (a)] starting with nearly zero velocity.The weight of each trajectory has to be deduced from quantum mechanics.

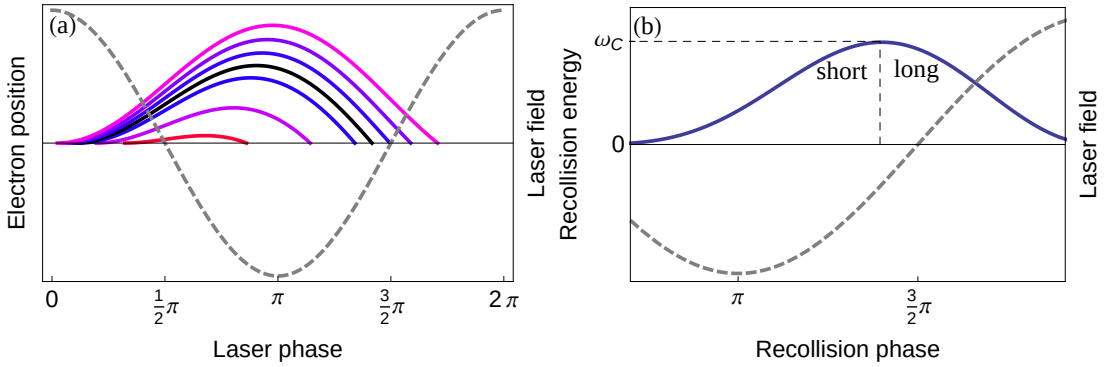

Figure 2.1: (a) The gray dashed line shows the laser field, the solid colored lines different classical trajectories. The trajectories have different ionization phases in the laser field. The recollision energy is encoded in their color. The energy increases from red to blue and the trajectory with the maximum energy (cutoff) is marked in black. In (b) we see the energies of the recolliding trajecotries for different recollision times of (a).

In Fig. 2.1 (a), we show different classical trajectories together with the laser field (gray dashed line). Recollision is only possible for trajectories ionized in the quarter cycle

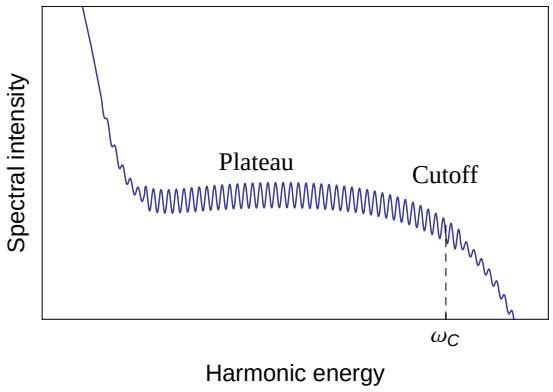

Figure 2.2: Typical HHG spectrum with plateau followed by a steep drop after the cutoff.

after each maximum or minimum of the laser cycle. Trajectories starting before do no re-encounter the origin. All trajectories recollide at different times and have a different recollision energy. The recollision energies are shown in Fig. 2.1 (b). It can be seen that each energy is emitted twice per half cycle. We call these two branches of trajectories *long* and *short* according to their excursion time in the continuum. As displayed in Fig. 2.1 (b), there is one trajectory with a maximal energy. This energy is called the cutoff energy and can be derived from the classical equations of motion yielding (in atomic units) [28]

$$\omega_c = 3.17\, U_p + I_p\,, \tag{2.1}$$

where I_p is the ionization energy and $U_p = \frac{E_0^2}{4\omega^2}$ is the ponderomotive potential equal to the average quivering energy of an electron in a sinusoidal laser field with peak strength E_0 and frequency ω.

A typical HHG spectrum is shown in Fig. 2.2. It originates from a superposition of all classically allowed trajectories leading to a spectrum with a long plateau ending at the cutoff energy ω_c. The oscillations in the plateau region are caused by the interference of two quantum paths (long and short) leading to the same energy, respectively.

Unfortunately, HHG has a poor conversion efficiency. This is mainly because the free wave packet undergoes quantum spreading during the continuum motion which is illustrated in Fig. 1.1. When the wave packet is driven back, most parts of the wave function miss the core due to the spreading. Let us briefly estimate the spreading. Just after ionization the wave packet has the dimensions of the atom on the order of 1 a.u.. The transversal spreading velocity can be estimated by $v_\perp = \sqrt{E}/I_p^{1/4}$ [111]. For a typical HHG experiment ($E \sim 0.1$ a.u., $I_p \sim 1$ a.u. and $\omega = 0.057$ a.u.), we find a wave packet dimension of $x = v_\perp \frac{2\pi}{\omega} = 35$ a.u. at recollision. Thus, spreading in the two perpendicular dimensions to the laser field reduces the HHG yield by a factor of $35^2 \sim 10^3$.

The emitted HHG light is coherent, i.e., its phase is locked to the laser phase. It arises because the wave packets keep their phase relation during ionization and during the subsequent evolution of the continuum part and bound part of the wave function. In the final step, coherent light emission is caused by the interference of the bound fraction of the wave function with the recolliding fraction in the binding potential. It leads to an oscillation in the expectation value of the electron position similar to a light-emitting,

oscillating classical dipole [102]. The phase of the dipole oscillation is determined by the wave packet phases. If the laser field is very strong, the whole wave function is ionized before recollision, no high-frequency oscillations of the expectation value of the electron position occur and no coherent HHG is emitted. The intensity regime is called saturation or over-the-barrier ionization (OBI) regime and is reached when the barrier-suppression field strength [112]

$$E_{BSI} = \frac{I_p^2}{4Z} \tag{2.2}$$

is exceeded, where Z is the residual charge seen by the ionized electron. During the recombination step incoherent light is also emitted. So far it has been assumed to be the only source of emission in the OBI regime [102]. Incoherent emission can also occur if the phase of the electronic wave packet has been randomized during the process, e.g., via collision with another atom.

2.1.1 Relativistic regime of HHG

The discussion has concentrated so far on non-relativistic laser intensities meaning that the electron is accelerated to velocities much smaller than the speed of light. Nowadays, lasers are available with much higher intensities but they cannot be used for HHG. When increasing the laser intensity, additional effects start to play a role. First, the magnetic component of the laser field becomes important. In the non-relativistic regime we neglected the action of the magnetic field and thus the electron was driven in a one-dimensional motion along the laser polarization [see Fig. 2.3 (a)]. When v/c becomes close to one, the Lorentz force caused by the magnetic field starts to influence the wave packet's motion. The wave packet is pushed [see Fig. 2.3 (b)] in the propagation direction of the laser and prevents recollision and HHG. This effect is called *relativistic drift* and becomes significant if the drift distance exceeds the wave packet dimension. This happens at laser intensities of about $10^{17}\,\mathrm{W/cm^2}$ [82, 113] at 800 nm wavelength. The various proposals as to how the drift problem could be overcome [67, 68, 70–83] are outlined in Chapter 4. When the laser intensity has even larger values such that the ponderomotive energy in the laser field becomes comparable with the electron rest mass, the actual relativistic regime is entered. This is indicated by the relativistic field strength parameter [114] $\xi = E/\omega c$ of equal to or greater than one. In this regime (starting at about an intensity of $10^{18}\,\mathrm{W/cm^2}$), the relativistic mass shift becomes important. At even higher laser intensities when the parameter $\xi\omega/c^2$ is larger than one, spin effects [115, 116] could be observed. Moreover, QED effects [15, 16, 117] are predicted to occur when the laser field in the electrons rest frame becomes comparable to the critical field strength of $E_{cr} = 1.3 \times 10^{16}\,\mathrm{V/cm}$ where the quantum vacuum breaks down.

2.2 Mathematical description of the single-atom process

Even though many aspects of HHG can be understood from classical dynamics, the HHG spectrum can only be calculated within a quantum-mechanical framework. Two main approaches are common: analytic theories based on the strong-field approximation

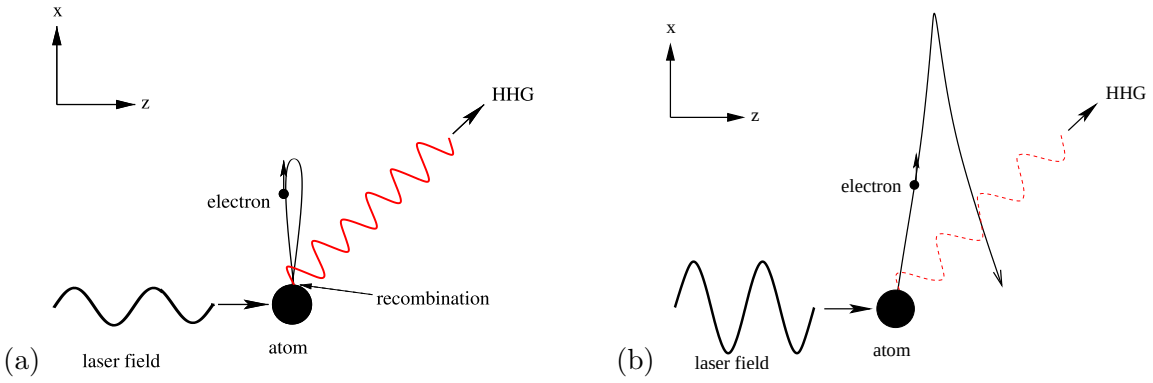

Figure 2.3: Two different classical electron trajectories for a linearly polarized wave in the (a) non-relativistic and (b) highly relativistic regime. In the relativistic case the electron does not return to the atomic core when the laser field changes its sign. HHG is unlikely what is depicted by the dashed line.

(SFA) [118–120] or a numerical solution of the time-dependent Schrödinger equation or alternatively the relativistic wave equations [121–124]. Both approaches are discussed in detail in the following.

2.2.1 Analytical framework

2.2.1.1 Strong-field approximation

The SFA is in the center of the most analytical theories in strong-field physics tackling phenomena such as above-threshold ionization, HHG and non-sequential double-ionization. The advantage of the SFA is an easy access to an intuitive interpretation of the physical problem approached. In many cases, the theory is proven to be in a good agreement with numerical studies [125, 126] and computationally less demanding.

The SFA is a possibility, to find an analytical approximate solution for the wave function of an atom or an ion in a strong laser field. To introduce its principles, we concentrate on the non-relativistic theory. The time-dependent Schrödinger equation

$$i\frac{\mathrm{d}}{\mathrm{d}t}\Psi(\mathbf{x},t) = H\Psi(t) \tag{2.3}$$

with the Hamiltonian

$$H = H_0 + H_I(t). \tag{2.4}$$

is used. $H_0 = \frac{1}{2}\hat{\mathbf{p}}^2 + V(\mathbf{x})$ is the Hamiltonian of an electron bound in the potential $V(\mathbf{x})$ and H_I covers the interaction with the laser field. We adopt the single-active electron approximation [127–129] by assuming that $V(\mathbf{x})$ is an effective potential of the most loosely bound electron. The effective potential is formed by the interaction with the core and the other more tightly bound electrons. It is often a good approximation to neglect the contribution of the tightly bound inner electrons that are ionized with a lower propability. Multi-electron effects are discussed in, e.g., [84, 92, 93, 109] and in Chapter 5.

In general, the time-dependent Schrödinger equation (2.3) has no analytical solution. Standard perturbation theory as usually employed in problems with low laser intensities cannot be applied because the interaction with the laser field cannot be considered to be a small perturbation. Therefore, we call this regime non-perturbative regime because neither the binding potential nor the laser potential are small perturbations for the evolution of the wave function. Instead, the fundamental SFA assumptions are that the binding potential is dominant before ionization and the laser field after ionization. The time-evolution operators of the separate scenarios are defined by

$$i\frac{\mathrm{d}}{\mathrm{d}t}U_0(\mathbf{x},t) = H_0U_0(\mathbf{x},t) \tag{2.5}$$

$$i\frac{\mathrm{d}}{\mathrm{d}t}U_V(\mathbf{x},t) = \left(\tfrac{1}{2}\hat{\mathbf{p}}^2 + H_I\right)U_V(\mathbf{x},t). \tag{2.6}$$

The SFA exploits that the two isolated equations can often be solved analytically.

- We use two analytical binding potentials in this thesis: the Coulomb potential and the zero-range potential [81, 130, 131]. The analytic expressions of the potentials and their ground-state solutions of (2.5) are

$$\text{Coulomb potential} \qquad V(r) = -\kappa/r \qquad \phi_0(\mathbf{x},t) = \tfrac{\kappa^{3/2}}{\sqrt{\pi}}\mathrm{e}^{-\kappa r + iI_p t}$$

$$\text{Zero-range potential} \quad V(r) = \tfrac{2\pi}{\kappa}\delta(\mathbf{x})\tfrac{\partial}{\partial r}r \quad \phi_0(\mathbf{x},t) = \sqrt{\tfrac{\kappa}{2\pi}}\mathrm{e}^{-\kappa r + iI_p t}/r$$

  where $\kappa = \sqrt{2I_p}$ with the binding potential I_p. Note that the zero-range potential has only a single bound state. The zero-range potential is employed in cases where the specific form of the potential is not important. It leads to expressions that are more easy to calculate than when the Coulomb potential is used.

- The case of an electron in the laser field only is discussed. It is described by the equations (2.6). An analytical solution exists only if the interaction with the laser field is described within the dipole approximation (DA), i.e., the electromagnetic laser field is approximated by a space-independent electric field $\mathbf{E}(t)$ only and the magnetic field component is neglected. Then, the interaction term reads $\hat{H}_I(\mathbf{x},t) = \mathbf{x}\cdot\mathbf{E}(t)$ in length gauge [125]. The DA is justified for the long-wavelength regime and non-relativistic laser intensities [68, 69, 82, 113, 117], where $kz \ll 1$ with the wave number k of the laser and the wave function dimension z along propagation direction. The analytical solution of Eq. (2.6) is called the Volkov solution [132,133]

$$\Psi_{V,\mathbf{p}}(\mathbf{x},t) = \frac{1}{\sqrt{2\pi}^3}\mathrm{e}^{i(\mathbf{p}+\mathbf{A}(t)/c)\mathbf{x}}\mathrm{e}^{-iS(\mathbf{p},t,t_0)} \tag{2.7}$$

  where

$$S(\mathbf{p},t,t_0) = \tfrac{1}{2}\int_{t_0}^{t}\mathrm{d}t'\big(\mathbf{p}+\mathbf{A}(t')/c\big)^2/2 \tag{2.8}$$

  is the classical action and $\mathbf{A}$ is the vector potential of the laser field. The electric field of the laser can be derived by $\mathbf{E}(t) = -\partial_t\mathbf{A}(t)/c$ from the vector potential.

We come back to the Schrödinger equation with the full Hamiltonian (2.4). To find an approximate solution, the equation is transformed to the Dyson equation of its time-evolution operator

$$U(t,t_0) = U_0(t,t_0) - i\int_{t_0}^{t} \mathrm{d}\tau U(t,\tau)H_I(\tau)U_0(\tau,t_0), \tag{2.9}$$

where

$$U_V(t,t_0) = \int \mathrm{d}^3\mathbf{p}|\Psi_{V,\mathbf{p}}(t)\rangle\langle\Psi_{V,\mathbf{p}}(t_0)| \tag{2.10}$$

$$U_0(t,t_0) = \mathrm{e}^{iI_p(t-t_0)}|\phi_0\rangle\langle\phi_0|. \tag{2.11}$$

Eq. (2.9) is still exact. The key point of the SFA is to replace U in the integral by U_V which means that after ionization from the unperturbed bound state by H_i, the electron evolves in a free laser field governed by U_V:

$$U_{SFA}(t,t_0) = U_0(t,t_0) - i\int_{t_0}^{t} \mathrm{d}\tau U_V(t,\tau)H_I(\tau)U_0(\tau,t_0), \tag{2.12}$$

This way the electronic wave function can be written as

$$|\Psi(t)\rangle = U_{SFA}|\phi_0\rangle \tag{2.13}$$

$$= |\phi_0\rangle\mathrm{e}^{iI_pt} - \mathrm{i}\int \mathrm{d}^3\mathbf{p}\int_{-\infty}^{t} \mathrm{d}t'|\mathbf{p}+\mathbf{A}(t)/c\rangle \times\langle\mathbf{p}+\mathbf{A}(t')/c|\mathbf{x}\cdot\mathbf{E}(t')|\phi_0\rangle\mathrm{e}^{-i(S(\mathbf{p},t,t')-I_pt')} \tag{2.14}$$

being a sum of the bound and ionized part.

2.2.1.2 Relativistic strong-field approximation

The strong-field approximation can be applied to the Klein-Gordon and Dirac equations in the same way [134–136]. As the Dirac equation is not used in this thesis, we concentrate on the solution of the Klein-Gordon equation (the presented formulas in this section are similar to [136])

$$\left(\partial^\mu\partial_\mu + c^2\right)\Psi(x) = (V_L + V_{AI})\Psi(x) \tag{2.15}$$

with the electron-ion interaction operator

$$V_{AI} = 2iV/c^2\partial_t + V^2/c^2\,, \tag{2.16}$$

and the electron-field interaction operator

$$V_L = 2i\mathbf{A}(\eta)\cdot\boldsymbol{\nabla}/c - \mathbf{A}(\eta)^2/c^2\,, \tag{2.17}$$

where V is the binding potential and $\eta = \omega t - \mathbf{k}\cdot\mathbf{x}$. To find the analytical solution, the problem is divided into two parts as before: consider only the electron-ion interaction

or only the electron-field interaction. The latter has an important difference to what was discussed in the non-relativistic part. For the case of the Schrödinger equation of an electron in the laser field only, we had to adopt the dipole approximation to have an analytical solution of the equation. Here, in the case of the Klein-Gordon equation, an analytical Volkov solution can only be found for the case of a plane wave laser field, i.e., the field depends on the phase η only. Under such conditions the Volkov solution for the Klein-Gordon equation is [134, 135] (four-vector notation is used)

$$\Psi_{\mathbf{p}}^{V}(x) = \frac{\sqrt{c}}{\sqrt{2(2\pi)^3\varepsilon_{\mathbf{p}}}} \exp\Big[- i\, p\cdot x + i\int_{\eta}^{\infty} \mathrm{d}\tilde{\eta}\, \frac{(\mathbf{p}+\mathbf{A}(\tilde{\eta})/2c)\cdot\mathbf{A}(\tilde{\eta})/c}{k\cdot p}\Big], \tag{2.18}$$

while the solution of the Klein-Gordon equation with only the binding potential is

$$\Phi(x) = \frac{\phi_0(\mathbf{x})\sqrt{c}}{\sqrt{2(c^2-I_p)}} \exp\left\{-i((c^2-I_p)t + \mathbf{x}\cdot\mathbf{A}/c)\right\} \tag{2.19}$$

where ϕ_0 is the nonrelativistic ground state wave function. The solution of the full Klein-Gordon equation (2.15) [81, 137] is

$$\Psi(x) = \Phi(x) + \int \mathrm{d}^4x'\, G^V(x,x')V_L(x')\Phi(x') \tag{2.20}$$

with the Volkov propagator

$$\begin{aligned} G^V(x,x') \;=\; & -i\,\theta(t-t')\int \frac{c\ \mathrm{d}^3\mathbf{q}}{2\varepsilon_{\mathbf{q}}(2\pi)^3} \exp\Big[- i\, q\cdot(x-x') \\ & -i\int_{\eta'}^{\eta} \mathrm{d}\tilde{\eta}\left(\frac{(\mathbf{q}+\mathbf{A}(\tilde{\eta})/2c)\cdot\mathbf{A}(\tilde{\eta})/c}{k\cdot q}\right)\Big], \end{aligned} \tag{2.21}$$

and the energy-momentum $q = (\varepsilon_{\mathbf{q}}/c, \mathbf{q})$, and $\varepsilon_{\mathbf{q}} = \sqrt{c^2\mathbf{q}^2 + c^4}$.

2.2.1.3 Harmonic spectra

Knowledge of the electronic wave function [see Eq. (2.14)] of the strong-field problem makes it possible to tackle many problems. Most crucially, in the context of this thesis, high-harmonic spectra can be calculated via the electric dipole moment

$$\mathbf{d}(t) = -\langle\Psi(t)|\mathbf{x}|\Psi(t)\rangle \tag{2.22}$$

which was pioneered by *Lewenstein et al.* [128]. Plugging the non-relativistic wave function (2.14) into Eq. (2.22) and taking only the relevant terms into account, we obtain the Lewenstein amplitude:

$$\mathbf{d}(t) = i\int_{-\infty}^{t} \mathrm{d}t' \int \mathrm{d}^3\mathbf{p}\langle\phi_0|x|\mathbf{p}+\mathbf{A}(t)/c\rangle\langle\mathbf{p}+\mathbf{A}(t')/c|xE(t')|\phi_0\rangle \mathrm{e}^{-i(S(\mathbf{p},t,t')-I_p(t'-t))}\,. \tag{2.23}$$

The spectrum can be obtained from a Fourier transform:

$$\begin{aligned} \tilde{\mathbf{d}}(\omega_H) \;=\; & i\int_{-\infty}^{\infty}\mathrm{d}t\int_{-\infty}^{t}\mathrm{d}t'\int \mathrm{d}^3\mathbf{p}\langle\phi_0|x|\mathbf{p}+\mathbf{A}(t)/c\rangle \\ & \times\langle\mathbf{p}+\mathbf{A}(t')/c|xE(t')|\phi_0\rangle \mathrm{e}^{-i(S(\mathbf{p},t,t')-I_p(t'-t)-\omega_H t)}\,. \end{aligned} \tag{2.24}$$

The integrand in (2.23) is highly oscillating because of the complex argument of the exponent and numerically difficult to calculate. Usually, one or several integrals are carried out by using the saddle-point approximation [138]. This means that the integral is only evaluated around the stationary points of the phase $S(\mathbf{p}, t, t') - I_p(t' - t)$. The stationary points are defined by the so-called saddle-point equations which correspond to energy conservation at ionization and recollision and to the recollision condition of a classical electron [128]:

$$\int_{t'}^{t} \mathrm{d}t''[\mathbf{p} + \mathbf{A}(t'')/c] = 0 \tag{2.25}$$

$$[\mathbf{p} + \mathbf{A}(t')/c]^2/2 = -I_p \tag{2.26}$$

$$[\mathbf{p} + \mathbf{A}(t)/c]^2/2 + I_p = \omega_H \tag{2.27}$$

The saddle points themselves represent the ionization and recollision time of the considered classical trajectory as well as the initial momentum. It turns out that it is sufficient to sum over a small number of classically allowed trajectories to calculate the spectrum given by Eq. (2.23). As the classical electron trajectories give an insight into the harmonic generation process, we frequently employ this model in this thesis.

2.2.2 Numerical framework

Another strategy to approach the single-atom problem is to solve the Schrödinger equation or relativistic equations numerically.

We briefly outline the two methods: solving the three-dimensional time-dependent Schrödinger equation with QPROP [122] and the two-dimensional Klein-Gordon equation with the real space split operator method [123].

2.2.2.1 Schrödinger equation

QPROP [122] is a 3D-Schrödinger solver for cylindrical symmetric potentials, e.g., spherical symmetric binding potentials in combination with a laser field within the dipole approximation (DA) as in our case. As ansatz for the wave function $\Psi(t)$, an expansion into spherical harmonics $\mathrm{Y}_{lm}(\theta, \varphi) = \mathrm{Y}_{lm}(\Omega)$ (the presented formulas in this section are similar to [122])

$$\Psi(\mathbf{x}, t) = \frac{1}{r} \sum_{l=0}^{\infty} \sum_{m=-l}^{l} \Phi_{lm}(r, t) \mathrm{Y}_{lm}(\Omega), \tag{2.28}$$

is employed where t is time, r the radius, l is the radial and m the magnetic quantum number. Inserting (2.28) into the time-dependent Schrödinger equation (2.3) yields

$$\begin{aligned}
\mathrm{i}\frac{\partial \Phi_{lm}(r,t)}{\partial t} &= \left(-\frac{1}{2}\frac{\partial^2}{\partial r^2} + V(r) + \frac{l(l+1)}{2r^2}\right)\Phi_{lm}(r,t) \\
&\quad + \mathrm{i}\frac{A(t)}{c}\left(-r\sum_{l'}\langle \mathrm{Y}_{lm}|\cos\theta|\mathrm{Y}_{l'm}\rangle\frac{\partial}{\partial r}\frac{\Phi_{l'm}(r,t)}{r}\right. \\
&\quad \left. + \sum_{l'}\langle \mathrm{Y}_{lm}|\sin\theta\frac{\partial}{\partial\theta}|\mathrm{Y}_{l'm}\rangle\frac{\Phi_{l'm}(r,t)}{r}\right) \\
&\quad + rE(t)\sum_{l'}\langle \mathrm{Y}_{lm}|\cos\theta|\mathrm{Y}_{l'm}\rangle\Phi_{l'm}(r,t). \qquad (2.29)
\end{aligned}$$

In (2.29) the radial orbitals $\Phi_{lm}(r,t)$ for different magnetic quantum numbers m are decoupled for a linearly polarized laser field within the DA. Because of this, each m component of the wave function can be propagated separately. In many cases, only the $m = 0$ state is intially populated and the other components can be ignored which saves computation time. For discretization on finite numerical grid, the general expansion (2.28) can be reduced to a sum over the first L angular momenta

$$\Psi_m(\mathbf{x},t) = \frac{1}{r}\sum_{l=0}^{\infty}\Phi_{ilm}(rt)\mathrm{Y}_{lm}(\Omega) \approx \frac{1}{r}\sum_{l=0}^{L-1}\Phi_{ilm}(rt)\mathrm{Y}_{lm}(\Omega). \qquad (2.30)$$

L is related to the number of absorbed photons and must be chosen sufficiently large. Moreover, the radial coordinate is discretized leading to 2D grid (in r and l) for each m. The discretized wave function is propagated within a Crank-Nicholson scheme [139].

2.2.2.2 Klein-Gordon equation

For relativistic laser intensities, it is necessary to employ the Klein-Gordon equation (the presented formulas in this section are similar to [123])

$$\left[\left(\mathrm{i}\frac{\partial}{\partial t} + V(\mathbf{x},t)\right)^2 - c^2\left(-\mathrm{i}\nabla + \mathbf{A}(\mathbf{x},t)/c\right)^2 - c^4\right]\varphi(\mathbf{x},t) = 0 \qquad (2.31)$$

to account for the enormously high momenta that are reached. To apply the concept of a time-evolution operator, the second-order differential equation in time, (2.31) needs to be transformed to a Schrödinger-like equation. This is possible by introducing the two-component wave function

$$\Psi(\mathbf{x},t) = \begin{pmatrix}\Psi_1(\mathbf{x},t)\\ \Psi_2(\mathbf{x},t)\end{pmatrix} = \begin{pmatrix}\frac{1}{2}\left(\varphi(\mathbf{x},t) + \frac{1}{c^2}\left(\mathrm{i}\frac{\partial}{\partial t} + V(\mathbf{x},t)\right)\varphi(\mathbf{x},t)\right)\\ \frac{1}{2}\left(\varphi(\mathbf{x},t) - \frac{1}{c^2}\left(\mathrm{i}\frac{\partial}{\partial t} + V(\mathbf{x},t)\right)\varphi(\mathbf{x},t)\right)\end{pmatrix} \qquad (2.32)$$

yielding to the new Schrödinger-like equation of motion

$$\mathrm{i}\frac{\partial\Psi(\mathbf{x},t)}{\partial t} = \hat{H}(t)\Psi(\mathbf{x},t) = \left(\frac{\tau_3 + \mathrm{i}\tau_2}{2}\left(-\mathrm{i}\nabla - q\mathbf{A}(\mathbf{x},t)/c\right)^2 - V(\mathbf{x},t) + \tau_3 c^2\right)\Psi(\mathbf{x},t) \tag{2.33}$$

in the so-called, Feshbach picture. [140]. The well-known Pauli matrices are τ_1,τ_2 and τ_3. Under these precautions the wave function can be propagated via a splitting of the time evolution operator

$$\Psi(\mathbf{x},t+\Delta t) = \hat{U}_{\hat{V}}\left(t+\Delta t,t,\tfrac{1}{2}\right)\hat{U}_{\hat{K}}\left(t+\Delta t,t,1\right)\hat{U}_{\hat{V}}\left(t+\Delta t,t,\tfrac{1}{2}\right)\Psi(\mathbf{x},t) + O\left(\Delta t^3\right), \tag{2.34}$$

where the operator covering the potential energy part is given by

$$\hat{U}_{\hat{V}}\left(t+\Delta t,t,\delta\right)\Psi(\mathbf{x},t) = \exp\left(\delta\mathrm{i}\int_t^{t+\Delta t} V(\mathbf{x},t') + \tau_3 c^2\,\mathrm{d}t'\right)\Psi(\mathbf{x},t)$$

and the kinetic energy part by

$$\hat{U}_{\hat{K}}\left(t+\Delta t,t,\delta\right)\Psi(\mathbf{x},t) = \Psi(\mathbf{x},t) - (\tau_3+\mathrm{i}\tau_2)\delta\frac{\mathrm{i}}{2}\int_t^{t+\Delta t}\left(-\mathrm{i}\nabla + \mathbf{A}(\mathbf{x},t')/c\right)^2\mathrm{d}t'\,\Psi(\mathbf{x},t)\,. \tag{2.35}$$

Because of the special Pauli algebra, Eq. (2.35) incorporates only a first-order and second-order derivative in space and the whole expression can be evaluated in real space. This is in contrast to the Schrödinger equation where the split-operator method is also frequently applied and terms with e^{∇} contain derivatives of infinite order. In that case, time-consuming Fourier transforms between real and momentum space are necessary to cope with these terms. Here, the scheme allows for an efficient parallelization on a computer cluster because the grid can be divided into areas with little communication between them.

2.3 Macroscopic perspective on HHG and phase–matching

The previous part concerned the HHG process of a single atom. In experiments, gas targets with a large number of atoms are used with pressures up to an atmospheric level. An illustration of a typical HHG setup is shown in Fig. 2.4. The red area is the laser pulse, which propagates through the gas [141, 142] or plasma [141] to the right direction independently of the HHG process. In dense media or in case of high intensities, serious deformation of the laser pulses can occur. The laser triggers the HHG process of each atom. As illustrated in Fig. 2.4, constructive interference of the emitted light occurs when the laser and the emitted light propagate uniformly and dispersion-free at the same speed. Then harmonic light that has just been created by the laser matches up in phase with the light that has been previously generated and the macroscopic HHG signal scales quadratically with the number of atoms.

Normally, all atoms can be assumed to be independent emitters because the interaction between electrons of different atoms is negligible [143]. Correlation only becomes

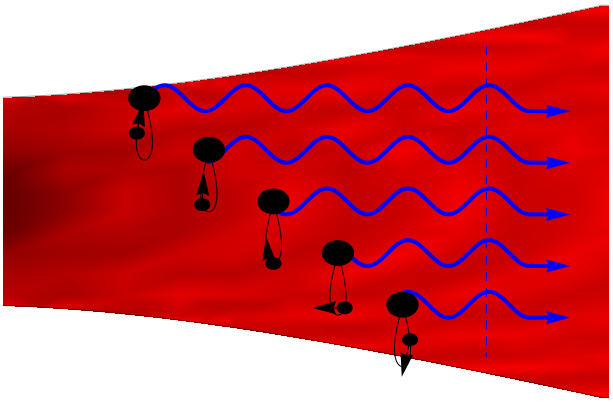

Figure 2.4: The case of coherent addition of the emitted light (blue) from different atoms (black) is shown. The HHG process of each atom in the Gaussian focus (red) cell is coherently triggered by the laser which propagates to the right

important in highly pressurized gases with densities larger than $10^{19}/\,\mathrm{cm}^3$ which are not considered in this thesis.

The condition of constructive interference — the so-called phase-matching — is not automatically fullfilled among other things because the IR laser light that triggers HHG does not travel at the same speed as the xuv/x-ray HHG light. For this reason, the phase front of the previously generated light does not match with newly generated light at another position. More quantitatively, the harmonic electric field emitted from different atoms differs by a phase factor of $\mathrm{e}^{i\Delta\mathbf{k}\cdot\mathbf{x}_a}$ with the atomic position $\mathbf{x}_a$ and the phase-mismatch vector [142]

$$\Delta\mathbf{k} = \mathbf{k}_H - \frac{\omega_H}{\omega_L}\mathbf{k}_L - \mathbf{k}_{geo} - \mathbf{k}_{dip}\,, \tag{2.36}$$

where $\mathbf{k}_L$ is the wave vector of the laser which triggers the HHG process, $\mathbf{k}_H$ the wave vector of the harmonic field with a free choice of its direction, $\mathbf{k}_{geo}$ a geometrical term and $\mathbf{k}_{dip}$ is the change of the emission phase of the atoms depending on the position. All terms will be discussed in more detail shortly. The overall emission of the macroscopic gas target is proportional to a three-dimensional spatial integral $\int_V \mathrm{d}^3\mathbf{x}_a \mathrm{e}^{i\Delta\mathbf{k}\cdot\mathbf{x}_a}$ that results only in a considerable yield if Δk is small. Destructive interference between different atoms occurs when the medium length of

$$L_{coh} = \frac{\pi}{|\Delta\mathbf{k}|} \tag{2.37}$$

is exceeded which is called the coherence length. In principle, on a single-atom level harmonics are emitted in all directions $\mathbf{k}_H$. However, phase-matching selects certain emission directions where $\Delta\mathbf{k}$ is smallest. As the last three terms in (2.36) are mainly directed into the laser propagation direction, Δk is smallest for $\mathbf{k}_H$ along the same direction. Thus, the medium emits mainly along the laser propagation direction.

Different issues contribute to the phase-mismatch vector (2.36). The dispersion is caused on the one hand by the refractive index of the atoms or ions n_{at} and the free

electron background

$$n_{el}(\omega) = \sqrt{1 - \frac{\omega_p^2}{\omega^2}}\,, \tag{2.38}$$

with the plasma frequency $\omega_p = \sqrt{4\pi\rho_e}$, the electron density ρ_e and laser frequency ω. It results in a different group velocity of the laser and HHG light and causes pulse deformation. On the other hand, the phase velocity of the light is modified by geometric effects such as focusing (e.g., Guoy phase) or by the propagation in a filament. For instance, in the case of a Gaussian focus on axis

$$k_{geo} = -\frac{\omega_H}{\omega_L}\frac{2}{b(1+(2z/b)^2)}\,, \tag{2.39}$$

with the confocal parameter b. All previous contributions considered the light propagation and the times HHG is triggered. Apart from this, each atom emits with a certain phase that is determined by the quantum nature of the process. It is equal to the phase of the atomic dipole moment given by Eq. (2.23). The phase depends on the local laser intensity and is given by $\phi_{dip} = -S(\mathbf{p}, t, t') + I_p(t'-t) = -(\beta U_p + I_p)\tau$ with the numerical factor β, the excursion time τ of the quantum trajectory leading to the harmonic energy under consideration. Thus, the phase depends approximately linearly on the intensity [31]: $\phi_{dip} = -\alpha I$ (proportionality parameter α). For this reason, the emission phase varies in a Gaussian focus. In summary, the phase-mismatch can be written as

$$\Delta k = \frac{\omega_H}{c}\Delta n_{at}(\mathbf{x}) + \frac{\omega_H}{c}\Delta n_{el}(\mathbf{x}) - k_{geo} + \alpha\partial_z I\,, \tag{2.40}$$

where $\Delta n_i = n_i(\omega_H) - n_i(\omega_L)$. In experiments, it is necessary to find a condition where all contributions in (2.40) cancel each other out.

For many HHG experiments where the energies are below 100 eV, the laser intensity, ionization rate and the gas pressure (a few tens of mbar) are low and focusing is the biggest contribution [last two terms in (2.40)]. Both contributions can balance each other off leading to a stable phase-matching condition $\Delta k \approx 0$. Tiny differences are tolerable as long as the coherence length (2.37) is longer than the medium length. In general, this is easier for lower harmonic energies because the coherence length (2.37) increases with lower harmonic energies and the plasma background is lower for small laser intensities. Under these conditions, phase-matching is usually achieved by using optimized focusing parameters and placing the atomic gas jet at the right position in the laser focus.

Phase-matching is more difficult to achieve for higher HHG energies, ionization rates, and gas pressures. Several phase-matching schemes have been proposed. Gas filled capillaries of suitable pressure can be employed [144] to adjust the group velocity of the laser pulse. For strong laser pulses close to the saturation limit, the free electron background considerably changes along the pulse leading to a dispersion that deforms the pulse in such a way that phase-matching is achieved, the so-called non-adiabatic phase-matching [145, 146]. A very promising concept is to use long wavelength driving fields [97, 147] that allow an increase in the cutoff [Eq. (2.1)] without increasing the laser field strength and keeping the ionization level low. The condition also permits an increase of the gas pressure resulting in very efficient HHG. Additionally, quasi-phase-matching

(QPM) schemes are known. QPM schemes break the spatial symmetry in $\mathrm{Re}\, e^{i\Delta\mathbf{k}\cdot\mathbf{x}_a}$ between the positive and negative contributions. This way certain emission phases are favored and complete cancellation is prevented. In this regard a weak counterpropagating IR field [148, 149], weak static fields [150] or modulated wave guides [151–153] can be employed.

3 Interference model of HHG and continuum–continuum HHG

A fundamental interference picture of HHG is developed to include continuum-continuum (CC) transitions. Even though CC transitions have been considered to be less relevant, a novel CC transition is discussed that can be the dominant HHG mechanism under certain conditions. This is verified by studying HHG numerically from a hydrogen atom exposed to an intense laser field in the saturation regime. Moreover, an analytical model of CC HHG is developed in excellent agreement with the numerical results. By means of this model, it is shown that CC harmonics show a significantly different phase-matching behavior than the traditional HHG mechanism. Finally, it is outlined that CC HHG could advance molecular tomography.

3.1 Photo-emitting transitions in HHG

3.1.1 Continuum–bound HHG

HHG is successfully described by the 3-step model [28, 29, 128] (see introduction in Section 2.1). The last step of this model – the photoemission – is explained by the recombination of an energetic electron with its parent ion. In [102] it was shown that this picture has to be extended: it is essential for *coherent* HHG emission that the recolliding electronic wave packet interferes with a portion of the same wave function still being bound to the parent ion. Only in this case coherent high-frequency light is emitted meaning that its phase is locked to the laser phase and the overall yield scales quadratically with the number of atoms. This coherent photoemission is absent if the laser has entirely ionized the wave function before recollision. For this reason, coherent HHG in the over-the-barrier (OBI) or saturation regime has been considered to be suppressed so far [102].

The interference between the recolliding continuum wave packet and the bound wave packet can even be observed in quantum simulations as an oscillation of the probability distribution of the electron. In analogy to an oscillating dipole in classical electrodynamics, radiation with the frequency of these oscillations is emitted. This kind of emission is named continuum–bound (CB) HHG because the two involved states are a recolliding continuum state and the bound state. Exactly this picture of interference enables the tomographic measurement of molecular orbitals [33] from their HHG spectrum. However, in this picture the role of the binding potential is not completely recognized. Neither has it been extended to continuum-continuum transitions which constitute the main subject of this chapter.

Note that apart from coherent radiation considered in this thesis, a recolliding electronic wave packet can also cause emission of incoherent radiation. This spontaneous process

also occurs when the electronic wave function is fully depleted. However, in a macroscopic gas target its emission yield scales only linearly with the number of atoms instead of the quadratic scaling typical for the coherent CB transition in the phase-matched case.

3.1.2 Continuum–continuum HHG

Besides the described CB transition, there are additional scenarios in an electron-ion collision in a laser field where coherent light is emitted. The other class of transitions is termed continuum–continuum (CC) HHG because it involves continuum states only.

First a brief review is given about the two classes of CC transitions that are described in the literature [see Fig. 3.1 (a) and (b)]:

- The first case is most apparent for laser intensities in the saturation regime where the whole electronic wave function is completely ionized within one laser half cycle. The recolliding electronic wave packet scatters at the ionic core which results in the emission of bremsstrahlung [154]. The process is schematically displayed in Fig. 3.1 (a). Calculations [103] show the possibility of the emission of very short radiation bursts down to the attosecond regime, but the photon energies are very low compared to CB HHG.

- The other known CC scenario [shown in Fig. 3.1 (b)] occurs when the recolliding wave packet interacts with a just-ionizing part of the bound wave function [107, 108, 155] within the range of the Coulomb tail of the ionic potential. Because the scenario is connected with the ionization process, it only occurs in the multiphoton or tunneling regime where a large fraction of the wave function is still bound at the recollision time. As long as recollision happens when the laser field is nonvanishing, CB HHG is always accompanied by this CC transition. On the other hand, when the laser field vanishes no just-ionizing wave packets exist and the transition does not take place. The transitions is also absent together with CB emission when the whole wave function has been freed in the saturation regime. The transition is very similar to CB HHG only the second involved state slightly differs. Thus, the emission spectrum has these similarities imprinted: the CC spectrum exhibits the same plateau-like structure as the CB spectrum. However, the CC spectrum is several orders of magnitude suppressed to CB HHG [106] and can be neglected in many situations [105].

Apart from the transitions described above, the impact of the various wave packets in the continuum has not been fully recognized yet. In this chapter it is shown that two simultaneously recolliding wave packets [see Fig. 3.1 (c)] lead to a significant harmonic response. The simultaneous recollision can occur in multi-cycle laser pulses. It will be shown that this new CC scenario becomes dominant when the laser intensity approaches the OBI regime. This CC transition is the main topic of this chapter.

3.1.3 Basic model of emission

A simple model being capable of unifying the different types of transitions outlined above is presented. In an electron–atom collision, the coherent part of the emitted radiation [156,

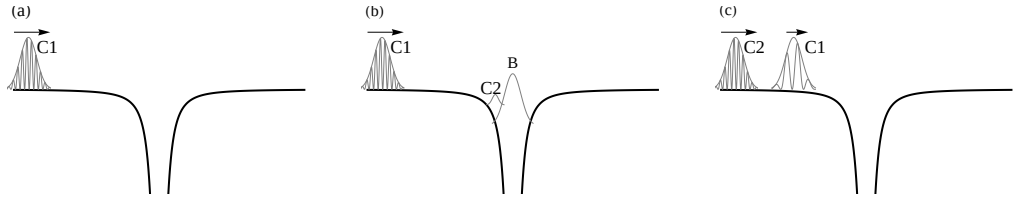

Figure 3.1: Schematic of the different CC transitions occurring in HHG. We concentrate on the coherent response. The thick black line is the potential, the thin gray lines are the different wave-packet portions. In (a) Bremsstrahlung is emitted when the wave packet (C1) interacts with the core. In (b) the recolliding wave packet will interfere with the bound wave packet (B) and a just-emerging continuum wave packet (C2) leading to CB and CC harmonics, respectively. In (c) the mechanism of our work is presented. Two continuum wave packets (C2 and C1) of *different momentum* recollide at the same time and interfere with each other emitting photons of exactly their kinetic-energy difference.

157] can be calculated via the expectation value of the acceleration using the Ehrenfest theorem

$$\mathbf{a}(t) = -\langle\Psi(t)|\nabla V|\Psi(t)\rangle \tag{3.1}$$

with the ionic potential V. Note that this approach, in consistence with earlier and current atomic HHG theory, considers only the coherent part of the emission response and neglects incoherent spontaneous emission which cannot be phase-matched.

In the following, the general conditions required for emission of radiation are investigated by considering (3.1) for $|\Psi(t)\rangle$ being a superposition of different (asymptotic) eigenstates $|\epsilon_i\rangle$. The following model holds strictly true only for time-independent Hamiltonians but its picture remains true in atomic HHG with collision times typically short on the time scale of a laser period.

If $|\Psi(t)\rangle$ is an eigenstate of the Hamiltonian, the expectation value (3.1) is time-independent. Accordingly, harmonic emission can only occur for a linear combination of at least two eigenstates: $|\Psi_1(t)\rangle = a_1|\epsilon_1\rangle \mathrm{e}^{-i\epsilon_1 t} + a_2|\epsilon_2\rangle \mathrm{e}^{-i\epsilon_2 t}$. Inserting $|\Psi_1(t)\rangle$ into (3.1) and separating the time-dependent part $a(t) = -a_1^* a_2 \langle\epsilon_1|\nabla V|\epsilon_2\rangle \mathrm{e}^{-i(\epsilon_2-\epsilon_1)t}$ + c.c. shows that the resulting dipole oscillates with the difference energy between the two states. The efficiency of the transition depends on the matrix element $\langle\epsilon_1|\nabla V|\epsilon_2\rangle$ describing the overlap between the two states and the core potential. This way, the potential mediates the momentum transfer between the two states.

All discussed HHG transitions can be understood in this context. Coherent emission can occur if two states interfere at a place where a potential gradient exists.

- In the case of CB HHG, a recolliding electronic plane wave (energy ϵ_1) interferes with the bound wave packet (energy $-I_p$) and the difference energy ($\epsilon_1 + I_p$) is emitted.

- In this picture, the coherent bremsstrahlung of Fig. 3.1 (a) is an interference of the different momentum eigenstates contained in the wave packet. Accordingly, the range of emission energies depends strongly on the spectral width of the wave packet.

- The CC transition of Fig. 3.1 (b) is an interference between a recolliding wave packet and a just-ionized wave packet (approximately zero energy). Thus, the emission energy is mainly given by the recollision energy and similar to the CB energy only differing by the ionization potential.

- In a new scenario of CC HHG [illustrated in Fig. 3.1 (c)], if a bichromatic electron wave sweeps over a potential, it would lead to light emission at the kinetic energy difference. This chapter is devoted to the description of this transition and it is shown that it can be the dominant HHG mechanism under certain conditions. In principle, the transition is the general case of the transition described in Fig. 3.1 (b) which is restricted to a very short excursion time of the second wave packet. Our results will show that the emitted radiation is distinguishable from the CB spectrum due solely to the arbitrary excursion times of C1 and C2 in Fig. 3.1 (c).

The previous idea provides a fundamental interference picture of HHG: wave function splitting or spreading, subsequent simultaneous recollision with different energies, and core-mediated transitions with photoemission at the difference energy.

To numerically illustrate this model and the difference frequency mechanism, the one-dimensional time-dependent Schrödinger equation is solved carried out by Robert Heck in his bachelor thesis [158]. A 1-dimensional hydrogen atom is chosen using a smoothed Coulomb potential $V(x) = 1/\sqrt{x^2 + a^2}$ with the smoothing parameter $a = 1.4039$ to match the hydrogen ionization potential.

Four cases are considered: (a) a monochromatic free-electron wave packet colliding with a partially ionized atom (the conventional CB HHG scenario), (b) the same as (a) but for a fully ionized atom, (c) a bichromatic free electron wave packet colliding with a fully ionized atom, and (d) a bichromatic free-electron wave packet colliding with a partially ionized atom. The dipole acceleration expectation value is analyzed by means of a windowed Fourier transform (Gabor transform) [159, 160]:

$$\tilde{a}(\omega_H, t) = \int_{-\infty}^{\infty} \mathrm{d}t' a(t') \mathrm{e}^{-i\omega_H t} \mathrm{e}^{-(\frac{t-t'}{\Delta_t})^2} \tag{3.2}$$

with a temporal window size of $\Delta_t = 3\,\mathrm{a.u.}$. $|\tilde{a}(\omega_H, t)|^2$ is plotted on a logarithmic scale in Fig. 3.2.

In case (a), a dipole response at a frequency corresponding to the sum of the electron kinetic energy and the ionization potential of the atom $E_{\mathrm{kin}} + I_{\mathrm{p}}$ is observed, well-known from traditional CB HHG. In case (b), no high-energy dipole acceleration response can be observed. The low energy signal corresponds to the bremsstrahlung CC spectrum [103] arising due to the non-vanishing spectral width of the recolliding wave packet. Case (c) exhibits a dipole response at a lower frequency than the one obtained in (a), while case (d) shows a total of 3 different frequencies.

The absence of any high-energy emission in case (b) arises from the lack of interference as only one electronic state takes place in the interaction in consistence with an earlier theoretical study [102]. Emission in (c) is created by the interference of two free-electron wave packets with kinetic energies of $E_{\mathrm{kin},1}$ and $E_{\mathrm{kin},2}$ that create a time-dependent dipole moment corresponding to a beating frequency of the difference $E_{\mathrm{kin},1} - E_{\mathrm{kin},2}$ inside the

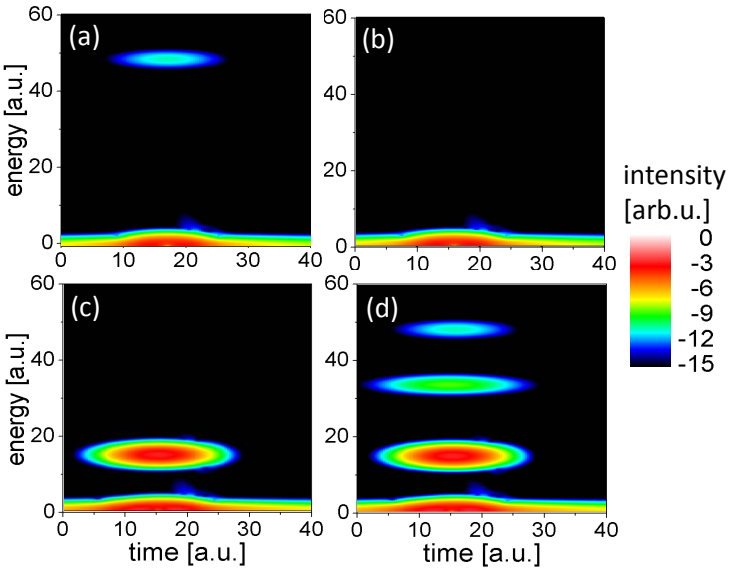

Figure 3.2: (color online) Electron–atom collision and analysis of the dipole acceleration response. Windowed Fourier transforms [Eq. (3.2)] on a logarithmic scale are shown for four cases: (a) monochromatic electron wave packet (47.8 a.u. kinetic energy) colliding with a partially ionized atom, (b) same as (a) but for a fully ionized atom, (c) a bichromatic electron wave packet (47.8 a.u., 33.1 a.u. kinetic energies) colliding with a fully ionized atom, (d) same as (c) but for a partially ionized atom. In (c) and (d) the signature of CC electron interference is observed at the difference kinetic energy of 14.7 a.u..

non-linear Coulomb field of the atom. This is the origin of the coherent CC HHG emission process discussed in the following Sec. 3.2-3.5 and illustrated in Fig. 3.1 (c). Case (d) shows emission due to both free-electron wave packets, each interfering with the bound state and amongst themselves, giving rise to three distinct dipole oscillation frequencies. Note that CC transitions also occur when the two wave packets meet each other in the potential with opposite (different absolute) momenta but with a lower probability as a consequence of the higher momentum transfer required.

3.2 HHG in the saturation regime – numerical analysis

In the previous discussion we obtained the CC signature of Fig. 3.2 (c) by a suitable choice of the initial state: two simultaneously recolliding wave packets with different energies. In practice, this can be reached by using a multicycle laser pulse as displayed in Fig. 3.3 (a). Apart from the electric laser field (gray dashed line), two classical trajectories (red and blue lines) are shown that start in different half cycles of the pulse but recollide at the same time. This way, the same condition is reached as for the simulation carried out before [Fig. 3.2 (c)]. In the following, it is shown that the CC transition occurs in common HHG scenarios of an atom in a laser field and can play a significant role.

As a fully quantum mechanical model, we solve the 3-dimensional time-dependent Schrödinger equation for a hydrogen atom with $V(r) = -1/r$ in a strong field. Instead,

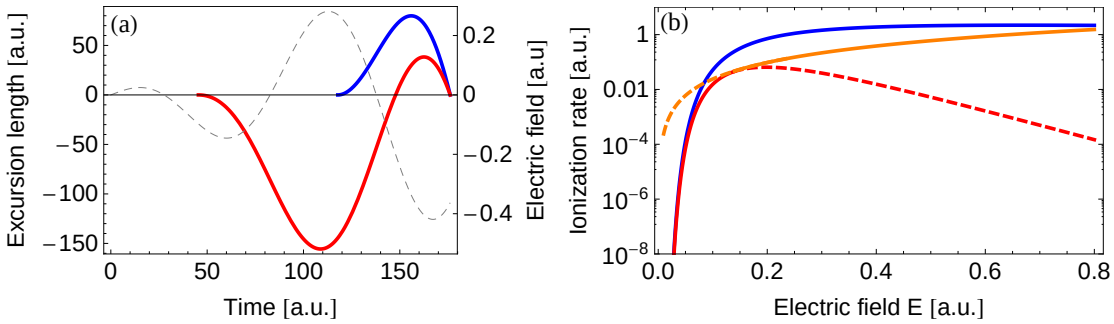

Figure 3.3: (a) Two classical trajectories (red and blue lines) starting from different half cycles driven by a laser pulse (gray, dashed line) and recolliding at the same time. (b) displays the instantaneous ionization rates of a hydrogen atom calculated via different models: ADK model (blue) [161, 162], empirical ADK extension (red) [163] and fit function (orange) [164]. The dashing denotes where the empirical formulas fail.

any other atom, ion or molecule could be selected. The peak intensity of $10^{16}\,\mathrm{W/cm^2}$ of the laser pulse [shown in Fig. 3.4 (a)] is chosen such that almost complete depletion of the ground state occurs on the leading edge of the pulse. The temporal evolution of the ground-state population

$$n_0(t) = \exp\Big(-\int_{-\infty}^{t} \mathrm{d}\tau\, w(\tau)\Big) \tag{3.3}$$

is shown in Fig. 3.4 (a), where $w(\tau)$ is the ionization rate. The frequently used analytical ADK ionization rate $w_{ADK}(t)$ defined in Refs. [161, 162] gives very accurate results for tunnel ionization of atoms for laser intensities below the saturation intensity [see Eq. (2.2)]. In the present case, the saturation intensity of $1.4 \times 10^{14}\,\mathrm{W/cm^2}$ ($\sim E_{BSI} = 0.0625\,\mathrm{a.u.}$) for a hydrogen atom is exceeded and $w_{ADK}(t)$ fails. A very accurate analytic description of the ionization rate for intensities slightly in the saturation regime is given by the empirical formula

$$w_{Lin}(t) = w_{ADK}(t) \exp\Big(-\alpha(Z/I_p)\Big(E(t)/\sqrt{2I_p}^{3}\Big)\Big) \tag{3.4}$$

of [163] with the fit parameter $\alpha = 6$. Both, the comparison with numerical data [163] and the decrease of the function for higher field strength [see red line in Fig. 3.3 (b)] show limitations of the expression for larger laser field strengths. At this point the fit function [orange line in Fig. 3.3 (b)]

$$w_{Bauer}(t) = 2.4E^2(t) \tag{3.5}$$

of [164] is employed. We combine both formulas in the following way:

$$w(t) = \begin{cases} w_{Lin}(t) & E(t) < 0.14\,\mathrm{a.u.} \\ w_{Bauer}(t) & E(t) > 0.14\,\mathrm{a.u.} \end{cases}$$

This is in agreement with the numerical analysis drawn in [163, 164]. Note that the ionization rate is only necessary for the analysis [e.g. Fig. 3.4 (a)] of the numerical results but not for the solution of the TDSE. However, in Section 3.3, where an analytical description of the CC response is developed, a precise knowledge of the ground-state population is required.

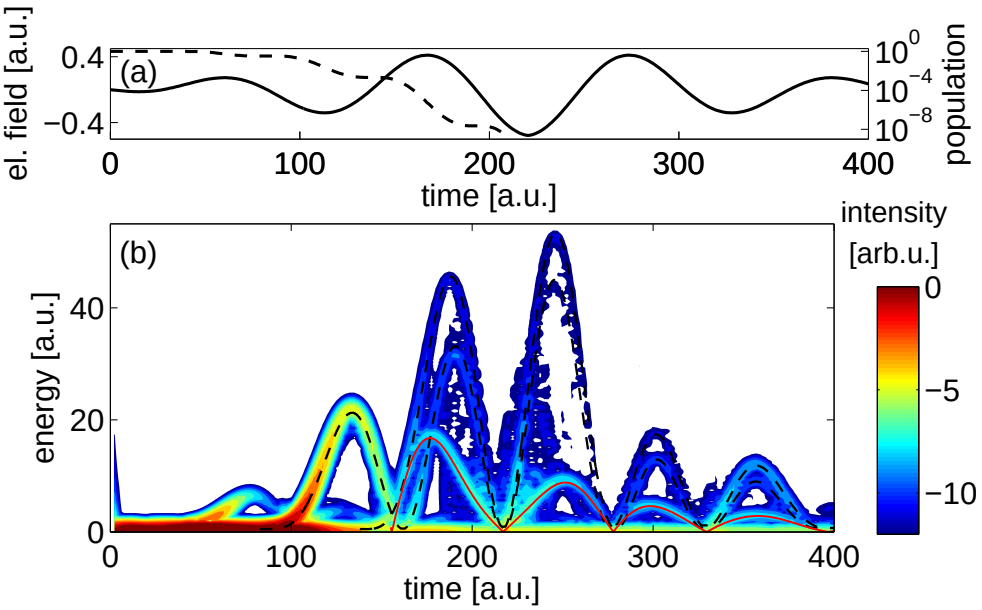

Figure 3.4: Time-frequency analysis of HHG showing the signature of CC wave packet interference. (a) Driver pulse used in the simulation and the ground-state population calculated via [163, 164]. We do not show the population below 10^{-8} because the analytic model [see Eq. (3.2)] yields no reliable results in this high-depletion case. (b) Windowed Fourier transform of the HHG emission on a logarithmic scale. Dashed black lines: classically calculated kinetic energies of electrons returning to the ion. Solid red line: difference between the two black dashed curves.

The depletion after the leading edge of the pulse will cause that CB transitions are entirely suppressed and according to current theories no high-energy HHG is expected any more. This regime offers us to observe the CC transitions isolatedly. Even though the laser intensity (peak at $10^{16}\,\mathrm{W/cm^2}$) and accordingly the recollision energies (up to 500 eV) are larger than in most of the current HHG experiments, our results are not specific to these intensities. The code QPROP [122] is used to solve the TDSE (see Sec. 2.2.2.1). The following simulation parameters are chosen: a time step of $\Delta t = 0.01$ a.u., a radial grid of $r_{max} = 800$ a.u. with a spacing of $\Delta r = 0.1$ a.u. and a highest angular momentum of $L = 140$. Again, the windowed Fourier transform of the dipole acceleration (3.2) of the 3D TDSE simulation is calculated and shown in Fig. 3.4 (b).

To analyze the individual time-resolved frequency components contained in the dipole response, Newton's equations are used to calculate classical electron trajectories in the laser field originating from the ion. In Fig. 3.4 (b), the classical CB (recombination) energy of $E_{\mathrm{kin},1,2} + I_\mathrm{p}$ (dashed black lines) as well as the energy difference $E_{\mathrm{kin},1} - E_{\mathrm{kin},2}$ of the two returning classical trajectories (solid red), each vs. the time of recollision is shown. We compare those to the dipole-response obtained from the quantum calculation: until time $t = 150$ a.u., HHG emission is caused by CB transitions that are still rather strong because the bound state has not been fully depleted [compare Fig. 3.4 (a) dashed line]. After time $t = 150$ a.u., we can clearly observe both the signature of ground-state (CB) recombination as well as CC interference by comparing to the classically calculated return energies. Interestingly, the CC component of the dipole response is the dominant

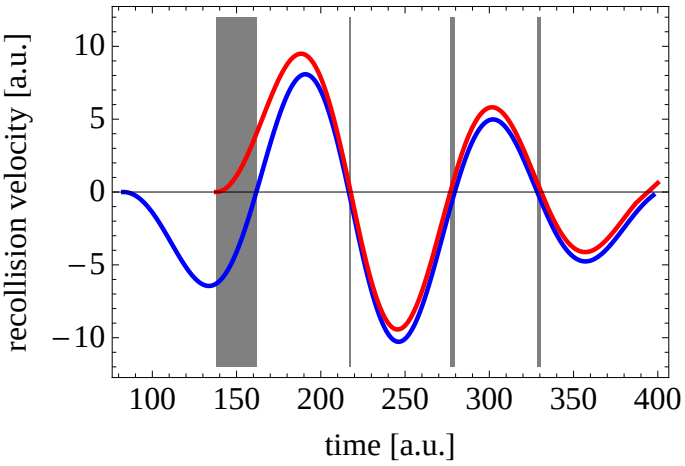

Figure 3.5: The classical recollision momenta for electrons ionized from either the two (red and blue) main ionization time windows at the beginning of the laser pulse. Only, in a small temporal region (gray shaded areas) the CC transitions are caused by trajectories having a velocity pointing in opposite directions.

contribution for several half-cycles between $t = 150$ a.u. and $t = 320$ a.u. This is because depletion of the ground state occurs around $t = 150$ a.u. and thus interference with and recombination to the ground state can no longer take place. Instead, the two parts of the wave packet, which have been ionized within the first two half cycles interfere steadily with each other in the atomic potential for the remainder of the laser pulse. From Fig. 3.5 we can see that the two wave packets mainly impinge onto the atom from the same direction. The figure shows the recollision momentum of classical electron trajectories ionized from either of two half cycles in blue and red. Therefore, the plot is similar to the dashed lines in Fig. 3.4 (b) but instead of plotting the energy, the momentum is shown. The gray areas mark the small time windows of recollision from opposite directions. Recollision from the same direction is more efficient because the nucleus has to compensate for a smaller momentum in order to conserve the overall momentum.

Note that the electronic interference described here is different from the optical interference of the harmonic field caused by the well-known *short* and *long* trajectories.

The significance of the signal is pointed out by estimating the photon yield in a small energy window between 12 a.u. and 18 a.u.. Assuming a phase-matched gas volume with radius 100 μm and length 1 mm having a density of $10^{18}/\mathrm{cm}^3$ and emitting into a solid angle of 10^{-9} Sr, we calculate a yield of 10^3 photons per shot originating from CB transitions within the time window of $t = 110$ a.u. and $t = 155$ a.u.. Between $t = 155$ a.u. and $t = 200$ a.u., a photon number of 10^{-1} is emitted within this bandwidth mainly caused by CC transitions. Laser systems with the typical kHz repetition rates could allow for a measurement of this effect. The emission yield could potentially be enhanced by using larger atoms and molecules with stronger core potentials.

In an experiment measuring the CB and CC transitions simultaneously, the impact of the CC transitions on the spectrum is larger than the mentioned ratio of four orders of magnitude between $|\tilde{a}_{CB}(\omega)|^2$ and $|\tilde{a}_{CC}(\omega)|^2$. In the spectrum, the contribution of the arising cross term between both amplitudes would be only two orders of magnitude lower

than the $|\tilde{a}_{CB}(\omega)|^2$ term:

$$|\tilde{a}_{CB}(\omega) + \tilde{a}_{CC}(\omega)|^2 \approx |\tilde{a}_{CB}(\omega)|^2 + 2\,\mathrm{Re}\,\tilde{a}_{CB}(\omega)\tilde{a}_{CC}(\omega)\,. \tag{3.6}$$

Therefore, in experiments, where a precise measurement of the spectrum is necessary, CC contributions could appreciably influence the result.

3.3 Analytical theory of continuum–continuum HHG

In this section, an analytical theory of the CC recollision process and harmonic emission is developed based on the strong-field approximation (SFA).

The standard approach to HHG within the SFA where the dipole moment $\mathbf{d}(t) = -\langle\Psi(t)|\mathbf{r}|\Psi(t)\rangle$ is calculated [128] is not sufficient since two plane continuum waves with different momenta $\mathbf{p}'' \neq \mathbf{p}'$ have a vanishing dipole moment $\langle\mathbf{p}''|\mathbf{r}|\mathbf{p}'\rangle = 0$. This vanishing dipole moment is a failure of the lowest order SFA-Volkov solution where no distortion of the plane waves by the potential of the atom is included. To account for the impact of the potential, we directly calculate the nonlinear dipole acceleration via the expectation value of the acceleration (Eq. (3.1)) $\mathbf{a}(t) = -\langle\Psi(t)|\nabla V|\Psi(t)\rangle$ as is common practice in numerical approaches. This way, the interaction of the electron with the core is included which is needed for the momentum conservation of the CC transition [165]. Within the dipole approximation (DA), the electronic wavefunction can be written as [see Eq. (2.14)]

$$\begin{aligned} |\Psi(t)\rangle &= |\phi_B(t)\rangle + |\phi_C(t)\rangle \\ &= \sqrt{n_0(t)}|0\rangle \mathrm{e}^{iI_p t} \\ &\quad -i\int \mathrm{d}^3p|\mathbf{p}+\mathbf{A}(t)\rangle \int_{-\infty}^{t} \mathrm{d}t'\sqrt{n_0(t')}\langle\mathbf{p}+\mathbf{A}(t')|\mathbf{r}\cdot\mathbf{E}(t')|0\rangle \mathrm{e}^{-i(S(\mathbf{p},t,t')-I_p t')}, \end{aligned} \tag{3.7}$$

where

$$S(\mathbf{p},t,t') = \int_{t'}^{t} \mathrm{d}\tau(\mathbf{p}+\mathbf{A}(\tau))^2/2 \tag{3.8}$$

is the classical action. In addition to the common SFA ansatz [128], the ground-state population $n_0(t)$ [see Eq. (3.3)] is empirically inserted, which is necessary in the OBI regime [166].

Inserting (3.7) into the expression for the expectation value of the acceleration (3.1) yields four contributing terms:

$$\begin{aligned} \mathbf{a}(t) = &- \langle\phi_B(t)|\nabla V|\phi_B(t)\rangle - \langle\phi_B(t)|\nabla V|\phi_C(t)\rangle \\ &- \langle\phi_C(t)|\nabla V|\phi_B(t)\rangle - \langle\phi_C(t)|\nabla V|\phi_C(t)\rangle \end{aligned} \tag{3.9}$$

The first term of this sum is zero because $\phi_B(t)$ is an eigenstate of the atomic potential and does not radiate. The third term is the complex conjugate of the second term.

The dipole acceleration of the CB transition can be identified as

$$\mathbf{a_{CB}}(t) = -\langle\phi_B(t)|\nabla V|\phi_C(t)\rangle + \text{c.c.} \tag{3.10}$$

and of the CC transition as

$$\mathbf{a_{CC}}(t) = -\langle\phi_C(t)|\nabla V|\phi_C(t)\rangle \tag{3.11}$$

and plugging the entire expression of the wave function (3.7) into (3.10) and (3.11), one obtains

$$\begin{aligned}\mathbf{a_{CB}}(t) &= i\int \mathrm{d}^3p \int_{-\infty}^{t} \mathrm{d}t' n_0(t) n_0(t') \langle 0|\nabla V|\mathbf{p}+\mathbf{A}(t)\rangle\langle \mathbf{p}+\mathbf{A}(t')|\mathbf{r}\cdot\mathbf{E}(t')|0\rangle \\ &\quad \times \mathrm{e}^{-i(S(\mathbf{p},t,t')+I_p(t-t'))} + \text{c.c.} \qquad (3.12)\\ \mathbf{a_{CC}}(t) &= -\int \mathrm{d}^3p' \int_{-\infty}^{t} \mathrm{d}t' \int \mathrm{d}^3p'' \int_{-\infty}^{t} \mathrm{d}t'' n_0(t') n_0(t'') \langle 0|\mathbf{r}\cdot\mathbf{E}(t')|\mathbf{p}'+\mathbf{A}(t')\rangle\langle \mathbf{p}'|\nabla V|\mathbf{p}''\rangle \\ &\quad \times \langle \mathbf{p}''+\mathbf{A}(t'')|\mathbf{r}\cdot\mathbf{E}(t'')|0\rangle \mathrm{e}^{-i(S(\mathbf{p}'',t,t'')-S(\mathbf{p}',t,t')+I_p(t'-t''))}\,. \qquad (3.13)\end{aligned}$$

Employing the identity [108]

$$\int_{t_0}^{t}\int_{t_0}^{t} \mathrm{d}t'\mathrm{d}t'' f(t')g(t'') = \int_{t_0}^{t} \mathrm{d}t' \int_{t_0}^{t'} \mathrm{d}t'' f(t')g(t'') + \int_{t_0}^{t} \mathrm{d}t'' \int_{t_0}^{t''} \mathrm{d}t' f(t')g(t'')\,, \tag{3.14}$$

Eq. (3.13) can be rewritten as

$$\begin{aligned}\mathbf{a_{CC}}(t) &= -\int \mathrm{d}^3p'' \int_{-\infty}^{t} \mathrm{d}t'' \int d^3p' \int_{-\infty}^{t''} \mathrm{d}t' n_0(t') n_0(t'') \langle 0|\mathbf{r}\cdot\mathbf{E}(t')|\mathbf{p}'+\mathbf{A}(t')\rangle\langle \mathbf{p}'|\nabla V|\mathbf{p}''\rangle \\ &\quad \times \langle \mathbf{p}''+\mathbf{A}(t'')|\mathbf{r}\cdot\mathbf{E}(t'')|0\rangle \mathrm{e}^{-i(S(\mathbf{p}'',t,t'')-S(\mathbf{p}',t,t')+I_p(t'-t''))} + \text{c.c.}\,. \qquad (3.15)\end{aligned}$$

The photo-emission matrix elements contained in Eqs. (3.13) and (3.15) can be carried out analytically:

$$\begin{aligned}\langle p_x| - \partial_x V|q_x\rangle &= \frac{i\sqrt{\alpha}}{2\pi^2}\frac{1}{p_x - q_x} \qquad (3.16)\\ \langle p_x| - \partial_x V|0\rangle &= i\sqrt{2}\alpha^{5/4}\big(p_x - \sqrt{\alpha}\arctan(p_x/\sqrt{\alpha})\big)/(\pi p_x^2) \qquad (3.17)\end{aligned}$$

Saddle-point approximation The integrals (3.12) and (3.15) cannot be solved exactly. We apply the saddle-point approximation successively to all integrals over times and momenta in the expressions (3.12) and (3.15) (valid for $\omega \ll I_p \ll U_p$) to carry out the integrals. First, we start with the momentum integration. Note that both momentum integrations in $\mathbf{p}'$ and $\mathbf{p}''$ in Eq. (3.13) are independent in terms of phases. This means the heavily oscillating exponential function can be separated into two parts depending either $\mathbf{p}'$ and $\mathbf{p}''$ and integrated isolatedly. The slowly varying prefactors cannot be factorized in such a way but in the saddle-point approximation they are assumed to be constant around the saddle points. The momentum saddle points are defined via $\nabla_{\mathbf{p}} S = 0$, which yields $p_s(t,t') = -\int_{t'}^{t} d\tau A(\tau)/(t-t')$ for a laser field linearly polarized along the x axis. After the momentum integration, we obtain the following expressions:

$$a_{CB}(t) = i\int_{-\infty}^{t} \mathrm{d}t' n_0(t) n_0(t') \sqrt{\frac{(-2\pi i)^3}{(t-t')^3}} \langle 0|\nabla V|p_s(t,t')+A(t)\rangle \langle p_s(t,t')+A(t')|xE(t')|0\rangle \times \mathrm{e}^{-i(S(p_s(t,t'),t,t')+I_p(t-t'))} \tag{3.18}$$

$$a_{CC}(t) = -\int_{-\infty}^{t} \mathrm{d}t'' \int_{-\infty}^{t''} \mathrm{d}t' n_0(t') n_0(t'') \sqrt{\frac{(-2\pi i)^6}{(t-t')^3(t-t'')^3}} \langle 0|xE(t')|p_s(t,t')+A(t')\rangle \times \langle p_s(t,t')|\nabla V|p_s(t,t'')\rangle \langle p_s(t,t'')+A(t'')|xE(t'')|0\rangle \times \mathrm{e}^{-i(S(p_s(t,t''),t,t'')-S(p_s(t,t'),t,t')+I_p(t'-t''))} + \text{c.c.} \tag{3.19}$$

The time integration is more involved since the ionization matrix elements $\langle 0|x|p\rangle$ possess a singularity at the saddle points $\partial_{t'} S(p_s(t,t'),t,t') = 0$ [and $\partial_{t''} S(p_s(t,t''),t,t'') = 0$ for $\mathbf{a_{cc}}(t)$]. For this reason the identity [68]

$$\langle p_s(t,t')+A(t')|xE(t')|0\rangle = -i\frac{(8I_p)^{5/4}}{8\pi}\frac{\mathrm{d}}{\mathrm{d}t'}\frac{1}{(-\frac{\mathrm{d}}{\mathrm{d}t'}S)^2} \tag{3.20}$$

is employed before we carry out the saddle-point approximation. Plugging (3.20) into Eqs. (3.18) and (3.19) and integrating partially yields

$$a_{CB}(t) = i\frac{(8I_p)^{5/4}}{8\pi}\int_{-\infty}^{t} \mathrm{d}t' n_0(t) n_0(t') \sqrt{\frac{(-2\pi i)^3}{(t-t')^3}} \langle 0|\nabla V|p_s(t,t')+A(t)\rangle \times \mathrm{e}^{-i(S(p_s(t,t'),t,t')+I_p(t-t'))} \Big/ \Big(\frac{\mathrm{d}}{\mathrm{d}t'}S\Big) \tag{3.21}$$

$$a_{CC}(t) = -\frac{(8I_p)^{5/2}}{(8\pi)^2}\int_{-\infty}^{t} \mathrm{d}t'' \int_{-\infty}^{t''} \mathrm{d}t' n_0(t') n_0(t'') \sqrt{\frac{(-2\pi i)^6}{(t-t')^3(t-t'')^3}} \langle p_s(t,t')|\nabla V|p_s(t,t'')\rangle \times \mathrm{e}^{-i(S(p_s(t,t''),t,t'')-S(p_s(t,t'),t,t')+I_p(t'-t''))} \Big/ \Big(\frac{\mathrm{d}}{\mathrm{d}t'}S\frac{\mathrm{d}}{\mathrm{d}t''}S\Big) + \text{c.c.} \tag{3.22}$$

Finally, applying the saddle-point approximation by employing the identity $\int dt\, \mathrm{e}^{iS}/S' = \sum_s \pi i \mathrm{e}^{iS}/S''$ [68, 167], we obtain

$$a_{CB}(t) = -\mathrm{Re}\frac{(8I_p)^{5/4}}{4}\sum_{t'} \sqrt{n_0(t) n_0(t')} w_{corr}(t') D(t,t') \times \langle 0|\partial_x V|p_s(t,t')+A(t)\rangle \mathrm{e}^{-i(S(p_s(t,t'),t,t')+I_p(t-t'))} \tag{3.23}$$

$$a_{CC}(t) = \mathrm{Re}\frac{(8I_p)^{5/2}}{32}\sqrt{n_0(t') n_0(t'')} w_{corr}(t') w_{corr}(t'') D(t,t') D(t,t'') \times \langle p_s(t,t')|\partial_x V|p_s(t,t'')\rangle \mathrm{e}^{-i(S(p_s(t,t''),t,t'')-S(p_s(t,t'),t,t')+I_p(t'-t''))}, \tag{3.24}$$

where

$$D(t,t') = \sqrt{(2\pi i)^3/(t-t')^3}/(\mathrm{d}^2/\mathrm{d}t'^2 S(p_s(t,t'),t,t'))\,, \tag{3.25}$$

$$w_{corr}(t) = \sqrt{w(t)/w_K(t)}\,, \tag{3.26}$$

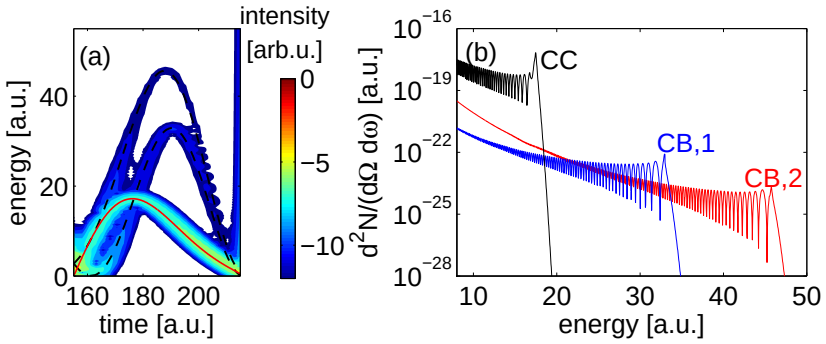

Figure 3.6: CC HHG by using an analytical approach based on the SFA for the same field as in Fig. 3.4. (a) is the windowed Fourier transform of the acceleration within a chosen time window in excellent agreement with the TDSE results of Fig. 3.4. (b) shows single-atom spectral photon yield per solid angle per shot of the same time window as in (a).

and $t' < t''$. The ionization correction factor $w_{corr}(t)$ was empirically inserted [111] as the non-Coulomb corrected SFA contains only the Keldysh ionization rate $w_K(t)$ which is not sufficient in this regime.

Results The analytically calculated dipole acceleration is shown in Fig. 3.6, for the same laser field and in the same window size as for Fig. 3.4. The excellent agreement with the TDSE results [compare Fig. 3.6 with Fig. 3.4] shows that the process is correctly described by the SFA model. It further proves that the origin of the signal is the simultaneous recollision of the continuum wave packets because we constructed the SFA model in that way. Moreover, the SFA model gives a possibility of fast evaluation of the HHG response. It also allows for a phase-matching analysis carried out in the next section.

3.4 Phase-matching properties of continuum–continuum HHG

For a measurement of the CC harmonics it is crucial to learn about their phase–matching behavior. As discussed in Section 2.3, phase-matching does not only depend on the characteristics of the gas medium and the laser field geometry but also on the emission dipole phase. This intrinsic phase has a characteristic intensity dependence that is usually exploited to balance the phase-mismatch employing an intensity gradient in the focus. If the characteristic intensity dependence would be different for the CC harmonics as compared to the CB harmonics, the CC contribution could be selected to be the only macroscopic HHG contribution. The intensity dependence of the emission phase is analyzed by means of our SFA model in a similar way as in Ref. [168]. In general, several quasi-classical trajectories j contribute to the Fourier transformed dipole moment $\tilde{d}(\omega_H)$ at a certain emission frequency ω_H:

$$\tilde{d}(\omega_H) = \sum_j |d_j(I)| \mathrm{e}^{-i\phi_j(I)} \approx \sum_j |d_j| \mathrm{e}^{-i\alpha_j I} \tag{3.27}$$

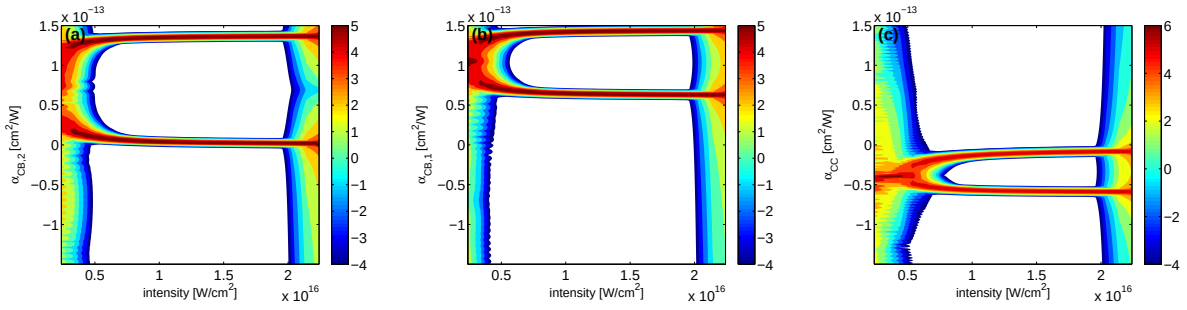

Figure 3.7: Intensity dependence of α of several quantum orbits at the harmonic frequency $\omega_H = 8$ a.u.. The time window between t=150 a.u. and t=220 a.u. is analyzed for the laser pulse shown in Fig. 3.4 (a) where we have 6 different contributions to the energy: short and long trajectory of the second ionization time window (a) and short and long trajectory of the first ionization time window (b) and (c) shows the "short" and "long" trajectory of the CC transition.

where $j = \{CB,1;\ CB,2;\ CC\}$ denotes the different orgins for the transition. $CB,1$ means the CB HHG from a trajectory ionized in the early ionization window (e.g. the red line in Fig. 3.3 (a)) whereas $CB,2$ is from the later ionization window [e.g. the blue line in Fig. 3.3 (a)]. CC marks the contributions from the CC transitions. For energies below the CC cutoff, we have 6 contributions from each branch [see Fig. 3.6]. The intensity dependence of the phase of each contribution is expressed via the parameter α_j defined by $\phi_j(I) = \alpha_j I$.

The phase $\phi_j(I)$ can be determined from the SFA model above. In a second step the expression is Gabor transformed [windowed Fourier transform, similar to the time-frequency analysis of Eq. (3.2)] with respect to intensity I to obtain α_j. For this purpose the intensity-dependence of the phase of d_j can be neglected. The results are shown in Fig. 3.7 for a photon energy of $\omega_H = 8$ a.u. where 6 different contributions exist. (a) and (b) are the usual CB transitions showing two contributions each: long and short trajectory. (a) and (b) differ in their half cycle of ionization: the signals in (a) come from trajectories ionized around $t = 70$ a.u. whereas (b) has an ionization time window around $t = 120$ a.u.. (c) is the intensity dependence of α for the CC transition investigated in this chapter.

The results show that the phase of the CC transition arising from the difference between the two trajectories has a different intensity dependence (c) than the CB transitions (a) and (b).

It can be intuitively explained as follows: In the SFA model the phase of the CC transition

$$\phi_{CC}(I) = S_{CB,1}(p_s(t,t''),t,t'') - S_{CB,2}(p_s(t,t'),t,t') + I_p(t'-t'') - \omega_H t \tag{3.28}$$

is the difference of the phases between both CB transitions (apart from $-\omega_H t$) where S is the action defined in (3.8). The sign between $S_{CB,1}(p_s(t,t''),t,t'')$ and $S_{CB,2}(p_s(t,t'),t,t')$ arises this way because the time derivative of ϕ_{CC} is the photon energy and has to be positive.

$\phi_{CC}(I)$ is apart from $-\omega_H t$ the difference of the phases of the two CB transitions: $\alpha_{CC} \approx \alpha_{CB,2} - \alpha_{CB,1}$. As $\alpha_{CB,i}$ can be intuitively understood as a measure for the

sensitivity of the phase to the laser intensity for the respective trajectory. The sensitivity is much larger for the trajectory that is longer in the continuum which means ionized earlier and, therefore, $\alpha_{CB,1} > \alpha_{CB,2}$. Thus, the sign of α_{CC} is different to the sign of $\alpha_{CB,i}$.

Moreover, α_{CC} has a similar smooth behavior and is of the same order of magnitude. For this reason, we expect that these harmonics can be selectively phase-matched by using certain focusing parameters or a specifically chosen regime in a gas cell and the CB harmonics can be suppressed at the same time.

From Fig. 3.7 we read off the following values: two CB transitions from the wave packet ionized at the first peak of the laser pulse ($\alpha_{CB,1,s} = +0.6 \times 10^{-13}\text{cm}^2/\text{W}$ and $\alpha_{CB,1,l} = +1.5 \times 10^{-13}\text{cm}^2/\text{W}$ for the short and long trajectory, respectively), two CB transitions from ionization at the second peak ($\alpha_{CB,2,s} \to 0$ and $\alpha_{CB,2,l} = +1.4 \times 10^{-13}\text{cm}^2/\text{W}$) and the two CC transitions ($\alpha_{CC,s} = -0.6 \times 10^{-13}\text{cm}^2/\text{W}$ and $\alpha_{CC,l} = -0.1 \times 10^{-13}\text{cm}^2/\text{W}$). As result, and explained by the difference-energy mechanism, the sign of α for CC vs CB harmonics is found to be different and thus allows to experimentally isolate the CC harmonics.

3.5 Applications

In this chapter, we have pointed out that atoms can emit harmonics even in the saturation regime by a new type of HHG transition. By means of our analytical model, the phase-matching behavior of the CC harmonics has been investigated and it is shown that conditions for isolated CC emission could be found. Besides the fundamental interest in understanding HHG, the CC HHG could even be used for applications. Since the CC singal has different properties than the CB signal, it can offer new prospects.

CC HHG may qualitatively advance and complete tomographic molecular imaging: Instead of sensing the orbital shape of the active electron [32, 33], the effective potential could be measured. This is because the detailed structure of the potential enters the CC transition in Eq. (3.25) via the matrix element $\langle p'|\nabla V|p''\rangle$ which is the Fourier transform of the gradient of the effective potential. It is not restricted to an ionic potential but also valid for molecules. From a measurement of the harmonic spectrum this matrix element could be potentially extracted. This could be particularly interesting for larger molecules, where the entire molecular potential, i.e. mainly the positions of all nuclei, would be mapped out, not just the few highest-lying molecular orbitals.

Moreover, it is known that an electron ionized from one isolated atom cannot coherently recombine with another atom to produce CB HHG, as there is no phase relation among isolated atoms. However, the phase of the CC transition does not depend on any bound-state portion of a wave function, only on the shape of the potential. It would allow for coherent interferences in another atomic or more complex potential even if they are some fixed distance away.

Also, CC transitions contribute to harmonic energies below I_p on which currently a frequent discussion exists about their underlying mechanism [169–172].

Additionally, the unique phase-matching behavior could allow for HHG emission in entirely new regimes or different field geometries.

4 Macroscopic relativistic HHG

A theoretical model capable of describing relativistic HHG from macroscopic gas targets is developed. It is applied to two different laser setups. Both are examined, optimized and suitable phase-matching schemes are found. Crucial issues determining the macroscopic HHG yield are discussed in detail.

HHG is a very valuable source of coherent soft x-ray radiation in the nonrelativistic regime. With the state-of-the-art technology, coherent x rays of up to $\sim$ 3 keVs [30] can be generated. A further increase of the photon energy can in principle be achieved by an increase of the laser intensity [see cutoff law Eq. (2.1)]. However, the applicable laser intensity is limited by the relativistic electron drift (see Section 2.1.1) that otherwise results in a dramatic suppression of the HHG efficiency.

Various methods to counteract the relativistic drift have been proposed. However, no universal solution has been found, each method has its drawbacks. To suppress the drift, highly charged ions moving relativistically against the laser propagation direction [70, 71] or a gas of positronium atoms [72, 73] can be used. Different combinations of laser fields have also been proposed for this purpose such as a tightly focused laser beam [173], two counterpropagating laser beams with linear polarization [67, 74, 77] or with equal-handed circular polarization [77, 78]. In the latter field configuration, the relativistic drift is eliminated. However, in this scheme the phase-matching is particularly problematic to realize [79]. In the weakly relativistic regime, the Lorentz force can also be compensated by a second weak laser beam being polarized in the strong beam propagation direction [68]. Two consecutive laser pulses or the laser field assisted by a strong magnetic field have been proposed as well [75, 76] but this requires large magnetic fields and dilute samples. Additionally, it has been pointed out [80–83] that strong attosecond pulse trains (APTs) employed as a driving field for HHG can be very useful to suppress the relativistic drift.

All these efforts have only addressed the emission probability of a single atom rather than coherent emission from a macroscopic gas target. Investigations to determine the photon yield from such gas targets in the relativistic regime still present a gap in existing research.

In this chapter, we examine the feasibility of phase-matched harmonic emission from an underdense plasma of multiply-charged ions for two relativistic HHG setups. Suitable phase-matching schemes for both setups are proposed.

4.1 Macroscopic model for relativistic HHG

4.1.1 Macroscopic HHG yield

In the first part of the chapter, a model is developed to calculate the harmonic spectrum from a macroscopic gas target suitable for relativistic laser intensities. The standard approaches [142, 174] employed in the non-relativistic regime are not applicable because they are based on the dipole moment to calculate the single-atom yield. This approach fails for sufficiently small wavelength because retardation between different emission points become important [175]. Instead of the the single-valued dipole moment, our approach uses the complete current density distribution of each atom. Retardation between different emission points within the distribution are taken into account by a phase factor. The link between the microscopic (atomic) current density $\mathbf{j}$ and the macroscopically emitted harmonic electric field $\mathbf{E}_H$ is obtained from Maxwell's equations [176]:

$$\Delta\mathbf{E}_H - \frac{1}{c^2}\frac{\partial^2\mathbf{E}_H}{\partial t^2} = \frac{4\pi}{c^2}\frac{\partial\mathbf{j}_\perp}{\partial t}. \tag{4.1}$$

The current density was splitted into two parts $\mathbf{j} = \mathbf{j}_\perp + \mathbf{j}_\parallel$ where the longitudinal current density fulfills $\nabla \times \mathbf{j}_\parallel = 0$ and the transversal current density $\nabla \cdot \mathbf{j}_\perp = 0$. Due to the large harmonic frequencies absorption of the harmonic photons can be neglected [174] because their energy is much higher than the largest atomic transition energy. The current density $\mathbf{j}$ will be exclusively determined by the HHG process.

With the following definitions of the Fourier transform (used throughout Sec. 4.1)

$$\tilde{f}(\omega_H) = \int \mathrm{d}t\, \mathrm{e}^{i\omega_H t} f(t) \tag{4.2}$$

$$f(t) = \frac{1}{2\pi}\int \mathrm{d}\omega_H\, \mathrm{e}^{-i\omega_H t}\tilde{f}(\omega_H) \tag{4.3}$$

the wave equation (4.1) can be transformed to Fourier space, yielding

$$\Delta\tilde{\mathbf{E}}_H + k_H^2\tilde{\mathbf{E}}_H = -\frac{4\pi}{c^2}\, i\,\omega_H\,\tilde{\mathbf{j}}_\perp, \tag{4.4}$$

where $k_H = \omega_H/c$. The solution of the equation is acquired by means of the Greens function:

$$\tilde{\mathbf{E}}_H(\mathbf{x}', \omega_H) = i\frac{\omega_H}{c^2}\int \frac{\tilde{\mathbf{j}}_\perp(\mathbf{x}, \omega_H)}{R}\mathrm{e}^{ik_H R}\mathrm{d}^3x \tag{4.5}$$

The complicated near field structure of $\tilde{\mathbf{E}}_H(\mathbf{x}', \omega_H)$ can be very complicated. For calculating the overall HHG photon yield, the knowledge of the far-field spectrum is sufficient. Thus, we can restrict the calculation to the far-field zone ($k_H R \gg 1$) with the approximation [176]:

$$R = |\mathbf{x} - \mathbf{x}'| \simeq x' - \mathbf{x}\cdot\mathbf{n}' \tag{4.6}$$

with being $\mathbf{n}' = \frac{\mathbf{x}'}{x'}$ the unit vector with the direction (ϕ) pointing to the observation point $\mathbf{x}'$. We restrict ourselves to radiation emitted along or with small deviations to the propagation direction of the laser and, therefore, $\mathbf{j} \approx \mathbf{j}_\perp$.

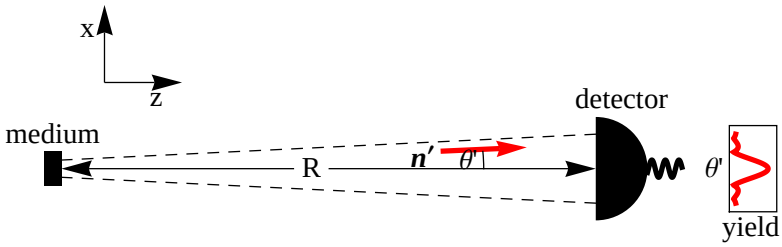

Figure 4.1: Geometry of the medium and detector including the definitions of the coordinates. The dashed lines denote the divergence angle of the harmonic radiation. The box on the right schematically shows the measured angular distribution.

Moreover, the absolute phase of the harmonic electric field at the observation point is not important and can be separated out:

$$\tilde{\mathbf{E}}_{H,0}(\mathbf{n}', \omega_H) = i\frac{\omega_H}{c^2}\int \frac{\tilde{\mathbf{j}}(\mathbf{x}, \omega_H)}{R} \mathrm{e}^{-i\mathbf{k}_H\cdot\mathbf{r}} \mathrm{d}^3x \tag{4.7}$$

where $\mathbf{k}_H = k_H\mathbf{n}'$. The total current density is superimposed by the current densities $\mathbf{j}_a(\mathbf{x}, t, \mathbf{x}_a)$ of the single atoms at $\mathbf{x}_a$:

$$\tilde{\mathbf{j}}(\mathbf{x}, \omega_H) = \rho \int \mathrm{d}^3x_a \int \mathrm{d}t\, \mathbf{j}_a(\mathbf{x}, t, \mathbf{x}_a)\mathrm{e}^{i\omega_H t} \tag{4.8}$$

where ρ is the number density of the atoms. The previous formula (4.8) is based on the assumption of a continuous and homogeneous atomic distribution in space with a number density ρ. Inserting (4.8) into (4.7) yields the final expression for the macroscopically emitted harmonic field

$$\begin{aligned}\tilde{\mathbf{E}}_{H,0}(\mathbf{n}', \omega_H) &= i\frac{\omega_H\rho}{Rc^2}\int \mathrm{d}^3x_a \int \mathrm{d}^3x \int \mathrm{d}t\, \mathbf{j}_a(\mathbf{x}, t, \mathbf{x}_a)\mathrm{e}^{-ik_H\mathbf{x}\cdot\mathbf{n}'+i\omega_H t} &(4.9)\\ &= i\frac{\omega_H\rho}{Rc^2}\int \mathrm{d}^3x_a\, \tilde{\mathbf{j}}_a(\mathbf{x}_a, \omega_H, \mathbf{k}_H). &(4.10)\end{aligned}$$

4.1.1.1 Emitted energy

The overall emitted energy can be obtained via integrating the Poynting vector $\mathbf{S}(\mathbf{r}, t)$ over a surface A (with differential $\mathrm{d}\mathbf{a}$) in the far field

$$W = \int_{-\infty}^{\infty} \mathrm{d}t \int_A \mathrm{d}\mathbf{a}\, \mathbf{S}(\mathbf{x}, t) = \frac{c}{4\pi}\int \mathrm{d}t \int \mathrm{d}a\, \mathbf{E}_H^2(\mathbf{x}, t)\,. \tag{4.11}$$

By plugging

$$\mathbf{E}_H(\mathbf{x}, t) = \frac{1}{2\pi}\int_{-\infty}^{\infty} \mathrm{d}\omega_H \mathrm{e}^{-i\omega_H t}\tilde{\mathbf{E}}_H(\mathbf{n}', \omega_H) \tag{4.12}$$

into (4.11), the energy can be calculated via an integration over the spectrum [177]:

$$W = \frac{c}{4\pi}\int_A \mathrm{d}a \int_{-\infty}^{\infty} \mathrm{d}t\, \mathbf{E}_H(\mathbf{x},t)\frac{1}{2\pi}\int_{-\infty}^{\infty}\mathrm{d}\omega_H \mathrm{e}^{-i\omega_H t}\tilde{\mathbf{E}}_H(\mathbf{n}',\omega_H) \tag{4.13}$$

$$= \frac{c}{8\pi^2}\int_A \mathrm{d}a \int_{-\infty}^{\infty} \mathrm{d}\omega_H \tilde{\mathbf{E}}_H(\mathbf{n}',\omega_H)\int_{-\infty}^{\infty}\mathrm{d}t\, \mathrm{e}^{-i\omega_H t}\mathbf{E}_H(\mathbf{x},t) \tag{4.14}$$

$$= \frac{c}{8\pi^2}\int_A \mathrm{d}a \int_{-\infty}^{\infty} \mathrm{d}\omega_H |\tilde{\mathbf{E}}_H(\mathbf{n}',\omega_H)|^2 \tag{4.15}$$

$$= \frac{c}{4\pi^2}\int_A \mathrm{d}a \int_{0}^{\infty} \mathrm{d}\omega_H |\tilde{\mathbf{E}}_H(\mathbf{n}',\omega_H)|^2 \tag{4.16}$$

Finally, we find the spectrally emitted energy and photon number from (4.16):

$$\frac{\mathrm{d}W}{\mathrm{d}\omega_H} = \frac{c}{4\pi^2}\int_A \mathrm{d}a |\tilde{\mathbf{E}}_{H,0}(\mathbf{n}',\omega_H)|^2 \tag{4.17}$$

$$\frac{\mathrm{d}N}{\mathrm{d}\omega_H} = \frac{c}{4\pi^2\omega_H}\int_A \mathrm{d}a |\tilde{\mathbf{E}}_{H,0}(\mathbf{n}',\omega_H)|^2 \tag{4.18}$$

4.1.2 Single-atom current density

So far, the macroscopic HHG yield has been calculated by means of classical electrodynamics and under the assumption that the atomic current density is known. In order to determine the single-atom contributions via the single-atom current density, relativistic quantum mechanics has to be applied. The Klein-Gordon current density of a particular atom at $\mathbf{x}_a$ in the laser field is given by [178]

$$\mathbf{j}_a(\mathbf{x}_a,x) = \frac{1}{2}\Big(\Psi^*(x)\hat{\mathbf{j}}\Psi(x) + \text{c.c.}\Big) \tag{4.19}$$

where $\hat{\mathbf{j}} = \hat{\mathbf{p}} + \mathbf{A_L}(x)/c$ and the solution $\Psi(x)$ of the Klein-Gordon equation [see Eq. (2.31)]. In the following, "$\cdot$" denotes the product between four-vectors in case no bold symbols are employed. The time-space coordinate is $x = (ct, \mathbf{x})$, the wave vector is $k = (\omega/c, \mathbf{k})$ and the metric tensor is $g_{\mu\nu} = \mathrm{diag}(1,-1,-1,-1)$.

By a Fourier transformation the spectral current is obtained:

$$\tilde{j_a}(\mathbf{x}_a,\omega_H,\mathbf{k}_H) = \frac{1}{c}\int_{-\infty}^{\infty}\mathrm{d}^4x\, \mathbf{j}_a(\mathbf{x}_a,x)\mathrm{e}^{i\omega_H t - i\mathbf{k}_H\mathbf{x}} \tag{4.20}$$

$$= \frac{1}{2c}\int \mathrm{d}^4x\, \Psi^*(x)(\hat{\mathbf{j}}+\hat{\mathbf{j}}^+)\Psi(x)\mathrm{e}^{i\omega_H t - i\mathbf{k}_H\mathbf{x}}\,. \tag{4.21}$$

The "+" in $\hat{\mathbf{j}}^+$ denotes that the operator acts to the left and is complex conjugated.

Inserting the SFA wave-function [134,135] $\Psi_F(x) = \phi(\mathbf{x}-\mathbf{x}_a,t) + \int d^4x' G(x,x')V_L(x')\phi(\mathbf{x}'-\mathbf{x}_a,t')$ and applying the assumptions [128, 179] of neglecting bound-bound and free-free transitions and the time-inverted process results in

$$\tilde{j_a}(\mathbf{x}_a,\omega_H,\mathbf{k}_H)$$

$$\approx \frac{1}{2c}\int \mathrm{d}^4x \int \mathrm{d}^4x' \mathrm{e}^{\mathrm{i}k_H\cdot x}\phi^*(\mathbf{x}-\mathbf{x}_a,t)(\hat{\mathbf{j}}+\hat{\mathbf{j}}^+)G(x,x')V_L(x')\phi(\mathbf{x}'-\mathbf{x}_a,t') \tag{4.22}$$

$$\approx \frac{1}{c}\int \mathrm{d}^4x \int \mathrm{d}^4x' \mathrm{e}^{\mathrm{i}k_H\cdot x}\phi^*(\mathbf{x}-\mathbf{x}_a,t)\hat{\mathbf{j}}G(x,x')V_{AI}(x')\phi(\mathbf{x}'-\mathbf{x}_a,t') \tag{4.23}$$

where $\phi(x) = \frac{\phi_0(\mathbf{x})}{\sqrt{2(c^2-I_p)}} \exp\{-i[(c^2-I_p)t + \mathbf{x}\cdot\mathbf{A}_L/c]\}$ includes the nonrelativistic ground-state wave function $\phi_0(\mathbf{x})$. In the last step, V_L was exchanged by V_{AI} which can justified by means of the Klein-Gordon equation and a partial integration [104,137,179]. Moreover, at this place $\hat{\mathbf{j}}$ and $\hat{\mathbf{j}}^+$ lead to the same result. This can be seen, when the time integration it transformed to phase integration which will be done later [see e.g. (4.40)]. In this case, the space integration becomes the matrix element $\langle 0|\hat{\mathbf{j}}+\hat{\mathbf{j}}^+|\mathbf{p}+\ldots\rangle = 2\langle 0|\hat{\mathbf{j}}|\mathbf{p}+\ldots\rangle$ because $\hat{\mathbf{j}}$ is hermitian.

The Volkov propagator $G(x,x')$ in a plane wave laser field is given as [137, 179]

$$G(x,x') = -i\,\theta(t-t')\int \frac{c\,\mathrm{d}^3\mathbf{q}}{2\varepsilon_{\mathbf{q}}(2\pi)^3}\exp\big[-i\,S_L(x,x')\big] \tag{4.24}$$

with

$$S_L(x,x') = q\cdot(x-x') + \int_{\eta'}^{\eta}\mathrm{d}\tilde{\eta}\left(\frac{(\mathbf{q}+\mathbf{A}(\tilde{\eta})/2c)\cdot\mathbf{A}_L(\tilde{\eta})/c}{k\cdot q}\right), \tag{4.25}$$

where $\eta = k\cdot x$.

Eq. (4.23) can be rewritten to

$$\tilde{j_a}(\mathbf{x}_a,\omega_H,\mathbf{k}_H) = \frac{1}{2c}\sqrt{\frac{\omega_H}{2\pi}}\int \mathrm{d}^4x \int \mathrm{d}^4x'\phi^*(\mathbf{x}-\mathbf{x}_a,t)V_H(x)G(x,x')V_{AI}(x')\phi(\mathbf{x}'-\mathbf{x}_a,t') \tag{4.26}$$

where $V_H(x) = 2\langle 1_H|\mathbf{A}_H(x)/c\cdot[\mathbf{p}+\mathbf{A}_L(x)/c]|0_H\rangle$ and $\mathbf{A}_H(\mathrm{x}) = c\sqrt{2\pi/\omega_H}\hat{\mathbf{e}}_H^* b^\dagger \exp(ik_H\cdot x)$. The current density is now in an analogous form to the HHG emission matrix element (see e.g. [81, 82, 179])

4.1.2.1 Electronic wave function

The wave function of an electron in a plane wave laser field is known analytically [see Volkov propagator (4.24)]. In order to make phase-matching possible, it might be necessary to add additional laser fields or to have spatial inhomogeneities in the laser field. Perturbations of the pure plane wave field $\mathbf{A}_L(\eta)$ can be taken into account by an expansion of the action and the application of the eikonal approximation [180].

The electronic wave function is described by the Klein-Gordon equation

$$(\partial^\mu\partial_\mu + c^2)\Psi(x) = V\Psi(x) \tag{4.27}$$

where $V = V_L + V_p$ is the sum of the potential of the laser and the perturbative laser field and $V = 2i\frac{\mathbf{A}(\eta)}{c}\nabla - A^2(\eta)/c^2$ and $\mathbf{A}(\eta,z) = \mathbf{A}_L(\eta) + \mathbf{A}_p(\eta,z)$. In order to solve the equation, the ansatz

$$\Psi(x) = \exp(i(S_L+S_p)) \tag{4.28}$$

is employed assuming that S_L is given by (4.25). Thus, $\exp(iS_L)$ solves the unperturbed equation where $\mathbf{A}(\eta,z) = \mathbf{A}_L(\eta)$. Inserting the ansatz (4.28) into (4.27), one finds

$$\begin{aligned}\frac{1}{c^2}[i\partial_t^2 S_p - 2\partial_t S_L\partial_t S_p - (\partial_t S_p)^2] - [i\nabla^2 S_p - 2\nabla S_L\nabla S_p - (\nabla S_p)^2] \\ = -2\frac{\mathbf{A}_L}{c}\nabla S_p - 2\frac{\mathbf{A}_p}{c}\nabla(S_L+S_p) - \frac{A_p^2}{c^2} - 2\frac{A_L A_p}{c^2}.\end{aligned} \tag{4.29}$$

We apply the eikonal approximation to the former equation by assuming that V_p changes in space much slower than the wave function and $V_p \ll V_L$. The former condition is equivalent to $\nabla^2 S_p \ll (\nabla S_p)^2$ and we can drop $i\nabla^2 S_p$. The term $-(\nabla S_p)^2$ can be omitted because $\nabla S_L \gg \nabla S_p$. With analogous arguments the terms $i\partial_t^2 S_p$ and $-(\partial_t S_p)^2$ can be neglected. This yields the equation

$$2\frac{A_L A_p}{c^2} + \frac{A_p^2}{c^2} + 2\frac{\mathbf{A}_p}{c}\nabla S_L = \frac{2}{c^2}\partial_t S_L \partial_t S_p + \Big(-2\nabla S_L - \frac{2}{c}(\mathbf{A}_L + \mathbf{A}_p)\Big)\nabla S_p\,, \tag{4.30}$$

that can be solved by the method of characteristics when introducing a parameter u and comparing it to

$$\frac{\mathrm{d}}{\mathrm{d}u}\tilde{S}_p(u) = \partial_t S_p \frac{\partial t(u)}{\partial u} + \nabla S_p \frac{\partial \mathbf{r}(u)}{\partial u}. \tag{4.31}$$

From the comparison the following relation can be found

$$-2k\cdot p = \mathbf{k}\tfrac{\partial \mathbf{r}}{\partial u} - \omega\tfrac{\partial t}{\partial u} \tag{4.32}$$

$$\Rightarrow u = -(\mathbf{kr} - \omega t)/(2k\cdot p) = \eta/(2k\cdot p) \tag{4.33}$$

which yields

$$S_p \;=\; \int_{\eta_0}^{\eta} \mathrm{d}\tilde{\eta}\frac{(\nabla S_L + \mathbf{A}_L(\tilde{\eta})/c + \mathbf{A}_p(\tilde{\eta}, z(\tilde{\eta},\eta))/(2c))\mathbf{A}_p(\tilde{\eta}, z(\tilde{\eta},\eta))/c}{k\cdot p}\,. \tag{4.34}$$

Therefore,

$$S = S_L + S_p = \int_{\eta_0}^{\eta} \mathrm{d}\tilde{\eta}\frac{(p_x + A(\tilde{\eta}, z(\tilde{\eta},\eta))/(2c))A(\tilde{\eta}, z(\tilde{\eta},\eta))/c}{k\cdot p}\,, \tag{4.35}$$

where $A(\eta, z(\tilde{\eta},\eta)) = A_L(\eta) + A_p(\eta, z(\tilde{\eta},\eta))$ and we find from the characteristics

$$\begin{aligned} z(\tilde{\eta},\eta) \;=\; & z - \int_{\eta_0}^{\eta}\mathrm{d}\eta'\frac{1}{k\cdot p}\left(p_z + \frac{k}{k\cdot p}\Big(p_x + \frac{A_L(\eta')}{2c}\Big)\frac{A_L(\eta')}{c}\right) \\ & + \int_{\eta_0}^{\tilde{\eta}}\mathrm{d}\eta'\frac{1}{k\cdot p}\left(p_z + \frac{k}{k\cdot p}\Big(p_x + \frac{A_L(\eta')}{2c}\Big)\frac{A_L(\eta')}{c}\right). \end{aligned} \tag{4.36}$$

The integral in (4.36) can be omitted in case the z-dependence of A_p along the trajectory is negligible.

After these general considerations, we discuss two different setups to generate relativistic harmonics in the remainder of this chapter in detail.

4.2 Relativistic phase-matched HHG from counterpropagating APTs

One promising proposal for a relativistic HHG setup is to employ two counterpropagating attosecond pulse trains (APTs) discussed in detail for a single atom in [82,83]. We advance this investigation by considering the emission from a whole gas target. Therefore, the theory developed in Section 4.1 is applied.

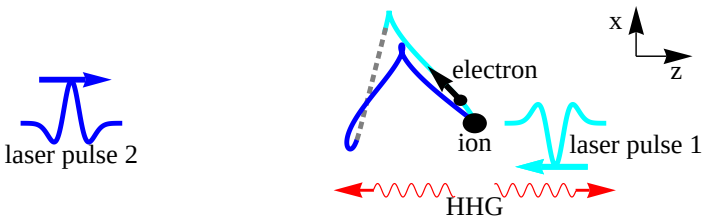

Figure 4.2: The HHG setup with counterpropagating APTs from single-atom perspective: The classical trajectory of a rescattered electron of a single atom in the gas target. After ionization by pulse 1 it is driven in the same pulse (light blue), propagates freely after the pulse has left (gray dashed) and is driven back to the ion by the second laser pulse (dark blue).

4.2.1 Single-atom perspective

The applied setup for relativistic HHG is shown in Fig. 4.2. The driving fields are two counterpropagating APTs consisting of 100 as pulses with a peak intensity of the order of 10^{19} W/cm^2 and a spectral range of about 20eV. Such pulses could be generated in the future by employing the relativistic oscillating mirror of an overdense plasma surface in a strong laser field [181, 182] which can have a HHG efficiency approaching a few percent for harmonics less than 100 eV, as particle-in-cell simulations show [183].

As HHG target medium, an underdense plasma of O^{6+} ions (ionization potential $I_p = 27.18$ a.u.) is used where the laser field strength is in the tunneling regime for the bound electron. Neutral atoms are not able to emit relativistic harmonics since the strong electric field strength ionizes the ground-state wave function rapidly and the ground-state population is depleted before parts of the continuum wave function can recollide. This suppresses HHG from the outer shell electrons (see [102, 184] and Sec. 2.1 and 3.1.1). The plasma is immediately formed when the first laser pulse of relativistic intensity is applied to a neutral atomic gas. This is because the outer shell electrons of an oxygen atom are almost instantaneously ionized due to a much smaller binding potential (0.5 a.u. – 5.1 a.u.) in contrast to the two remaining electrons in the $1s$-shell. HHG is produced only by the tightly-bound inner electron having an ionization potential large enough to prevent saturation but small enough to allow for tunneling at the considered relativistic intensities. The O^{6+} emission is slightly reduced by the depletion to O^{7+} on a few percent level. The O^{7+} emission is not phase-matched in the proposed phase-matching scheme that is introduced below.

First, we concentrate on describing the generation process in view of a single atom, see Fig. 4.2. The electron is liberated by the first pulse, driven by the pulse in the continuum and undergoes the relativistic drift. This part of the trajectory is indicated by the light blue coloring [in Fig. 4.2]. Thereafter, the electron propagates freely (gray dashed) in the continuum. A moment later, the second pulse reaches the electron, it reverts the drift and realizes rescattering (dark blue). The drift compensation is very efficient as one can deduce from Fig. 4.3 (a): the single-atom spectral emission rate of the present setup is calculated twice. Once fully relativistically (black) and second (blue) within the dipole approximation (DA) where the drift is neglected. The heights of the plateaus

coincide meaning that the setup exhibits no significant drift any more. Note that in the DA calculation the relativistic mass shift is included via the leading kinetic energy part of the Hamiltonian [116, 178] $H_{kin} = \sqrt{\mathbf{p}^2c^2 + c^4} - c^2 \approx \mathbf{p}^2/2 - \mathbf{p}^4/(8c^2)$. The rate for the applied setup [the black curve in Fig. 4.3 (a)] is much larger than the one for a conventional laser field [the black curve in Fig. 4.3 (b)] with the same cutoff. In the latter case, due to the drift, the rate would drop rapidly with increasing laser intensity. When comparing both DAs (blue curves), we observe a small suppression of the discussed setup compared to the conventional field because the recolliding classical trajectories start in a smaller relative time window compared to a conventional sinusoidal field. In our scheme only a small fraction of the starting trajectories actually reencounters the core, whereas for a sinusoidal field half of the trajectories revisit the ion [see Fig. 2.1 a)]. On the other hand, the pulse shape of the APT offers an increased ionization probability in this time window but the first effect is stronger. The laser field strength of the discussed setup ($E_0 = 21$ a.u.) is higher than for a conventional setup ($E_0 = 2.7$ a.u.) to reach the same cutoff. It is caused by the larger center frequency of the APT that lowers the ponderomotive potential $U_p = (E_0/2\omega)^2$.

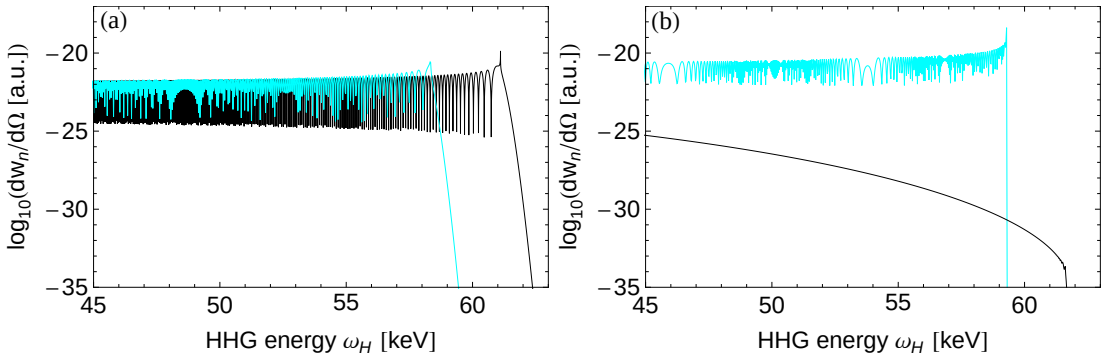

Figure 4.3: Single-atom HHG rates via [82]: (a) represents the discussed setup (Fig. (4.2)) either fully relativistically (black) or in DA including the relativistic mass shift (blue); the delay between the two pulses of the APT is 1.5 fs, the laser field strength $E_0 = 21$ a.u., and $I_p = 27.18$ a.u. (O^{6+}); (b) displays the scenario for a conventional propagating laser field (black) with $E_0 = 2.7$ a.u., $I_p = 7.35$ a.u. (hydrogen-like ion), and (blue) the latter within the DA including the relativistic mass shift. The indicated parameters are chosen such that both the cutoffs and the average ADK-tunneling rates are the same for the two fully relativistic curves [black curves in (a) and (b)].

4.2.2 Macroscopic perspective

We continue to describe the macroscopic properties of the setup. The contributions of different parts of the medium to the harmonic emission are shown in Fig. 4.4. As in common HHG scenarios, the medium mainly emits along the driving field propagation axis (z-axis) to the left as well as to the right direction for symmetry reasons. As the emission mechanism is symmetric towards both directions, we can concentrate on the emission to the right direction. In this case, recombination has to be necessarily arranged by a pulse also propagating to the right because then the emitted harmonics and the pulse triggering

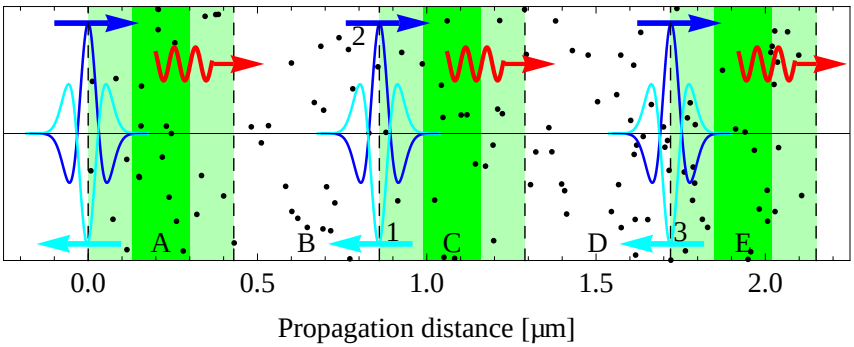

Figure 4.4: The HHG setup with counterpropagating APTs from a macroscopic perspective: the small dots denote the atoms. The two driving APTs are shown in different blue color shades at the moment of overlap. The arrows indicate their propagation direction. The medium is divided into different zones separated by the dashed lines and indicated by A,B,C,D,E. The harmonics emitted from the green (dark) area propagate along the red (wavy) arrow. HHG from shaded (light green) areas is damped.

recollision propagate in the same direction. Opposite directions would result in a strong phase-mismatch. Fig. 4.4 shows the setup at the time when the counterpropagating APTs overlap. All ions in the shaded zones (A,C,E) have previously experienced a pulse (e.g. pulse 1 or 3) propagating to the left and have potentially been ionized by such a pulse. Next, these parts of the medium will experience a pulse propagating to the right and emission in this direction will be possible until other pairs of pulses overlap (e.g. 2 and 3). Thereafter, the white zones (B,D) fulfill the requirement of emission to the right. Note that contributions of atoms experiencing two pulses simultaneously (light shaded areas) are frustrated due to the chaotic trajectories of the ionized electrons in this region [185]. This limits the volume in longitudinal direction to about 1/3 of its complete length and thus the possible pulse delays are between $1-2$ fs.

4.2.3 Mathematical model

The driving APTs are assumed to be plane waves and are numerically propagated in one dimension in the relativistic free electron background using the finite difference method. We use the following equation [174]:

$$2\frac{\omega^2}{c^2}\frac{\partial \tilde{A}_L(z,\omega)}{\partial z} = F\left\{\frac{\omega_p^2(z,t')}{c^3}\frac{\partial_{t'}A_L(z,t')}{\sqrt{1+\frac{1}{2}\frac{A_L^2(z,t')}{c^4}}}\right\}, \tag{4.37}$$

where $t' = t - z/c$ is the time coordinate in a moving grid and F is the Fourier transform operator with respect to t'. The equation is derived in [174] for the electric field with the assumption of a slowly varying envelope. We transformed the equation from the electric field ($E_L = -\partial_t A(t)/c$) to the vector potential because it is required to calculated the current density (4.26). Additionally, we empirically inserted the factor

$1/\sqrt{1+\frac{1}{2}\frac{A_L^2(z,t')}{c^4}}$ [186,187] to account for the relativistic mass shift modifying the plasma frequency ω_p.

The laser field is assumed to be independent from the transversal coordinate, i.e., loose focusing conditions are imposed. A tight focusing would result in a large phase-mismatch (see Sec. 2.3). A consequence of the plasma dispersion is the deformation of the pulse shape as demonstrated in Fig. 4.5. Therefore, the plasma density is limited to a maximum value that the deformed pulse shapes still fulfill the recollision scheme: when the difference between the two pulses driving the process becomes too large, the relativistic drift cannot be compensated. Moreover, we assume that the density of the free electrons is constant because O^{6+} is almost instantaneously reached and the outer shell ionization time of the $1s$ electrons is small compared with the laser period.

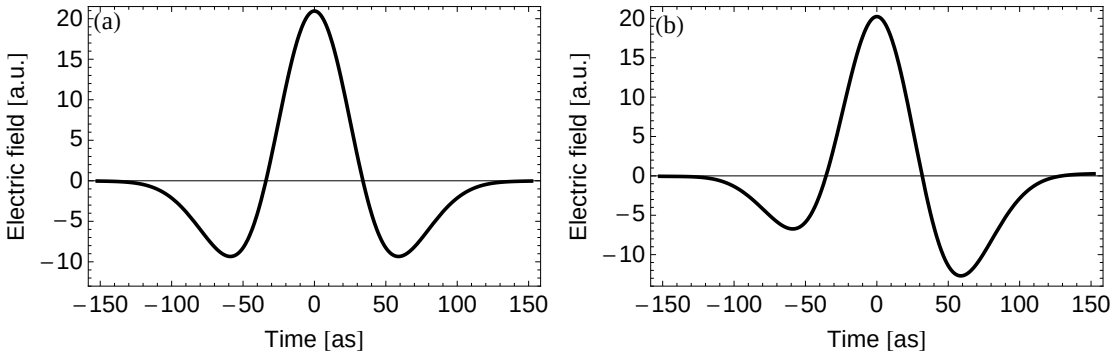

Figure 4.5: (a) Initial electric field of the laser pulse; (b) laser pulse after a propagation length of 12.5μm through a plasma of O^{6+} with a number density of $10^{19}/\text{cm}^3$.

In order to find the overall HHG yield, the spectral photon number $\frac{\mathrm{d}N}{\mathrm{d}\omega_H}$ in the far field is calculated via (4.18) and via the spectral electric field (4.10). The last expression is a spatial integral over all single-atom current densities. The emitted harmonics have the same polarization direction (along the x-axis) as the incident laser field. The x-component of the spectral electron current density of a single multiply charged ion in a modified version of Eq. (4.26) is given by:

$$\tilde{j_a}(\mathbf{x}_a,\omega_H,\mathbf{n}') = \frac{1}{2c}\sqrt{\frac{\omega_H}{2\pi}}\int \mathrm{d}^4x \int \mathrm{d}^4x' \phi^*(\mathbf{x}-\mathbf{x}_a,t)V_H(x)G(x,x')\kappa(t')V_{AI}(x')\phi(\mathbf{x}'-\mathbf{x}_a,t'), \tag{4.38}$$

We included a tunneling correction factor $\kappa(t)=\sqrt{w_{ADK}(t)/w_K(t)}$ upgrading the Keldysh tunneling rate $w_K(t)$ contained in the SFA to fit the ADK-ionization rate [111]. As discussed, we only consider the relevant scenario of interaction in which the electron is initially driven by one pulse and then taken by the second counterpropagating pulse realizing the rescattering with the atomic core, i.e., the electron successively moves in different counterpropagating pulses. Accordingly, in each stage of the excursion, we approximate the Green function by the Volkov Green function $G(x,x')$ in a field of the appropriate single attosecond pulse (see [82]):

$$G(\mathrm{x},\mathrm{x}') \approx i\int \mathrm{d}^3\mathbf{x}^B G_2^V(\mathrm{x},\mathrm{x}^B)\overleftrightarrow{\partial}_{ct^B} G_1^V(\mathrm{x}^B,\mathrm{x}'), \tag{4.39}$$

where $G^V_{1,2}(\mathrm{x},\mathrm{x}')$ are the Volkov Green functions [137, 179] for the electron motion in the first and second pulses, respectively. The time-space coordinate $\mathrm{x}^B = (ct^B, \mathbf{x}^B)$ indicates the intermediate moment between the two pulses when the first laser pulse has already left the wave packet of the active electron and the second laser pulse has not acted yet.

The space integration in (4.38) is shifted by $\mathbf{x}_a$ and an integral transformation to the phases ($\eta'' = \omega t + k_L z'$ and $\eta' = \omega t - k_L z'$, where $k_L = \omega/c$) of the counterpropagating laser fields is applied. It yields

$$\begin{aligned}
&\tilde{j_a}(\mathbf{x}_a, \omega_H, k_H\hat{\mathbf{z}}) \\
= \; & -i\int_{-\infty}^{\infty} \mathrm{d}\eta' \int_{-\infty}^{\eta'} \mathrm{d}\eta'' \int \mathrm{d}^3\mathbf{q}\, m^H(\mathbf{q},\eta',\eta'') \\
& \times \exp\Big\{ -i\big[S_2(\mathbf{x}_a,\mathbf{p},\eta',t^B - z_0^B/c) + S_1(\mathbf{x}_a,\mathbf{p},t^B + z_0^B/c,\eta'') \\
& \qquad +2(\varepsilon_{\mathbf{p}} - c^2 + I_p)z_0^B/c - \omega_H/\omega\eta' + \mathbf{k}_H\mathbf{x}_a\big]\Big\}
\end{aligned} \tag{4.40}$$

where

$$\begin{aligned}
& m^H(\mathbf{p},\eta',\eta'') = \frac{c^2(p_x + A_{L,2}(\mathbf{x}_a,\eta' - \mathbf{k}_L\mathbf{x}_a)/c)}{2\varepsilon_{\mathbf{p}}\omega^2} \\
& \times \left\langle 0|\mathbf{p} + \frac{\mathbf{A}_{L,2}(\mathbf{x}_a,\eta' - \mathbf{k}_L\mathbf{x}_a)}{c} - \frac{\hat{\mathbf{k}}_L}{\omega}(\varepsilon_{\mathbf{p}} + I_p - c^2)\right\rangle \\
& \times \left\langle \mathbf{p} + \frac{\mathbf{A}_{L,1}(\mathbf{x}_a,\eta'' + \mathbf{k}_L\mathbf{x}_a)}{c} + \frac{\hat{\mathbf{k}}_L}{\omega}(\varepsilon_{\mathbf{p}} + I_p - c^2)\,|V|\,0\right\rangle,
\end{aligned} \tag{4.41}$$

and $S_i(\mathbf{x}_a,\mathbf{p},\eta,\eta') = \int_{\eta'}^{\eta} \mathrm{d}\tilde{\eta}\,(\tilde{\varepsilon}_{\mathbf{p},i}(\mathbf{x}_a,\tilde{\eta}) - c^2 + I_p)/\omega$ the quasiclassical action with the electron energy in the laser field $\tilde{\varepsilon}_{\mathbf{x}_a,\mathbf{p},i}(\eta) = \varepsilon_{\mathbf{p}} + (\mathbf{p} + \mathbf{A}_{L,i}(\mathbf{x}_a,\eta \pm \mathbf{k}_L\mathbf{x}_a)/2c)\cdot\mathbf{A}_{L,i}(\mathbf{x}_a,\eta \pm \mathbf{k}_L\mathbf{x}_a)/(c\Lambda_i(\mathbf{p}))$. The subindex i denotes whether the pulse propagates to the left or right.

Eq. (4.40) is evaluated in the saddle-point approximation because the tunneling regime applies. Using $\tilde{j_a}(\mathbf{x}_a,\omega_H,\mathbf{k_H}) = \tilde{j_a}(\mathbf{x}_a,\omega_H,k_H\hat{\mathbf{z}})\exp(-i(k_{H,x}x_a + k_{H,y}y_a))$, the emitted harmonic field from (4.10) is found to be

$$\tilde{E}_0(\mathbf{r}',\omega_H) = i\frac{\omega_H}{c^2R}\rho F(k_h,\theta,r_m)\int \mathrm{d}z_a \tilde{j_a}(z_a,\omega_H,k_H\hat{\mathbf{z}}) \tag{4.42}$$

where

$$\begin{aligned}
F(k_h,\theta,r_m) &= \int \mathrm{d}x_a \int \mathrm{d}y_a \exp(-i(k_{H,x}x_a + k_{H,y}y_a)) \\
&= \int \mathrm{d}\phi_a \int \mathrm{d}r_a \exp\left(-ik_H r_A \sin\theta\, \cos\phi_a\right) \\
&= 2\pi r_m^2 \frac{J_1(k_H r_m \sin\theta)}{k_H \sin\theta r_m},
\end{aligned} \tag{4.43}$$

the Bessel function J_1 of first order and r_m the radius of the cylindrical medium. We assumed a homogeneous current density in radial direction.

4.2.4 Intrinsic harmonic phase

It is crucial for a considerable macroscopic yield that phase-matching is achieved. Mathematically, it reflects a negligible phase variation $\Delta\varphi$ of the integrand in (4.42) along the propagation length: $\Delta\varphi = \Delta \arg \tilde{j}_a \ll \pi$. This phase is calculated for the considered case of the two counterpropagating laser pulses depending on the position in the gas and displayed in Fig. 4.6. We observe a strong phase variation of much larger than π along a distance of much less than $1\,\mu$m ($= 20000$ a.u.). The coherence length is only few atomic units. This translates into a heavily oscillating integrand of the phase-matching integral (4.42) and results in an extensive cancellation between emissions from different atoms.

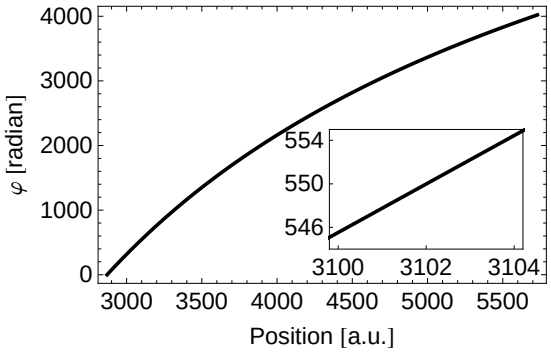

Figure 4.6: The figure displays the phase of the current density $\arg \tilde{j}_a$ depending on the position in propagation direction for the parameters mentioned in the main body of the text. The inset is the same but on a different scale.

We examine the phase difference of the harmonics emitted from different ions separated by a distance Δz along the propagation direction derived from (4.40):

$$\Delta\varphi = \Delta \arg \tilde{j}_a \approx \Delta z \left(\frac{\omega_H}{c} \frac{\Delta v_g}{v_g} - \frac{\partial \varphi_i}{\partial z} \right) \tag{4.44}$$

The first term describes the phase-mismatch due to the free electron dispersion with $\Delta v_g = \omega_p^2 / 2\omega_H^2$, ω_p being the electron plasma frequency and v_g the group velocity of the driving laser pulse, whereas the last term φ_i is the single-atom emission phase depending on the laser field conditions [188] (see Sec. 2.3). This intrinsic phase φ_i is determined by the classical action of the electron trajectory recolliding with the specific harmonic energy and is an integral over the electron's energy in the laser field plus the binding energy. To illustrate our numerical results, the integral can be estimated as $\varphi_i \approx (\alpha U_p(\mathbf{x}_a) + I_p)\tau(\mathbf{x}_a)$, with the local ponderomotive potential $U_p(\mathbf{x}_a) = (E_0(\mathbf{x}_a)/2\omega_0)^2$, the electron excursion time $\tau(\mathbf{x}_a)$, a numerical constant α, the local laser field amplitude $E_0(\mathbf{x}_a)$ and a central frequency of ω_0. Thereby, we take into account that during the relativistic motion in the laser field, the electron energy is proportional to $(E_0/\omega_0)^2$, see, e.g., Ref. [114]. $\alpha U_p(\mathbf{x}_a)$ estimates the average electron energy in the short laser pulse. In fact, the harmonic single-atom cutoff of this field configuration can be estimated in good approximation by $3.2\,U_p + I_p$.

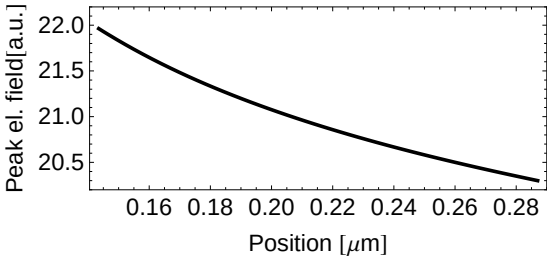

Figure 4.7: The figure displays the optimized peak electric field variation in the first interaction zone (A in Fig. 4.4). The excursion time increases to the right.

Thus, φ_i depends on the laser intensity as well as on the delay between the two pulses. The latter, being unique for this laser setup, mainly affects the electron excursion time $\tau(\mathbf{x}_a)$ and varies along the propagation direction. In order to achieve phase-matching, one can vary the laser intensity along the propagation direction to balance the intrinsic phase with the phase slip due to dispersion. The intensity variation required for a constant complex phase of $\arg \tilde{j}_a$ within the entire medium is calculated numerically and shown in Fig. 4.7 for the first interaction zone. It is optimized for the long trajectory of 50 keV energy but could be accomplished for any energy value below. Note that only one of the short and long trajectories can be phase-matched since their classical actions are different. The eikonal-Volkov approximation [180, 189] (see Sec. 4.1.2.1) is applied for the analytical description of the spatial variations of the laser field in the expression for $G(x, x')$. This is justifiable because the additional driving field causing the modulation perturbs the electron energy only slightly. Consequently, the second derivatives of the additional phase of the electron wave function as well as the square of the additional phase are neglected in the Klein-Gordon equation. The experimental realization of the phase-matched scheme could be achieved, e.g., with a modulated hollow core waveguide.

4.2.5 Emission spectrum

We employ a medium length as short as the spatial extent of the APT to minimize dispersion. In our simulation, each APT consists of 15 pulses with an APT duration of 40 fs. Our calculations show that in the case of longer APTs, the pulses in the train strongly spread due to dispersion and overlap, thus, violating the condition for the drift compensation. All pairs of pulses have almost the same coherent contribution to the overall yield. Since the pulses in different zones have experienced a different propagation length through the plasma, their shapes slightly differ. However, phase-matching still can be maintained by slightly adjusting the modulation profile, as long as the pulse shape still fulfills the recollision scheme. The phase-matching scheme imposes a strong demand on the jitter of the laser field $\Delta E/E$: $\Delta U_p \tau \ll 1$ yields $\Delta E/E \ll (U_p \tau)^{-1} \sim 10^{-4}$. We chose a gas density of $\rho = 10^{19}/\mathrm{cm}^3$ (ionized by the laser as described before), a diameter of 1 mm and a length of 12.5 μm for the interaction volume.

The emitted spectral photon number is shown in Fig. 4.8. An integral over the spectrum yields an emitted photon number of 10^{-7} at 50 keV per one collision of APTs which

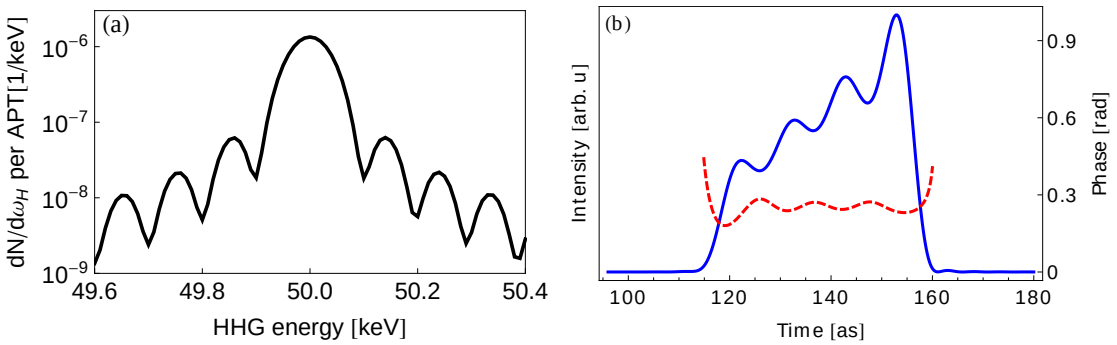

Figure 4.8: (a) Emitted spectral photon number [via (4.18)] of the setup for the medium described in the text. Note that spikes at integer multiples of ω do not appear due to a local averaging. (b) displays the emitted HHG pulse. The blue line is the intensity whereas the dashed red line is the nonlinear phase of the HHG pulse. The latter has only small variation and thus the pulse is near to its bandwidth-limited duration.

corresponds to a signal of about 10 photons per day at a assumed 1 kHz repetition rate. Note that the choice of the atomic species is rather flexible. Multi-electron highly charged ions offer an enhanced recombination probability due to core polarization [109], but produce a larger electron background that can be balanced by a lower gas density. The overall efficiency is maintained or could even be enhanced. The bandwidth of phase-matched HHG in this scheme is about 150 eV near the cutoff and pulses with a duration of about 35 as can be produced.

4.2.5.1 Formula for estimating the photon yield

Before continuing to discuss the small HHG yield, we show how the emitted photon number can be estimated without the extensive calculation above:

$$N = \frac{\mathrm{d}w_n}{\mathrm{d}\Omega} \times \Delta N \times \Omega \times \Delta t \times V^2 \rho^2 N^3 \tag{4.45}$$

Here, $\frac{\mathrm{d}w_n}{\mathrm{d}\Omega}$ is the single-atom emission rate that can be calculated from [82] for the present setup and is similar to the single-atom current density Eq. (4.38), ΔN is the phase-matched frequency bandwidth, Δt the interaction time that is approximately the delay between both pulses, ω_H the angular frequency of the emitted harmonics, V the volume if coherently emitting atoms, ρ the atomic density and N the number pulses per train.

Equation (4.45) states that the harmonic yield scales as $\sim N^3$ with the number of pulses per train. Every pulse of the first train interacts with N pulses of the other train. All N contributions add up with the same phase (phase-matching provided). Contributions from other pulses of the first train are phase-shifted by $\mathrm{e}^{in2\pi}$. Therefore, the totally emitted energy is proportional to

$$\left|\sum_{j=0}^{N-1} N\mathrm{e}^{in2\pi j}\right|^2 = \left|N\frac{1-\mathrm{e}^{in2\pi N}}{1-\mathrm{e}^{in2\pi}}\right|^2 = N^2\frac{\sin^2(Nn2\pi)}{\sin^2(n2\pi)} \tag{4.46}$$

neglecting the frequency dependence of the other factors. An averaging over n of the previous formula yields the factor N^3 in (4.45).

To estimate the photon number via (4.45), numerical values for each factor are needed: the single atom emission rate is $\frac{\mathrm{d}w_n}{\mathrm{d}\Omega} \approx 10^{-22}$ [see Fig. 4.3 (a)]; the phase-matched frequency bandwidth can be deduced from Fig. 4.8 (a): $\Delta\omega_H \approx 0.1\,\mathrm{keV} \rightarrow \Delta N \approx 10^2 th$; the solid angle in the far field is determined by the interference pattern of a circular aperture $\Omega = \phi^2 = (\frac{2.4}{r_a}\frac{\lambda_H}{2\pi})^2 \approx 10^{-16}$, where $\omega_H = 50\,\mathrm{keV}$ and medium radius $r_a = 10^7$a.u. are assumed; the interaction time $\Delta t \approx 10^2$ a.u. can be approximated by the delay between both pulses; the volume is cylindrical $V_{zone} = \pi r_a^2 \Delta z_a = \pi\, 10^{14} \times 3 \times 10^3 = 10^{18}$ and, therefore, $V^2 \approx 10^{36}$; the plasma density restricted by the dispersion is $n_A = 10^{19}/\mathrm{cm}^3$; assuming that the APT was generated by a 30 fs fundamental pulse, it consists of $N = 15$ attosecond pulses.

Taking all parts together, the emitted photon number is

$$\begin{aligned} N &= \frac{\mathrm{d}w_n}{\mathrm{d}\Omega}\Big|_{long} \times \Delta N \times \Omega \times \Delta t \times V_{zone}^2 \rho^2 N^3 \\ &= 10^{-22} \times 10^2 \times 10^{-16} \times 10^2 \times 10^{36} \times 10^{-12} \times 10^3 \\ &= 10^{-7} \end{aligned} \tag{4.47}$$

in agreement with the previous accurate calculation. This kind of estimation can be performed for other HHG experiments with different laser configurations as well. For instance, we can use the experimental parameters of [40] where in an efficient way 80 as pulses were generated. We can estimate the emitted photon number

$$\begin{aligned} N &= \frac{\mathrm{d}w_n}{\mathrm{d}\Omega}\Big|_{long} \times \Delta N \times \Omega \times \Delta t \times V_{zone}^2 \rho^2 \\ &= 10^{-17} \times 10^1 \times 10^{-9} \times 10^2 \times 10^{41} \times 10^{-12} \\ &= 10^{+6} \end{aligned} \tag{4.48}$$

The large ratio between (4.47) and (4.48) arises mainly due to the single-atom yield $\frac{\mathrm{d}w_n}{\mathrm{d}\Omega}$, the emission angle Ω and the phase-matching volume. Please note that in the same way as the emission angle decreases from (4.47) to (4.48), the phase space volume contained in $\frac{\mathrm{d}w_n}{\mathrm{d}\Omega}$ decreases. Therefore, the actual decrease of the other factors in $\frac{\mathrm{d}w_n}{\mathrm{d}\Omega}$ is much larger. In the following, these factors are analyzed.

4.2.6 Efficiency analysis

The small magnitude of the harmonic signal compared with current xuv HHG yields (e.g., [40]) can be explained by investigating the general expression for the spectral HHG photon rate $\dot{N}_n$ for phase-matched emission [80, 81, 111] of the harmonic order $n = \omega_H/\omega$ from a fixed gas volume

$$\dot{N}_n \sim w_i(t_i)\, |\langle 0|V_H|\mathbf{p}\rangle|^2\, (v_\perp^2 \tau^2 \partial\omega_H/\partial t_i)^{-1}. \tag{4.49}$$

Here, $w_i(t_i)$ is the ionization rate with the ionization time t_i, $\langle 0|V_H|\mathbf{p}\rangle$ is the recombination amplitude and the last factor accounts for the dynamical properties of the wave. $v_\perp^2 \tau^2$ is

the transversal cross section of the recolliding electronic wave packet where transversal spreading velocity is $v_\perp$, and τ is the excursion time of the electron. $\partial\omega_H/\partial t_i$ is the so-called electron wave packet chirping factor which is illustrated in Fig. 4.9 and is described in Sec. 6.2.1 in detail.

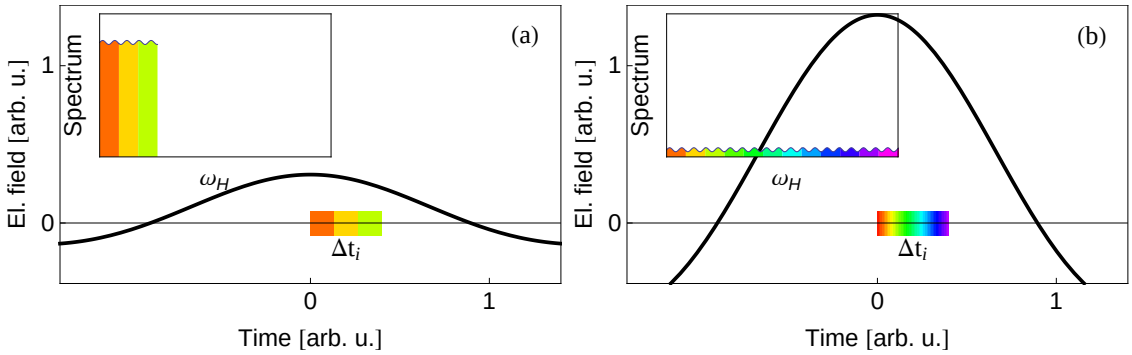

Figure 4.9: Schematic illustration of the chirping factor $\partial\omega_H/\partial t_i$: the harmonic bandwidth per unit ionization time. The insets show harmonic spectra for laser fields (black line) of either low (a) or high (b) intensity. The ionization time window Δt_i resulting in HHG is marked on the time axis, where the colors indicate the harmonic frequency originating from the particular ionization time. Δt_i remains unchanged under the increase of intensity but the bandwidth of the contained harmonics increases from (a) to (b), consequently, decreasing the ionization propability per harmonic frequency expressed by an increase of the chirping factor.

We proceed by analyzing the scaling of $\dot{N}_n$ with increasing laser intensity at a harmonic energy near the respective cutoff provided that $w_i(t_i)$ is kept constant by an appropriate choice of I_p. The recombination amplitude decreases with increased electron energy favoring scattering rather than recombination. Its scaling depends on the shape of the ionic potential: $|\langle 0|V_H|\mathbf{p}\rangle_C|^2 \sim I_p^{5/2}/\omega_H^4$ for a hydrogen-like ion and $|\langle 0|V_H|\mathbf{p}\rangle_Z|^2 \sim \sqrt{I_p}/\omega_H^2$ for a zero-range potential with $I_p \ll \omega_H$ and $p^2 \sim \omega_H$. Regarding the last term of Eq. (4.49), which is derived from the functional determinant and is attributed to the wave-packet nature of the electron, we follow [111] to find $v_\perp = \sqrt{E}/I_p^{1/4} \sim (\omega_H/I_p)^{1/4}$ and illustrate the chirping factor in Fig. 4.9. It describes that the bandwidth of the harmonics emitted from a fixed ionization time window rises with increasing laser intensity (i.e. the ionization probability per harmonic decreases because the overall number of harmonics increases) and can be estimated as $\partial\omega_H/\partial t_i \sim \omega_H/\Delta t_i$. Thus, the photon emission rate in a constant bandwidth for a zero-range potential scales as $\dot{N}_n \sim I_p/\omega_H^{3.5}$. A rough estimate for the scaling of I_p at a constant ionization rate can be derived fixing the common tunneling exponent yielding $I_p \sim E^{2/3} \sim \omega_H^{1/3}$ and, consequently, $\dot{N}_n \sim 1/\omega_H^{3.17}$. The decrease for a hydrogen-like potential is even more dramatic. Therefore, the HHG photon yield decreases with rising photon energy due to the decreased probabilities of ionization per harmonic and the reduced recombination cross section. Our analysis points out a possible future direction for optimization of HHG by means of increasing the ionization time window at a given harmonic bandwidth, enhancing the recombination probability or by increasing the gas volume.

4.3 Relativistic phase-matched x-ray assisted HHG

In this section, we investigate the macroscopic emission of a different setup that was suggested in [82,91] on a single-atom level. Relativistic HHG from an exclusively conventional plane-wave laser field is not possible because of the continuous drift of the electronic wave packet in the propagation direction (see also Section 2.1.1 and Fig. 2.3). If the electron were ionized with an initial momentum opposite to the laser propagation, the subsequent relativistic drift motion could be compensated and the electron could recollide. Practically, the initial momentum could be delivered to the electron if it were single-photon ionized rather than tunnel ionized, which could be achieved by employing x-ray assistance as proposed in Ref. [82, 91]. Once in the continuum, the electron is driven by the IR laser only. Such a compensated trajectory is illustrated in Fig. 4.10. The weak x-ray field propagates perpendicular to the IR field and has a polarization along the propagation direction of the laser. The frequency of the x-ray beam ω_X is chosen such that it

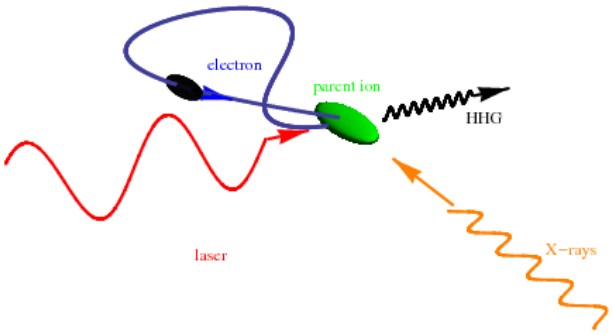

Figure 4.10: Geometry of the HHG process: The electron is ionzed by the x-ray field (orange) and delivers initial momentum to it. The laser field (red) drives the electron in the continuum. A classical trajectory is shown in blue. Recollision is possible if the initial momentum compensates for the relativistic drift.

exceeds the ionization threshold I_p of the ion and single-photon ionization can happen where additional initial kinetic energy is delivered to the electron. The initial momentum can compensate for the relativistic drift motion and rescattering can occur along with the emission of relativistic harmonics. Such a classical electron trajectory is shown in Fig. 4.10. The electron starts in the opposite direction to the laser propagation direction. Subsequently, the Lorentz force acts in the counterdirection of the electron motion and leads to recollision in this way.

4.3.1 Single-atom HHG emission

First we concentrate on the single-atom HHG emission yield. The harmonic emission spectrum can be calculated via [82, 91] and is displayed in Fig. 4.11 (a) in red for the set of parameters denoted in the caption of the figure. The ionization potential I_p is chosen in order that tunnel ionization by the strong optical laser field does not lead to ground-state depletion. In this chapter, we exclusively employ a zero-range potential

as binding potential. We compare this spectrum with the spectrum of a conventional HHG setup where no x-ray field is present calculated either fully relativistically (black) or within the DA (gray). As the gray and red curve are of comparable order, we see that the relativistic drift is compensated. The yield is much higher than for the fully relativistically calculated curve (black) for the conventional setup where the drift is not compensated. For the chosen parameters, mainly 3 quantum paths contribute to each energy in the spectrum. The separate contribution of each quantum path to the spectrum is shown in Fig. 4.11 (b).

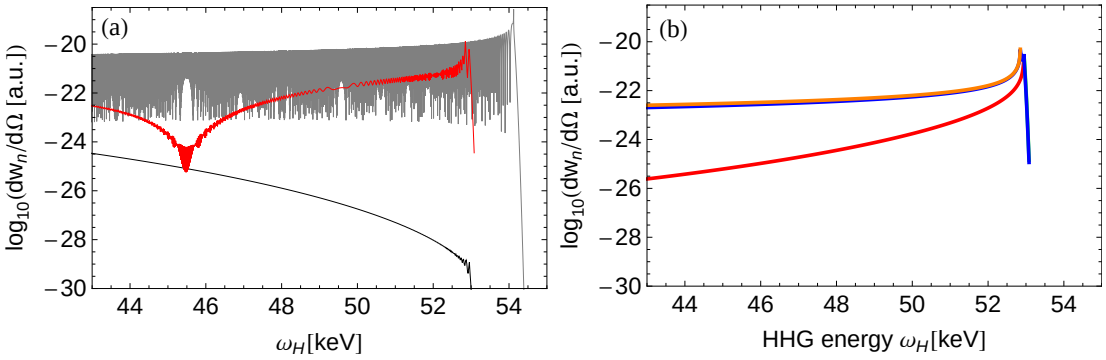

Figure 4.11: (a) Single-atom emission probability for $E_0 = 2.5\,\text{a.u.}$, $I_p = 8\,\text{a.u.}$, $\omega_X = 14\,\text{a.u.}$ and $E_X = 0.15\,\text{a.u.}$ (red) and a conventional laser field with $E_0 = 2.5\,\text{a.u..}$, $E_X = 0$ and $I_p = 4.96\,\text{a.u.}$ (black) and the same configuration in the DA. For the second configuration I_p is chosen such that the average tunnel-ionization rate is the same as the single-photon ionization rate in the case before. (b) Separate HHG yields of the three contributing quasi-classical trajectories for the discussed setup [red line in (a)]. The red contribution is suppressed because the drift for the trajectory is not completely compensated (as discussed in Sec. 4.3.1.1).

4.3.1.1 Saddle points and influence of x-ray field

The saddle-point equations have to be solved to calculate the harmonic spectrum. The saddle-points are the ionization and recollision times and the canonical momentum of the classical electron trajectory leading to the emission energy under consideration. In Fig. 4.11 (b), three such classical trajectories existed for one specific energy. In the following, we examine the influence of the x-ray photon energy ω_X on the saddle-points and discuss Fig. 4.11 (b) in detail. For illustration, we calculate the saddle-point solutions for different x-ray frequencies ω_X for the harmonic emission at 50 keV and show the ionization phase (saddle point) in Fig. 4.12 (a). For small initial energies $\omega_X - I_p$, two saddle points contribute to harmonic emission as in the usual case of HHG in a driving laser only. Both saddle points, the long and short trajectory, are complex (real part shown in the graph) and their HHG amplitude is very tiny due to the missing drift compensation (expressed by the complex value). When increasing ω_X, first the short trajectory (at ionization phase $\eta_2 \approx -1.155$) and then the long trajectory (at $\eta_2 \approx -1.345$) split up into two parts. These branches are called uphill and downhill trajectories, respectively, because their initial momentum component along the laser polarization is either positive or negative [88].

After the splitting at about $\omega_X - I_p \approx 4$ and $\omega_X - I_p \approx 8.5$, the respective ionization phase is purely real which indicates that the initial momentum is sufficient to compensate the subsequent relativistic drift. The short trajectory reaches drift compensation earlier because it spends less time in the continuum and, therefore, undergoes a smaller drift that requires compensation. We can understand the three contributions in Fig. 4.11 (b)

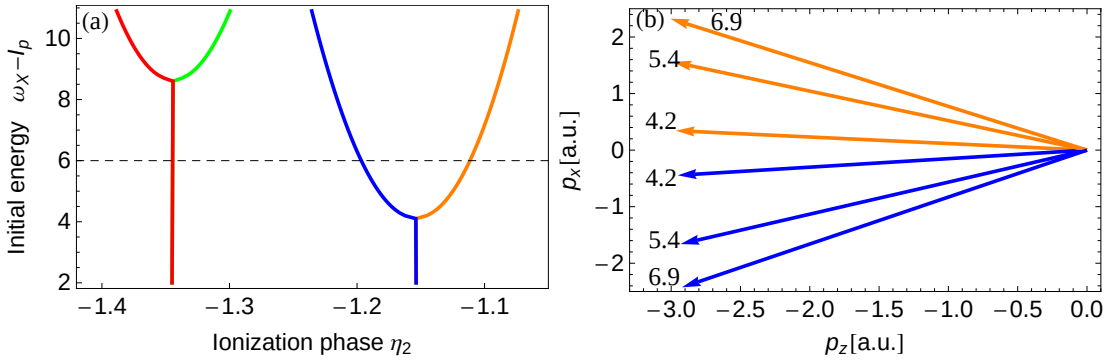

Figure 4.12: (a) We show the ionization phase saddle points of the $50\,\mathrm{keV}$ trajectory for different x-ray frequencies which is the same as ionization time in units of radian. The dashed line indicates the value chosen in Fig. 4.11. (b) displays the initial momentum direction for different initial energies $\omega_X - I_p$ [as indicated in a.u. next to the respective arrow] needed for the emission of $50\,\mathrm{keV}$. The momenta correspond to the up- and downhill short trajectories and the color indication coincides with the one in (a).

when concentrating on the dashed line in Fig. 4.12 (a). The short trajectory has two contributions (blue and orange) whereas the long trajectory has only one contribution (red). The contribution of the long trajectory is suppressed by 1-2 order of magnitude. This is because it spends more time in the continuum and the larger relativistic drift is not fully compensated. In this case, the ionization saddle point is complex. By increasing ω_X above $\omega_X - I_p \approx 8.5$, the red contribution could be enhanced leading to a larger single-atom yield. However, only one of the trajectories can be phase-matched in many cases and the enhancement of the other trajectories would not be useful. The different phase-matching for each trajectory arises because the trajectories have different excursion times τ which leads to different emission phases $\sim \mathrm{e}^{(E_{kin}+I_p)\tau}$ as described in Sec. 2.3.

When increasing ω_X over the value needed for drift compensation, no over-compensation happens and the recollision condition is still fullfilled. To understand this, it is important to keep in mind that single-photon ionization is a rather undirected process: the x-ray field ionizes the electron with a large angular distribution with a maximum around its polarization direction $\mathbf{E}_x/|\mathbf{E}_x|$. This can be seen from the ionization matrix element [131]

$$\langle \mathbf{p}|\mathbf{E}_x \cdot \mathbf{x}|0\rangle = \frac{-2\mathrm{i}\kappa^{1/2}\mathbf{E}_x \cdot \mathbf{p}}{\pi(\mathbf{p}^2+\kappa^2)^2}\,, \tag{4.50}$$

(calculated for the bound-state wave function of a zero-range potential where $\kappa = \sqrt{2I_p}$) where $\mathbf{p}$ is the initial momentum direction. In this large variety of possible starting directions for classical trajectories only two specific directions (the up- and downhill trajectories) lead to recollision with the specific HHG energy under consideration. The starting

directions are displayed for different ω_X in Fig. 4.12 (b) being solutions of the saddle-point equations. When $\omega_X - I_p \approx 4.2\,\text{a.u.}$, the threshold to achieve drift compensation for the short trajectories is just exceeded [see Fig. 4.12 (a)]. In this case, the initial momentum is directed mainly along the z-direction [arrows indicated by 4.2 in Fig. 4.12 (b)]. When ω_X is increased, only the p_x component changes; the p_z component determined by the drift compensation condition remains approximately. Because the HHG amplitude for each trajectory contains the ionization matrix element (4.50), the efficiency in each case depends on the scalar product between required ionization direction $\mathbf{p}$ and x-ray field polarization direction $\mathbf{E_x}/|\mathbf{E_x}|$ [see Eq. (4.50)]. This results in some freedom in choosing the direction of E_x. Only if $\mathbf{p}$ and E_x are close to be perpendicular would the probability of the amplitude be suppressed. In the next paragraph, we will see that it can be advantageous to choose E_x parallel to the laser polarization direction to have a collinear propagation of the laser and x-ray field. This is different to what is proposed in [82,91] and shown in Fig. 4.10. When choosing the x-ray field polarization along the x-direction, an initial kinetic energy at least somewhat larger than the minimum value at about 4.2 a.u. is necessary to achieve efficient ionization. As discussed in Fig. 4.12 (b), the angle between $\mathbf{p}$ and $\mathbf{E}_x$ becomes smaller with increasing initial kinetic energy and the ionization matrix element (4.50) for the particular trajectory larger.

4.3.2 Macroscopic HHG emission

After the discussion of the single-atom yield of the setup, we continue with a discussion on how to apply the scheme to a macroscopic gas target. The macroscopically emitted harmonic electric field is calculated in Eq. (4.10) from the Fourier-transformed single-atom current density of an atom at $\mathbf{x}_a$. The expression is rewritten for the present laser geometry. The x-ray field enters only into the general expression for the current density [see Eq. (4.22)]

$$\tilde{j_a}(\mathbf{x_a}, \omega_H, \mathbf{k}_H) = \frac{1}{c}\int \mathrm{d}^4x \int \mathrm{d}^4x' \mathrm{e}^{i\omega_H t - i\mathbf{k}_H\mathbf{r}} \phi^*(x - \mathbf{x}_a)\hat{\mathbf{j}} G(x, x') V_L(x') \phi(x' - \mathbf{x}_a) \quad (4.51)$$

in $V_L(x) = 2\,\mathbf{x}\cdot(\mathbf{E_X} + \mathbf{E_L}) \approx 2\,\mathbf{x}\cdot\mathbf{E_X}$ where E_L and E_X are the electric fields of the laser and x rays, respectively. Due to its negligible ponderomotive potential, the latter can be negelected for the continuum propagation of the electron and thus the propagator (4.24) remains unchanged. The electric field can be split up $V_L(x) = 2\,\mathbf{x}\cdot\mathbf{E}_{X0}\frac{1}{2}(\mathrm{e}^{-i(\omega_X t - \mathbf{k}_X\cdot\mathbf{x})} + \mathrm{e}^{i(\omega_X t - \mathbf{k}_X\cdot\mathbf{x})}) \approx \mathbf{x}\cdot\mathbf{E}_{X0}\mathrm{e}^{-i(\omega_X t - \mathbf{k}_X\cdot\mathbf{x})}$ and the second term is dropped because the other part leads to an unphysical situation [88] as can be deduced from the saddle-point equations. As previously, the dependence on the position of the atom $\mathbf{x_a}$ is given by the bound wave functions $\phi(\mathbf{x} - \mathbf{x}_a, t)$. To separate out phase factors that highly oscillate with $\mathbf{x}_a$, an integral transform is applied: $\tilde{\mathbf{x}} = \mathbf{x} - \mathbf{x}_a$. Thereafter, time integration is transformed to an integration over the laser phase: $\eta = \omega t - \mathbf{k}_L\cdot\mathbf{x} = \omega t - \mathbf{k}_L\cdot\mathbf{x}_a - \mathbf{k}_L\cdot\tilde{\mathbf{x}}$

Finally, we obtain an expression for the current density that can be evaluated within

the saddle-point approximation:

$$\tilde{j_a}(\mathbf{x_a}, \omega_H, \mathbf{k}_H) = \int_{-\infty}^{\infty} \mathrm{d}\eta' \int_{-\infty}^{\eta'} \mathrm{d}\eta'' \int \mathrm{d}^3\mathbf{q}\, m^j(\mathbf{q}, \eta', \eta'') \\ \times \exp\left(-i(S(\mathbf{q}, \eta', \eta'') + \omega_X/\omega\eta'' - (\omega_H/\omega)\eta')\right) \\ \times \exp\left(i((\omega_H/\omega)\mathbf{k}_L - \mathbf{k}_H + \mathbf{k}_X - (\omega_X/\omega)\mathbf{k}_L)\mathbf{x}_A\right) \tag{4.52}$$

where

$$m^j(\mathbf{p}, \eta', \eta'') = -i\frac{c^2(p_x + A(\mathbf{x}_A, \eta')/c)}{2\varepsilon_\mathbf{p}\omega^2} \\ \times \left\langle 0|\mathbf{p} + \frac{\mathbf{A}(\mathbf{x}_A, \eta')}{c} - \frac{\mathbf{k}_L}{\omega}(\varepsilon_\mathbf{p} + I_p - c^2) + (\omega_H/\omega)\mathbf{k}_L - \mathbf{k}_H \right\rangle \\ \times \left\langle \mathbf{p} + \frac{\mathbf{A}(\mathbf{x}_A, \eta'')}{c} - \frac{\mathbf{k}_L}{\omega}(\varepsilon_\mathbf{p} + I_p - c^2) + (\omega_X/\omega)\mathbf{k}_L - \mathbf{k}_X\, |\mathbf{x}\cdot\mathbf{E}_{X0}|\, 0 \right\rangle . \tag{4.53}$$

and $\mathbf{k}_L = n\omega/c\hat{\mathbf{e}_z}$ and n is the refractive index of the plasma. The propagation of the optical laser pulse is described by the wave vector $\mathbf{k}_L$ only and pulse deformation is ignored. m^j contains only the space dependence of the laser field propagation, whereas phase-mismatch due to difference in the refractive index between the different fields is contained in the last exponential function of (4.52). One is due to the phase-mismatch between the harmonics and the laser and the other one due to the phase-mismatch between the ionizing x rays and the laser. Interestingly, due to the different signs both can partially cancel out. The phase-mismatch is given by [argument in the last term of Eq. (4.52)]

$$\Delta k = |(\omega_H/\omega)\mathbf{k}_L - \mathbf{k}_H + \mathbf{k}_X - (\omega_X/\omega)\mathbf{k}_L| . \tag{4.54}$$

In [82,91] and Fig. 4.10, $\mathbf{k}_X$ and $\mathbf{k}_L$ are perpendicular which would result in a large phase-mismatch. For this reason, we choose a collinear alignment of the x-ray and laser fields in the following (see Fig. 4.13).

In the rest of the chapter, we inspect the emission from a Be^{3+} gas of density $\rho = 5\times10^{16}/\mathrm{cm}^3$ with the following parameters: laser frequency $\omega = 0.05$ a.u., x-ray frequency $\omega_X = 14$ a.u., a plasma refractive index [see Eq. (2.38)] at the laser frequency of $n_L = 1 - 5\times10^{-5}$. The phase mismatch at the harmonic emission energy of 50 keV is then $\Delta k = 6\times10^{-4}$ a.u. and a coherence length of $L_{coh} = 0.25\,\mu$m follows. The coherence length is too short to allow for considerable macroscopic HHG yield.

We employ a weak counterpropagating IR field to obtain a quasi-phase matching (QPM) scheme [148, 149]. The additional field is denoted by a brown line in Fig. 4.13. It is included into our mathematical formulation by changing the action in (4.52) to (4.35). The impact of the additional field can be observed in Fig. 4.14 (a). The real part of the emitted spectral field at the respective position is shown. In case no QPM scheme is applied (red line), the single-atom contributions oscillate on the scale of the coherence length estimated previously. An integration over all contributions results in extensive cancellation. However, when applying the additional field, the symmetry between the positive and negative contributions is broken (see the blue line) and both parts only

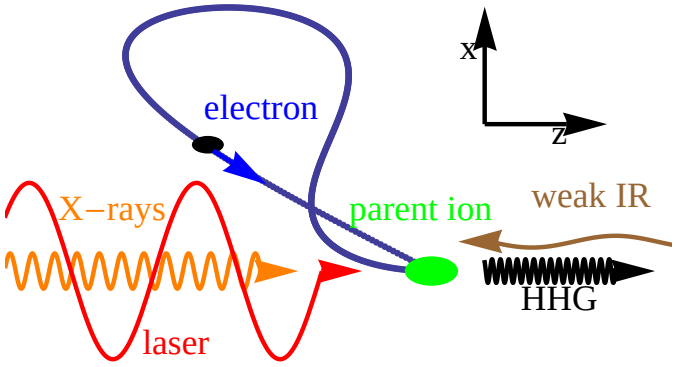

Figure 4.13: Geometry of the HHG process for a collinear alignment of the x-ray and laser field. In contrast to Fig. 4.10, the red and orange line have the same direction which improves the phase-matching behavior. Additionally, a weak IR field (brown) is added that accomplishes phase-matching.

partially cancel thus achieving quasi-phase-matching. The parameters of the additional field ($E_2 = 5 \times 10^{-5}$ a.u., $\omega_2 = 0.0418$) were chosen to optimize the spectrum at 48.6 keV as shown in Fig. 4.14 (b). A medium length of 100 μm was chosen whereas the diameter is 500 μm. The assumed laser and x-ray pulse duration is 10 cycles. The length is limited to this value because ω_2 is not given by infinite precision which results in a detuning after the length of 100 μm when assuming 0.1% precision. An integral over the spectrum yields the final result of 2×10^{-7} emitted photons per shot.

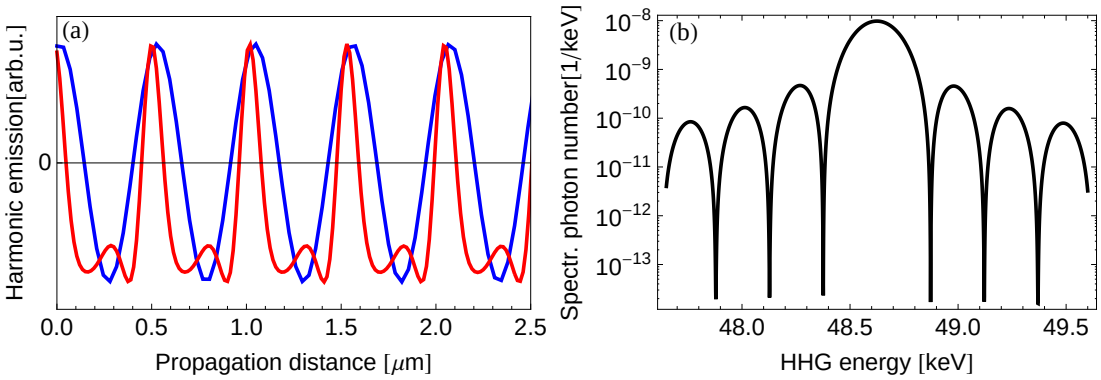

Figure 4.14: (a) Real part of spectral component of the locally emitted HHG field at 48.6 keV at different positions along the propagation direction. The blue line is for HHG without the quasi-phase-matching scheme. The red line is for the case of adding the weak counterpropagating field to achieve QPM. (b) The macroscopically emitted spectral photon number [via (4.18)] is displayed for the QPM scenario.

4.4 Discussion

Extending table-top HHG to the hard x-ray domain is an exciting prospect, especially because many research labs already use HHG as xuv source and other approaches to generate hard x rays require large scale facilities (as FELs).

The present study discussed several difficulties that need to be overcome in order to realize the idea. The relativistic drift has been extensively discussed in literature. Each proposed geometry has its own advantages and disadvantages regarding phase-matching. Generally, increasing the harmonic energy renders phase-matching more difficult for many reasons: the emission phase of the harmonics depends approximately linearly on the intensity. Small intensity variation, e.g., in a Gaussian focus, immediately results in phase difference much larger than π. On the other hand, differences in the phase velocities between the harmonics and the laser lead to a slip in space between both waves. This results in phase-mismatch as soon as the slip is comparable to the harmonic wavelength which happens earlier for shorter harmonic wavelengths. Additionally, relativistic HHG is always accompanied by an ionic gas with a large electron background because of the high laser intensities leading to an enormous plasma dispersion. For these reasons, in the best case, we obtain realizeable medium lengths of only a few tens of μm reducing the expectable macroscopic yield.

Apart from the relativistic drift and phase-matching, we identified further issues decreasing the harmonic emission in relativistic HHG connected with the single-atom yield. First, recombination of the recolliding electron becomes less likely for high momenta: scattering is favored instead. Secondly, the electronic wave function is spread over a larger energy bandwidth. If phase-matching cannot be achieved for the whole bandwidth, however, a large part of the harmonic radiation is lost. This was expressed by the chirping factor.

Regarding the harmonic yield, both setups exhibit a tiny spectrally emitted photon number that are both of the same order. The medium volume of the first setup is smaller than in the second setup but its phase-matching scheme allowed to employ a larger medium density. On the bottom line, we think that the second setup is much more promising because the required laser intensities are lower and the phase-matching scheme is more practical. One important result is that the setup proposed in [82, 91] has to be significantly modified to achieve phase-matching: the laser and the x rays have co-propagate. It is pointed out that no perpendicular alignment of both beams is necessary to achieve drift compensation. This kind of geometry has already been used in various experiments [85, 87, 89].

5 Novel HHG light via Rabi oscillations

HHG is combined with resonant x-ray excitation to obtain an efficient recombination of the continuum electron with a core hole instead of a valence hole. This way, the entire HHG spectrum is significantly upshifted in energy rendering the production of x-ray attosecond pulses possible. Additionally, the HHG spectrum bears novel signatures of the core hole of the emitting atom or molecule that can be employed to gain information about the atomic/molecular structures and ultrafast dynamics. The work has been carried out in collaboration with Christian Buth.

A new approach is proposed to transfer the state-of-the-art of attosecond science into the multi-keV regime. The technique is based on the combination of standard HHG with Rabi oscillations. Rabi flopping [190–193] is a fundamental process that occurs when a resonant or near-resonant strong light field interacts with a two level-system: the probability of finding the electron in one of the states continuously flops between the two levels, i.e., a coherent excitation and deexcitation of the upper state takes place. Such Rabi oscillation have been predicted in the x-ray regime for neon [194].

A prerequisite of this coherent process is that there is a hole in one of the states and that the excited state is not too short-lived. This situation is found in a typical HHG scenario after laser ionization of the electron: the ionized electron leaves a hole in the valence orbital and returns not before a typical time scale of 1 fs. During this time the atom can be manipulated by means of an additional strong xuv or x-ray light field, i.e., Rabi flopping of another electron can take place. The frequency of the xuv or x-ray light is chosen to be (near-)resonant to a core-valence excitation. At recollision, the returning electron sees an altered atom and can either recombine with the valence or core hole. The latter results in an upshift of the HHG photon energy by the energy difference of the two involved bound states and offers novel prospects for x-ray science and tomographic imaging of core orbitals.

The scenario is a genuine two-electron problem: a first electron evolves in accordance with the usual HHG process while the second electron Rabi flops (see Fig. 5.1). When the first electron revisits the ion, it can only recombine to the state that is not occupied by the second electron. In Section 5.1, we develop a two-electron theory based on the SFA to describe the HHG emission yield for the present process. In Section 5.2, we apply our theory on the $3d \to 4p$ transition in krypton and the $1s \to 2p$ transition in neon. The term *high-frequency light field* is used for the xuv or x-ray light field.

5.1 Analytical two-electron HHG model

To describe the atom, we first specify the three spatial one-electron states of relevance: the valence state of the closed-shell atom is $|a\rangle$ and the core state is $|c\rangle$. Within the

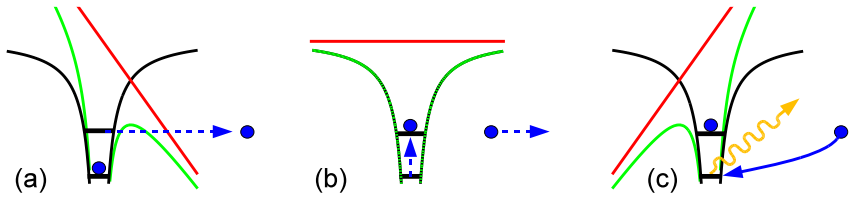

Figure 5.1: Schematic of the HHG scenario as a three-step process: (a) the valence electron is tunnel ionized; (b) the additional high-frequency light excites the core electron; (c) the continuum electron recombines with the core hole.

strong-field approximation, continuum electrons are given by free-electron states $|\mathbf{k}\rangle$ for all $\mathbf{k} \in \mathbb{R}^3$ with

$$\langle\, \mathbf{r} \,|\, \mathbf{k} \,\rangle = \frac{1}{(2\pi)^{3/2}}\, \mathrm{e}^{\mathrm{i}\,\mathbf{k}\cdot\mathbf{r}}\,. \tag{5.1}$$

The associated level energies are E_a, E_c, and $\frac{\mathbf{k}^2}{2}$, respectively. For constructing the two-electron basis, we take into account that the first electron is either in the valence state $|a\rangle$ or in the continuum $|\mathbf{k}\rangle$, whereas the second electron can be either in the core $|c\rangle$ or the valence $|a\rangle$ state. From these one-electron states the two-electron basis can be constructed which consists of three different relevant classes of states: first, the ground state of the two-electron system is given by the Hartree product $|a\rangle \otimes |c\rangle$. Second, the valence-ionized state with one electron in the continuum and one electron in the core state is $|\mathbf{k}\rangle \otimes |c\rangle$. Third, the core-ionized state with one electron in the continuum and one electron in the valence state is $|\mathbf{k}\rangle \otimes |a\rangle$.

In our model, we apply several assumptions similar to [128] and necessary to use the SFA:

- The system can be described by the three classes of states $|a\rangle \otimes |c\rangle$, $|\mathbf{k}\rangle \otimes |c\rangle$ and $|\mathbf{k}\rangle \otimes |a\rangle$.
- Depletion of the ground state is taken into account by the decay constant Γ_0 to describe direct valence ionization by the x rays and tunnel ionization by the optical laser field.
- We ignore perturbation of the ground state $|a\rangle \otimes |c\rangle$ by the laser and the x rays. Conversely, the influence of the binding potential on the continuum wave function is neglected. Moreover, we assume orthogonality between the bound states and the continuum wave function.
- The influence of the other bound electrons is ignored.
- We describe core-hole decay and direct valence ionization by the x rays and tunnel ionization by the optical field of $|\mathbf{k}\rangle \otimes |a\rangle$ and $|\mathbf{k}\rangle \otimes |c\rangle$ via the phenomenological decay constants Γ_C and Γ_A, respectively.

The time-dependent decay rates are calculated by

$$\Gamma_i(t) = \theta(t)\, \sigma_i\, J_{\mathrm{X}}(t) + \delta_{i,c}\, \gamma_c + \Gamma_{t,i} \tag{5.2}$$

with $i \in \{0, a, c\}$ where $\delta_{i,j}$ is the the Kronecker delta [138]. The first term in (5.2) covers direct ionization by the x rays. The x-ray photon flux is $J_\mathrm{X}(t)$. To determine the respective cross section σ_i, we assumed an approximately monochromatic high-frequency field. The cross section can be found in [195]. γ_c is the intrinsic decay width from Auger and radiative decay of the core-ionized state [196]. $\Gamma_{t,i}$ is the average tunnel ionization rate caused by the laser field which is calculated by means of the barrier-suppression ADK model [197].

The two-electron Hamiltonian in the laser and high-frequency field is defined as follows:

$$\hat{H} = \hat{H}_\mathrm{A} + \hat{H}_\mathrm{L} + \hat{H}_\mathrm{X} \,. \tag{5.3}$$

The individual operators $\hat{H}$ in (5.3) are constructed via tensorial products from the one-particle Hamiltonians.

Atomic electronic structure The Hamiltonian covering the atomic interaction reads

$$\begin{aligned} \hat{H}_\mathrm{A} \;=\; & \hat{h}_{\mathrm{A},1} \otimes \hat{\mathbb{1}}_2 + \hat{\mathbb{1}}_1 \otimes \hat{h}_{\mathrm{A},2} - \mathrm{i}\, |a\rangle \otimes |c\rangle \, \frac{\Gamma_0}{2} \, \langle a| \otimes \langle c| \\ & -\mathrm{i} \int_{\mathbb{R}^3} \left[|\mathbf{v}\rangle \otimes |c\rangle \, \frac{\Gamma_a}{2} \, \langle \mathbf{v}| \otimes \langle c| + |\mathbf{v}\rangle \otimes |a\rangle \, \frac{\Gamma_c}{2} \, \langle \mathbf{v}| \otimes \langle a| \right] \mathrm{d}^3 v, \end{aligned} \tag{5.4}$$

where

$$\begin{aligned} \hat{h}_{\mathrm{A},1} &= |a\rangle \, E_a \, \langle a| + \int_{\mathbb{R}^3} |\mathbf{k}\rangle \, \frac{\mathbf{k}^2}{2} \, \langle \mathbf{k}| \, \mathrm{d}^3 k \\ \hat{h}_{\mathrm{A},2} &= |a\rangle \, E_a \, \langle a| + |c\rangle \, E_c \, \langle c| \;, \end{aligned} \tag{5.5}$$

and the single-electron unity operators $\hat{\mathbb{1}}_1 = |a\rangle \langle a| + \int_{\mathbb{R}^3} |\mathbf{k}\rangle \langle \mathbf{k}| \, \mathrm{d}^3 k$ and the unity operator for the second electron $\hat{\mathbb{1}}_2 = |a\rangle \langle a| + |c\rangle \langle c|$.

Interaction with the laser field The interaction of the first electron with the laser field is taken into account in length gauge:

$$\hat{h}_\mathrm{L} = (\mathbf{e}_\mathrm{L} \cdot \mathbf{r}) \, E_\mathrm{L}(t) \;, \tag{5.6}$$

where $\mathbf{e}_\mathrm{L}$ is the polarization direction of the laser field $E_\mathrm{L}(t) = E_{0\mathrm{L}} \, \cos(\omega_\mathrm{L} \, t)$ with the laser frequency ω_L and its electric field amplitude $E_{0\mathrm{L}}$. Then, the two-electron Hamiltonian for the interaction with the laser reads [193, 198]:

$$\begin{aligned} \hat{H}_\mathrm{L} \;=\; & \int_{\mathbb{R}^3} \left[|\mathbf{k}\rangle \, \langle \mathbf{k}| \, \hat{h}_\mathrm{L} \, |a\rangle \, \langle a| + \mathrm{h.c.} \right] \mathrm{d}^3 k \otimes |c\rangle \, \langle c| \\ & + \int_{\mathbb{R}^3} \int_{\mathbb{R}^3} |\mathbf{k}\rangle \, \langle \mathbf{k}| \, \hat{h}_\mathrm{L} \, |\mathbf{k}'\rangle \, \langle \mathbf{k}'| \, \mathrm{d}^3 k \, \mathrm{d}^3 k' \otimes \hat{\mathbb{1}}_2 \;. \end{aligned} \tag{5.7}$$

The first term describes the ionization of the valence electron by the laser while the second electron is in the core state. We neglect the coupling of the second electron to the continuum because of its higher binding energy. The second term in (5.7) covers the propagation of the ionized electron in the continuum. During this time, the second electron can either be in the core or valence state.

Interaction with the high-frequency light The interaction of the second electron with the high-frequency field is described by

$$\hat{H}_{\mathrm{X}} = \int\limits_{\mathbb{R}^3} |\,\mathbf{k}\rangle\,\langle\mathbf{k}\,|\;\mathrm{d}^3k \otimes \hat{h}_{\mathrm{X}}\;, \tag{5.8}$$

where

$$\hat{h}_{\mathrm{X}} = \theta(t)\,(\mathbf{e}_{\mathrm{X}}\cdot\mathbf{r})\,\frac{E_{0\mathrm{X}}(t)}{2}\left[\mathrm{e}^{\mathrm{i}\,(\omega_{\mathrm{X}}\,t+\varphi_{\mathrm{X}}(t))} + \mathrm{e}^{-\mathrm{i}\,(\omega_{\mathrm{X}}\,t+\varphi_{\mathrm{X}}(t))}\right] \tag{5.9}$$

and ω_{X} is angular frequency of the high-frequency field with the envelope $E_{0\mathrm{X}}(t)$, time-dependent phase $\varphi_{\mathrm{X}}(t)$ and polarization $\mathbf{e}_{\mathrm{X}}$. The continuum propagation of the first electron is not influenced by the high-frequency field because the ponderomotive potential is very low due to its high frequency ω_{X}.

5.1.1 Wave function ansatz and equation of motion

In order to solve the Schrödinger equation with the Hamiltonian (5.3), we employ the following ansatz for the two-electron wave packet

$$\begin{aligned} |\,\Psi,t\rangle \;&=\; a(t)\,\mathrm{e}^{-\frac{\mathrm{i}}{2}\,(E_a+E_c-\omega_{\mathrm{X}})\,t+\mathrm{i}\,I_{\mathrm{P}}\,t}\,|\,a\rangle\otimes|\,c\rangle \\ &\quad+\int\limits_{\mathbb{R}^3}\Big[b_a(\mathbf{k},t)\,\mathrm{e}^{-\frac{\mathrm{i}}{2}\,(E_a+E_c-\omega_{\mathrm{X}})\,t+\mathrm{i}\,I_{\mathrm{P}}\,t}\,|\,\mathbf{k}\rangle\otimes|\,c\rangle \\ &\quad+b_c(\mathbf{k},t)\,\mathrm{e}^{-\frac{\mathrm{i}}{2}\,(E_a+E_c+\omega_{\mathrm{X}})\,t+\mathrm{i}\,I_{\mathrm{P}}\,t}\,|\,\mathbf{k}\rangle\otimes|\,a\rangle\Big]\;\mathrm{d}^3k\;, \end{aligned} \tag{5.10}$$

where we introduced a global phase factor based on $I_{\mathrm{P}} = -\frac{1}{2}(E_a+E_c+\omega_X) = -E_a+\frac{\delta}{2}$. $\delta = E_a - E_c - \omega_{\mathrm{X}}$ is the detuning between the high-frequency photon energy from the level spacing between the two atomic states. The indices of the amplitudes $b_a(\mathbf{k},t)$ and $b_c(\mathbf{k},t)$ indicate which orbital contains the hole. Putting the ansatz into the Schrödinger equation and projecting it onto $\langle a|\otimes\langle c|$, $\langle\mathbf{k}|\otimes\langle c|$ and $\langle\mathbf{k}|\otimes\langle a|$ yields the following three equations of motion

$$\frac{\mathrm{d}}{\mathrm{d}t}\,a(t) = -\frac{\Gamma_0(t)}{2}\,a(t) - \mathrm{i}\int\limits_{\mathbb{R}^3} b_a(\mathbf{k},t)\;\langle a|\,\hat{h}_{\mathrm{L}}\,|\mathbf{k}\rangle\;\mathrm{d}^3k \tag{5.11}$$

$$\begin{aligned} \frac{\partial}{\partial t}\,\mathbf{b}(\mathbf{k},t) \;&=\; -\frac{\mathrm{i}}{2}\left(\boldsymbol{R}(t) + (\mathbf{k}^2+2\,I_{\mathrm{P}})\,\mathbb{1}\right)\mathbf{b}(\mathbf{k},t) \\ &\quad+E_{\mathrm{L}}(t)\,\frac{\partial}{\partial k_z}\,\mathbf{b}(\mathbf{k},t) - \mathrm{i}\,a(t)\,E_{\mathrm{L}}(t)\,\wp_{\mathrm{L},\mathbf{k}\,a}\begin{pmatrix}1\\0\end{pmatrix}, \end{aligned} \tag{5.12}$$

with $\mathbf{b}(\mathbf{k},t) \equiv \binom{b_a(\mathbf{k},t)}{b_c(\mathbf{k},t)}$. The instantaneous Rabi matrix reads

$$\begin{aligned} \boldsymbol{R}(t) \;&=\; \begin{pmatrix} -\delta - \mathrm{i}\,\Gamma_a(t) & R_{0\mathrm{X}}(t) \\ R_{0\mathrm{X}}(t) & \delta - \mathrm{i}\,\Gamma_c(t) - 2\,\mathrm{i}\,\dot{\varphi}_{\mathrm{X}}(t)\end{pmatrix} \\ &=\; -\mathrm{i}\,\mathbf{diag}\big(\Gamma_a(t), \Gamma_c(t) - 2\,\mathrm{i}\,\dot{\varphi}_{\mathrm{X}}(t)\big) - \delta\,\boldsymbol{\sigma}_z + R_{0\mathrm{X}}(t)\,\boldsymbol{\sigma}_x\;, \end{aligned} \tag{5.13}$$

with the Pauli matrices $\boldsymbol{\sigma}_x$ and $\boldsymbol{\sigma}_z$ [192,199]. The instantaneous Rabi frequency is $R_{0\mathrm{X}}(t) = 2\,\langle c|\,\hat{h}_{\mathrm{X,RWA}}\,|a\rangle = E_{0\mathrm{X}}(t)\,\wp_{\mathrm{X},ca}$, where $\wp_{\mathrm{X},ca}$ is the dipole moment between the two atomic states.

In the derivation of Eqs. (5.11) and (5.12), we made the rotating-wave approximation $\hat{h}_{\mathrm{X}}\,\mathrm{e}^{-\mathrm{i}\,(\omega_{\mathrm{X}}\,t+\varphi_{\mathrm{X}}(t))} \approx \hat{h}_{\mathrm{X,RWA}} = (\mathbf{e}_{\mathrm{X}}\cdot\mathbf{r})\,\dfrac{E_{0\mathrm{X}}}{2}$ [193].

The ansatz (5.10) was chosen such that $a(t)$ can be assumed to have a constant phase and the Rabi matrix (5.13) contains no oscillating terms.

5.1.2 Wave function solutions and dipole matrix elements

In the following, we solve the equations of motion [Eqs. (5.11) and (5.12)] and distinguish two scenarios: in Sec. 5.1.2.1, the scenario of a sinusoidal high-frequency field is considered. In this case, an exact analytical solution for the wave function can be found because the Rabi matrix (5.13) is time-independent. In Sec. 5.1.2.2, we consider an arbitrary x-ray pulse to model pulses generated with the SASE principle and find an approximate analytical solution. In both cases the expectation value of the atomic dipole moment is calculated which describes the harmonic emission spectrum.

5.1.2.1 Continuous x-ray scenario

In the first scenario, we assume a sinusoidal high-frequency field, i.e., $\varphi_{\mathrm{X}}(t) = 0$ and $E_{0\mathrm{X}}(t) = \mathrm{const}$ in Eq. (5.9). Then, the Rabi matrix (5.13) as well as the decay rates (5.2) become time-independent. To decouple the equations of motion (5.12) between $b_a(\mathbf{k},t)$ and $b_c(\mathbf{k},t)$, we diagonalize the Rabi matrix (5.13) with the following eigenvalues

$$\lambda_{\pm} = -\frac{\mathrm{i}}{2}\,(\Gamma_a + \Gamma_c) \pm \mu\;, \tag{5.14}$$

and the complex Rabi frequency [193]

$$\mu = \sqrt{[\delta + \frac{\mathrm{i}}{2}\,(\Gamma_a - \Gamma_c)]^2 + R_{0\mathrm{X}}^2}\,. \tag{5.15}$$

From $b_a(\mathbf{k},t)$ and $b_c(\mathbf{k},t)$ we pass over to the dressed state basis $\beta(\mathbf{k},t) \equiv \binom{\beta_+(\mathbf{k},t)}{\beta_-(\mathbf{k},t)}$ where the Rabi matrix becomes diagonal. The matrix of the eigenvectors of (5.13) $\boldsymbol{U}$ is employed for the transform: $\mathbf{b}(\mathbf{k},t) = \boldsymbol{U}\,\beta(\mathbf{k},t)$. After the diagonalization, the decoupled equation of motions (5.12) can be integrated leading to the solution

$$\begin{aligned}\beta_{\pm}(\mathbf{k},t) \;&=\; -\mathrm{i}\,w_{\pm}\int_0^t a(t')\,E_{\mathrm{L}}(t')\wp_{\mathrm{L},\mathbf{k}-\mathbf{A}_{\mathrm{L}}(t)+\mathbf{A}_{\mathrm{L}}(t')\,a} \\ &\quad\times \mathrm{e}^{-\frac{\mathrm{i}}{2}\int_{t'}^{t}(\mathbf{k}-\mathbf{A}_{\mathrm{L}}(t)+\mathbf{A}_{\mathrm{L}}(t'))^2\,\mathrm{d}t''}\,\mathrm{e}^{-\mathrm{i}\left(\frac{\lambda_{\pm}}{2}+I_{\mathrm{P}}\right)(t-t')}\,\mathrm{d}t'\;,\end{aligned} \tag{5.16}$$

with the valence ionization fraction

$$\mathbf{w} = \begin{pmatrix} w_+ \\ w_- \end{pmatrix} = \boldsymbol{U}^{-1}\begin{pmatrix} 1 \\ 0 \end{pmatrix}\,. \tag{5.17}$$

The final expression for the wave function is obtained by plugging the solution (5.16) into the wave function ansatz (5.10). Employing the wave function, the harmonic emission is calculated via the expectation value of the time-dependend dipole matrix element $\mathcal{D}(t) = \langle \Psi_0, t | \hat{D} | \Psi_\mathrm{c}, t \rangle$. The two-electron dipole operator is

$$\begin{aligned} \hat{D} \;=\; \int\limits_{\mathbb{R}^3} \big[&|a\rangle \otimes |c\rangle \langle a| \, \mathbf{e}_\mathrm{H} \cdot \mathbf{r} \, |\mathbf{k}\rangle \langle \mathbf{k}| \otimes \langle c| \\ &+ |a\rangle \otimes |c\rangle \langle c| \, \mathbf{e}_\mathrm{H} \cdot \mathbf{r} \, |\mathbf{k}\rangle \langle \mathbf{k}| \otimes \langle a| \big] \, \mathrm{d}^3k + \mathrm{h.c.} \,. \end{aligned} \tag{5.18}$$

The polarization direction vector of the emitted light e_H is parallel to the laser polarization $\hat{e}_\mathrm{L}$. First, the momentum integration ($\int \mathrm{d}^3k$) in (5.18) is performed by means of the saddle-point method [138] (as in *Lewenstein et al.* [128] or see Sec. 2.2.1.3). Thereafter, we transform the time integral [$\int \mathrm{d}t'$, see Eq. (5.16)] to the excursion time $\tau = t - t'$ and find

$$\mathcal{D}(t) = \langle \Psi_0, t | \hat{D} | \Psi_\mathrm{c}, t \rangle = \sum_{\substack{i \in \{a,c\} \\ j \in \{+,-\}}} \mathfrak{D}_{ij}(t) \,, \tag{5.19}$$

with

$$\mathfrak{D}_{ij}(t) = -\mathrm{i}\, U_{ij}\, w_j \, \mathrm{e}^{-\mathrm{i}\,\delta_{i,c}\,\omega_\mathrm{X}\,t} \, a^*(t) \int\limits_0^\infty \sqrt{\frac{(-2\pi\mathrm{i})^3}{\tau^3}} a(t-\tau)\, A_{\mathrm{st},i}(t,\tau) \, \mathrm{e}^{-\mathrm{i}\,S_{\mathrm{st},j}(t,\tau)} \, \mathrm{d}\tau \,, \tag{5.20}$$

where

$$\begin{aligned} S_{\mathrm{st},j}(t,\tau) \;=\; &\left(\tfrac{\lambda_j}{2} + I_\mathrm{P} + U_\mathrm{P}\right) \tau \\ &- 2\,\frac{U_\mathrm{P}}{\omega_\mathrm{L}^2 \tau} \left(1 - \cos(\omega_\mathrm{L}\,\tau)\right) \\ &- \frac{U_\mathrm{P}}{\omega_\mathrm{L}}\, C(\tau)\, \cos\!\big(\omega_\mathrm{L}\,(2\,t - \tau)\big) \,, \end{aligned} \tag{5.21}$$

is the stationary quasiclassical action with the ponderomotive potential of the laser $U_\mathrm{P} = \frac{E_{0\mathrm{L}}^2}{4\,\omega_\mathrm{L}}$ and we define

$$C(\tau) = \sin(\omega_\mathrm{L}\,\tau) - \frac{4}{\omega_\mathrm{L}\,\tau}\, \sin^2\!\Big(\omega_\mathrm{L}\,\frac{\tau}{2}\Big) \,. \tag{5.22}$$

The term

$$A_{\mathrm{st},i}(t,\tau) \;=\; E_\mathrm{L}(t-\tau)\, \wp^*_{\mathrm{H},\mathbf{p}_\mathrm{st}(t,\tau)+\mathbf{A}_\mathrm{L}(t)\,i} \wp_{\mathrm{L},\mathbf{p}_\mathrm{st}(t,\tau)+\mathbf{A}_\mathrm{L}(t-\tau)\,a} \tag{5.23}$$

in (5.19) contains the atomic wave functions with the transition dipole moments

$$\wp_{\mathrm{j},\mathbf{k}\,i} = \frac{1}{(2\pi)^{3/2}} \int\limits_{\mathbb{R}^3} \mathrm{e}^{-\mathrm{i}\,\mathbf{k}\cdot\mathbf{r}}\, \mathbf{e}_\mathrm{j} \cdot \mathbf{r}\, \varphi_i(\mathbf{r})\, \mathrm{d}^3r \tag{5.24}$$

and the stationary momentum originating from the saddle-point integration is

$$\mathbf{p}_\mathrm{st}(t,\tau) = -\frac{E_{0\mathrm{L}}}{\omega_\mathrm{L}\,\tau}\, \mathbf{e}_\mathrm{L} \left[\cos(\omega_\mathrm{L}\,t) - \cos\!\big(\omega_\mathrm{L}\,(t-\tau)\big)\right] \,. \tag{5.25}$$

In order to obtain an emission spectrum depending on the harmonic frequency Ω, we Fourier transform the dipole moment (5.20) with respect to t. The only t-dependent

terms are $a^*(t)$, $a(t-\tau)$ and $A_{st,i}(t,\tau)$. The latter is periodic in time and, therefore, is decomposed into Fourier components:

$$A_{\mathrm{st},i}(t,\tau) = \sum_{M=-\infty}^{\infty} \mathfrak{b}_{M,i}(\tau)\, \mathrm{e}^{-\mathrm{i}\,(2\,M+\delta_{i,a})\,\omega_\mathrm{L}\,t}\ . \tag{5.26}$$

The complete time integration can be separated into a factor called line shape function

$$h_{M,N,i}(\Omega,\tau) \;=\; \int_0^{T_P} \mathrm{d}t\, \mathrm{e}^{-\mathrm{i}\,[(2\,(M+N)+\delta_{i,a})\,\omega_\mathrm{L}+\delta_{i,c}\,\omega_\mathrm{X}-\Omega]\,t} a^*(t)\, a(t-\tau) \tag{5.27}$$

with the optical and x-ray pulse duration T_P.

Thus, we arrive at the final expression for the Fourier transformed dipole moment

$$\begin{aligned}
\tilde{\mathfrak{D}}_{ij}(\Omega) \;&=\; \int_0^{T_P} \mathfrak{D}_{ij}(t)\, \mathrm{e}^{\mathrm{i}\,\Omega\,t}\, \mathrm{d}t \\
&=\; -\mathrm{i}\, U_{ij}\, w_j \int_0^{\infty} \sqrt{\frac{(-2\pi\mathrm{i})^3}{\tau^3}}\ \mathrm{e}^{-\mathrm{i}\,F_{0,j}(\tau)} \\
&\quad\times \sum_{N=-\infty}^{\infty} \mathrm{i}^N J_N\Big(\frac{U_\mathrm{P}}{\omega_\mathrm{L}}\, C(\tau)\Big)\ \mathrm{e}^{\mathrm{i}\,N\,\omega_\mathrm{L}\,\tau} \\
&\quad\times \sum_{M=-\infty}^{\infty} \mathfrak{b}_{M-N,i}(\tau)\, h_{M,0,i}(\Omega,\tau)\, \mathrm{d}\tau\ ,
\end{aligned} \tag{5.28}$$

where

$$\begin{aligned}
F_{0,j}(\tau) \;&=\; \frac{\lambda_j}{2}\,\tau + F_0'(\tau) \\
&=\; \Big(\frac{\lambda_j}{2} + I_\mathrm{P} + U_\mathrm{P}\Big)\,\tau - 2\,\frac{U_\mathrm{P}}{\omega_\mathrm{L}^2\tau}\,\big(1-\cos(\omega_\mathrm{L}\,\tau)\big)\ .
\end{aligned} \tag{5.29}$$

For the calculation in Sec. (5.2) we will only consider terms in (5.28) with $N>0$ similar as in [128]. The other term are not physical and can influence the results for a high-depletion scenario. Next, we discuss the two factors $\mathfrak{b}_{M,i}(\tau)$ and $h_{M,N,i}(\Omega,\tau)$ introduced in (5.26) and (5.27):

$$\mathfrak{b}_{M,i}(\tau) = \frac{1}{T_\mathrm{L}} \int_0^{T_\mathrm{L}} A_{\mathrm{st},i}(t',\tau)\, \mathrm{e}^{\mathrm{i}\,(2\,M+\delta_{i,a})\,\omega_\mathrm{L}\,t'}\, \mathrm{d}t' \tag{5.30}$$

are the Fourier coefficients of the Fourier series (5.26) and $T_L = \frac{2\pi}{\omega_L}$ the laser period. For symmetry reasons in (5.30) certain M components vanish, which leads to the selection of odd and even harmonics. To understand this, we have to compare the two half cycles in the integration period. On the one hand, we have a ungerade symmetry in time of the laser field and the free electron trajectories: $\mathbf{A}_L(t+T_L/2) = -\mathbf{A}_L(t)$ and, therefore, $\mathbf{p}_{st}(t+T_L/2,\tau) = -\mathbf{p}_{st}(t,\tau)$. On the other hand, the central symmetry of the atomic potential

implies that the atomic orbitals are parity eigenstates: $\wp_{\mathrm{j},-\mathbf{k}\,i} = \mp\wp_{\mathrm{j},\mathbf{k}\,i}$. Moreover, the states $\langle a|$ and $\langle c|$ have opposite parity. Thus, we have

$$A_{st,a}(t + T_L/2, \tau) = -A_{st,a}(t, \tau), \tag{5.31}$$

and

$$A_{st,c}(t + T_L/2, \tau) = A_{st,c}(t, \tau)\,. \tag{5.32}$$

Combining (5.31) and (5.32) with (5.30), we find that in the case of valence hole recombination even harmonics vanish and in the case of core hole recombination odd harmonics vanish.

Now we concentrate on the line shape function (5.27) of the harmonic peaks. To find an expression for $a(t)$, we have to solve (5.11). As in [128], the second term on the right-hand side in (5.11) is omitted. The term describes population transfer from and into the ground state wave function by the laser. The latter is negligible and ionization is phenomenologically covered by Γ_0. Therefore, we find $a(t) = \theta(-t) + \mathrm{e}^{-\frac{\Gamma_0}{2}\,t}\,\theta(t)$ and get for the line shape (5.27):

$$h_{M,N,i}(\Omega, \tau) = \frac{\mathrm{e}^{\frac{\Gamma_0}{2}\,\tau}(1-\mathrm{e}^{-(\Gamma_0+\mathrm{i}(\tilde{\Omega}_{M,N,i}-\Omega))T_P})}{\Gamma_0+\mathrm{i}\,[(2\,(M+N)+\delta_{i,a})\,\omega_\mathrm{L}+\delta_{i,c}\,\omega_\mathrm{X}-\Omega]}\,, \tag{5.33}$$

with $\tilde{\Omega}_{M,N,i} = (2\,(M+N)+\delta_{i,a})\,\omega_\mathrm{L} + \delta_{i,c}\,\omega_\mathrm{X}$. Ignoring the enumerator, the function peaks at odd harmonics for valence recombination and at even harmonics plus ω_X for core recombination. The widths of the peaks is determined by Γ_0. Note that in the limit $T_P \to \infty$ and $\Gamma_0 \to 0$, the function is proportional to $T_P\delta((2\,(M+N)+\delta_{i,a})\,\omega_\mathrm{L}+\delta_{i,c}\,\omega_\mathrm{X}-\Omega)$. The photon emission probability is

$$\frac{d^2 P_\mathrm{H}(\Omega)}{d\Omega d\Omega_s} = 4\,\pi\,\Omega\,\varrho(\Omega)\,|\tilde{\mathcal{D}}(\Omega)|^2 \tag{5.34}$$

with $\tilde{\mathcal{D}}(\Omega) = \sum_{\substack{i\in\{a,c\}\\ j\in\{+,-\}}} \tilde{\mathfrak{D}}_{ij}(\Omega)$ and the solid emission angle Ω_S.

5.1.2.2 Scenario of an arbitrary x-ray pulse

In the second scenario, we discuss the case of an x-ray pulse as occurring under real experimental conditions in free-electron lasers generated with the SASE principle. In this case, the Rabi matrix (5.13) is time-dependent and the equations of motion for the vector $\mathbf{b}(\mathbf{k}, t)$ (5.12) cannot be decoupled in an exact manner anymore, i.e., changing to a dressed state picture as in section 5.1.2.1 is not possible. Instead, we use an iterative approach. We first transform Eq. (5.12) by

$$\begin{aligned} b_a(\mathbf{k}, t) &= b'_a(\mathbf{k}, t)\,\mathrm{e}^{\frac{\mathrm{i}}{2}\,\delta\,t-\frac{P_a(t)}{2}} \\ b_c(\mathbf{k}, t) &= b'_c(\mathbf{k}, t)\,\mathrm{e}^{-\frac{\mathrm{i}}{2}\,\delta\,t-\frac{P_c(t)}{2}+\mathrm{i}\,\varphi_\mathrm{X}(t)}\,, \end{aligned} \tag{5.35}$$

to remove the diagonal elements of $\boldsymbol{R}(t)$ as they cover the main time-dependence. This leads to

$$\begin{aligned}\frac{\partial}{\partial t}\,\mathbf{b}'(\mathbf{k},t) &= \Big(-\frac{\mathrm{i}}{2}\,R_{0\mathrm{X}}(t)\,\boldsymbol{\Sigma}_x(t) - \mathrm{i}\left(\frac{\mathbf{k}^2}{2}+I_\mathrm{P}\right)\mathbb{1}\Big)\,\mathbf{b}'(\mathbf{k},t)\\ &\quad + E_\mathrm{L}(t)\,\frac{\partial}{\partial k_z}\,\mathbf{b}'(\mathbf{k},t)\\ &\quad - \mathrm{i}\,a'(t)\,E_\mathrm{L}(t)\,\wp_{\mathrm{L},\mathbf{k}\,a}\begin{pmatrix}\mathrm{e}^{-\frac{\mathrm{i}}{2}\,\delta\,t+\frac{P_a(t)}{2}}\\ 0\end{pmatrix}.\end{aligned} \tag{5.36}$$

The matrix

$$\boldsymbol{\Sigma}_x(t) = \begin{pmatrix}0 & \mathrm{e}^{\Delta(t)}\\ \mathrm{e}^{-\Delta(t)} & 0\end{pmatrix} \tag{5.37}$$

with the phase-amplitude difference

$$\Delta(t) \equiv -\mathrm{i}\,\delta\,t + \mathrm{i}\,\varphi_\mathrm{X}(t) + \frac{1}{2}\left(P_a(t) - P_c(t)\right) \tag{5.38}$$

contains problematic off-diagonal elements. Next, the equations of motion (5.36) are transformed according to $\mathbf{b}'(\mathbf{k},t) = \boldsymbol{U}'\,\beta'(\mathbf{k},t)$ with the time-dependent eigenvector matrix

$$\boldsymbol{U}' = \begin{pmatrix}\mathrm{e}^{\Delta(t)} & -\mathrm{e}^{\Delta(t)}\\ 1 & 1\end{pmatrix}, \tag{5.39}$$

yielding the transformed equations of motions

$$\begin{aligned}\frac{\partial}{\partial t}\,\beta'(\mathbf{k},t) &= \Big(\dot{\boldsymbol{U}}'^{\,-1}(t)\,\boldsymbol{U}'(t) - \frac{\mathrm{i}}{2}\,R_{0\mathrm{X}}(t)\,\boldsymbol{\Lambda}' - \mathrm{i}\left(\frac{\mathbf{k}^2}{2}+I_\mathrm{P}\right)\mathbb{1}\Big)\,\beta'(\mathbf{k},t)\\ &\quad + E_\mathrm{L}(t)\,\frac{\partial}{\partial k_z}\,\beta'(\mathbf{k},t) - \mathrm{i}\,a'(t)\,E_\mathrm{L}(t)\,\wp_{\mathrm{L},\mathbf{k}\,a}\,\mathbf{w}'(t)\end{aligned} \tag{5.40}$$

with

$$\beta(\mathbf{k},t) \equiv \begin{pmatrix}\beta_+(\mathbf{k},t)\\ \beta_-(\mathbf{k},t)\end{pmatrix} = \boldsymbol{U}'^{-1}(t)\,\mathbf{b}'(\mathbf{k},t)\,, \tag{5.41}$$

$$\boldsymbol{\Lambda}' \equiv \mathbf{diag}(\lambda'_+,\lambda'_-) = \boldsymbol{\sigma}_z\,, \tag{5.42}$$

the valence ionization fraction

$$\begin{aligned}\mathbf{w}'(t) &\equiv \begin{pmatrix}w'_+(t)\\ w'_-(t)\end{pmatrix}\\ &= \boldsymbol{U}'^{-1}(t)\begin{pmatrix}\mathrm{e}^{-\frac{\mathrm{i}}{2}\,\delta\,t+\frac{P_a(t)}{2}}\\ 0\end{pmatrix}\\ &= \frac{1}{2}\,\mathrm{e}^{\frac{\mathrm{i}}{2}\,\delta\,t-\mathrm{i}\,\varphi_\mathrm{X}(t)+\frac{P_c(t)}{2}}\begin{pmatrix}1\\ -1\end{pmatrix}.\end{aligned} \tag{5.43}$$

Due to the time dependence of the Rabi matrix, the following non-diagonal transformation rest is left in the equation of motion (5.40):

$$\dot{\boldsymbol{U}}'^{\,-1}(t)\,\boldsymbol{U}'(t) = \frac{\dot{\Delta}(t)}{2}\,(-\mathbb{1}+\boldsymbol{\sigma}_x)\,. \tag{5.44}$$

5.1.2.3 Iterative solution

In order to solve the transformed equation of motion (5.40), we employ the iterative ansatz

$$\beta(\mathbf{k},t) \approx \beta^{(0)}(\mathbf{k},t) + \beta^{(1)}(\mathbf{k},t) \;, \tag{5.45}$$

with respect to the off-diagonal elements in $\dot{\boldsymbol{U}}'^{\,-1}(t)\;\boldsymbol{U}'(t)$ [Eq. (5.44)] valid if $\dot{\Delta}(t) \ll R_{0x}(t)$.

Zeroth order We find $\beta^{(0)}(\mathbf{k},t)$ from Eq. (5.40) by negelecting the off-diagonal elements in $\dot{\boldsymbol{U}}'^{\,-1}(t)\;\boldsymbol{U}'(t)$:

$$\begin{aligned} \beta'^{(0)}_{\pm}(\mathbf{k},t) \;&=\; -\mathrm{i}\int_0^t a'^{\,(0)}(t')\,E_{\mathrm{L}}(t')\,\wp_{\mathrm{L},\mathbf{k}-\mathbf{A}_{\mathrm{L}}(t)+\mathbf{A}_{\mathrm{L}}(t')\,a} \\ &\qquad \times \mathrm{e}^{-\mathrm{i}\,S'_{\pm}(\mathbf{k},t,t')}\;w'_{\pm}(t')\;\mathrm{d}t' \;. \end{aligned} \tag{5.46}$$

Here, the quasiclassical action is

$$\begin{aligned} S'_j(\mathbf{k},t,t') \;&=\; \frac{1}{2}\int_{t'}^{t}\big(\mathbf{k}-\mathbf{A}_{\mathrm{L}}(t)+\mathbf{A}_{\mathrm{L}}(t'')\big)^2\,\mathrm{d}t'' + I_{\mathrm{P}}\,(t-t') \\ &\quad + \frac{\lambda'_j}{2}\,\big(\Theta(t)-\Theta(t')\big) - \frac{\mathrm{i}}{2}\,\big(\Delta(t)-\Delta(t')\big) \end{aligned} \tag{5.47}$$

and the pulse area [193] of the x rays is

$$\Theta(t) = \theta(t)\int_0^t R'_{0\mathrm{X}}(t')\,\mathrm{d}t' \;. \tag{5.48}$$

For the dipole matrix elements, we find

$$\begin{aligned} \tilde{\mathfrak{D}}'^{\,(0)}_{ij}(\Omega) \;&=\; -\mathrm{i}\int_0^\infty \sqrt{\frac{(-2\pi\mathrm{i})^3}{\tau^3}}\;\mathrm{e}^{-\mathrm{i}\,F'_0(\tau)} \\ &\quad \times \sum_{N=-\infty}^{\infty} \mathrm{i}^N J_N\Big(\frac{U_{\mathrm{P}}}{\omega_{\mathrm{L}}}\,C(\tau)\Big)\;\mathrm{e}^{\mathrm{i}\,N\,\omega_{\mathrm{L}}\,\tau} \\ &\quad \times \sum_{M=-\infty}^{\infty} \mathfrak{b}_{M-N,i}(\tau)\,h'_{M,0,i,j}(\Omega,\tau)\,\mathrm{d}\tau \;, \end{aligned} \tag{5.49}$$

with $F'_0(t)$ defined in (5.29), $C(\tau)$ in (5.22),

$$\phi_i(t) = (-1)^{\delta_{i,c}}\,\frac{\delta}{2}\,t - \delta_{i,c}\,\omega_{\mathrm{X}}\,t + \mathrm{i}\,\frac{P_i(t)}{2} \;, \tag{5.50}$$

and

$$h'_{M,N,i,j}(\Omega,\tau) = \frac{(-1)^{\delta_{i,c}\,\delta_{j,-}}}{2}\int_0^{T_\mathrm{P}} \mathrm{e}^{-\frac{P_0(t)+P_0(t-\tau)}{2}}\mathrm{e}^{-\mathrm{i}\,[(2\,(M+N)+\delta_{i,a})\,\omega_\mathrm{L}+\delta_{i,c}\,\omega_\mathrm{X}-\Omega]\,t} \times \mathrm{e}^{\frac{\mathrm{i}}{2}\,(\varphi_\mathrm{X}(t)-\varphi_\mathrm{X}(t-\tau))}\,\mathrm{e}^{-\mathrm{i}\,\delta_{i,c}\,\varphi_\mathrm{X}(t)}\mathrm{e}^{\frac{-P_a(t)-P_c(t)+P_a(t-\tau)+P_c(t-\tau)}{4}} \times \mathrm{e}^{-\frac{\mathrm{i}}{2}\,\lambda'_j\,(\Theta(t)-\Theta(t-\tau))}\,\mathrm{d}t\,.$$

For the calculation in Sec. (5.2) we will only consider terms in (5.49) with $N > 0$ similar as in [128]. The other term are not physical and can influence the results for a high-depletion scenario.

First order In the next step, we calculate $\beta^{(1)}(\mathbf{k},t)$ by separating the non-diagonal part of (5.40) and setting $\beta(\mathbf{k},t) = \beta^{(0)}(\mathbf{k},t)$ there and obtain:

$$\beta^{(1)}(\mathbf{k},t) = \int_0^t \frac{1}{2}\,\dot{\Delta}(t')\,\mathrm{e}^{-\mathrm{i}\,S'_\pm(\mathbf{k},t,t')}\,\boldsymbol{\sigma}_x\,\beta^{(0)}(\mathbf{k},t')\,\mathrm{d}t'\,. \tag{5.51}$$

And the first order solution is given by

$$\tilde{\mathfrak{D}}'^{(1)}_{ij}(\Omega) = -\mathrm{i}\,\frac{(-1)^{\delta_{j,-}}}{2}\int_0^{T_\mathrm{P}} \mathrm{e}^{-\frac{P_0(t)}{2}-\frac{P_a(t)+P_c(t)}{4}}\mathrm{e}^{\frac{\mathrm{i}}{2}\,\varphi_\mathrm{X}(t)}\,\mathrm{e}^{-\frac{\mathrm{i}}{2}\,\lambda_j\,\Theta(t)} \times \sum_{M,N=-\infty}^{\infty} \mathrm{e}^{-\mathrm{i}\,[(2\,(M+N)+\delta_{i,a})\,\omega_\mathrm{L}+\delta_{i,c}\,\omega_\mathrm{X}-\Omega]\,t} \times \mathcal{K}_{M,N,i,j}(t)\,\mathrm{d}t\,, \tag{5.52}$$

with the integrals

$$\mathcal{K}_{M,N,i,j}(t) = \int_0^t \frac{1}{2}\,\Big[-\mathrm{i}\,\delta + \mathrm{i}\,\dot{\varphi}_\mathrm{X}(t-\tau') + \frac{\dot{P}_a(t-\tau')-\dot{P}_c(t-\tau')}{2}\Big]\,\mathrm{e}^{\mathrm{i}\,\lambda_j\,\Theta(t-\tau')} \times \big[\mathcal{J}_{M,N,i,j}(t) - \mathcal{J}_{M,N,i,j}(\tau')\big]\,\mathrm{d}\tau'\,, \tag{5.53}$$

and

$$\mathcal{J}_{M,N,i,j}(t) = \frac{(-1)^{\delta_{j,+}}}{2}\int_0^t \sqrt{\frac{(-2\pi\mathrm{i})^3}{\tau^3}}\mathfrak{b}_{M-N,i}(\tau)\,\mathrm{e}^{-\mathrm{i}\,F'_0(\tau)}\mathrm{i}^N J_N\Big(\frac{U_\mathrm{P}}{\omega_\mathrm{L}}\,C(\tau)\Big)\,\mathrm{e}^{\mathrm{i}\,N\,\omega_\mathrm{L}\,\tau} \times \mathrm{e}^{-\frac{P_0(t-\tau)}{2}+\frac{P_a(t-\tau)+P_c(t-\tau)}{4}}\,\mathrm{e}^{-\frac{\mathrm{i}}{2}\,\varphi_\mathrm{X}(t-\tau)}\mathrm{e}^{-\frac{\mathrm{i}}{2}\,\lambda_j\,\Theta(t-\tau)}\,\mathrm{d}\tau\,. \tag{5.54}$$

5.2 Case studies for Kr and Ne

In this part, we apply the former theory to two different atoms. We consider the $3d \to 4p$ transition in krypton with a level spacing of 83.6 eV in the xuv regime. We use

parameters that are feasible at the Free Electron Laser in Hamburg (FLASH) [200]. And second, we use an x-ray field at 835 eV such as generated at LCLS [201] together with the $1s \to 2p$ transition in neon.

The chosen driving laser fields are $3 \times 10^{14}\,\mathrm{W/cm^2}$ for krypton and an intensity of $5 \times 10^{14}\,\mathrm{W/cm^2}$ for neon both at 800 nm wavelength. Neon exhibits a higher ionization potential and thus can withstand higher laser intensities. The photoionization cross sections σ_i required for the decay rates (5.2) are found in [195] and the orbital wave functions for the transition dipole moments are calculated in the Hartee-Fock-Slater approximation.

For each individual atomic system we distinguish two cases: First, we apply our exact theory of a sinusoidal x-ray pulse and, in a second step, we generate model pulses of a free electron laser [202, 203] and use our approximate theory.

The energies of the participating $3d$ and $4p$ levels in krypton are $E_c = -96.6\,\mathrm{eV}$ ($\mathrm{Kr}\,3d$) and $E_a = -14.0\,\mathrm{eV}$ ($\mathrm{Kr}\,4p$), respectively. For neon the binding energies are $E_c = -857\,\mathrm{eV}$ ($\mathrm{Ne}\,1s$) and $E_a = -21.6\,\mathrm{eV}$ ($\mathrm{Ne}\,2p$).

5.2.1 Sinusoidal high-frequency pulse

In this case, we consider two x-ray intensities of $10^{13}\,\mathrm{W/cm^2}$ and $10^{16}\,\mathrm{W/cm^2}$. The respective decay rates calculated via (5.2) are shown in Tab. 5.1. For the lower intensity the core hole decay is mainly governed by Auger decay and tunnel ionization rather than x-ray ionization. The Auger decay rate of the Kr^+ $3d$ vacancy is 88 meV [204] corresponding to a life time of 7.5 fs. The rate for the $\mathrm{Ne}\,1s$ vacancy is 270 meV being a life time of 2.4 fs.

I_{0X} [$\mathrm{W/cm^2}$]	Γ_0 [meV]	Γ_a [meV]	Γ_c [meV]
Krypton $3d \to 4p$			
10^{13}	280	1.5	88
10^{16}	450	170	300
Neon $1s \to 2p$			
10^{13}	5.7	10^{-3}	270
10^{16}	7	1.3	272

Table 5.1: Decay rates defined in (5.2) for the krypton $3d \to 4p$ and neon $1s \to 2p$ transition for cw high-frequency fields of different intensities I_{0X} at frequency 83.6 eV and 835 eV, respectively.

Before investigating the HHG process, isolated Rabi flopping of the system is examined. If we ignore all terms related to the laser field in Eq. (5.12), we obtain the well-known Rabi equations [193]. In Fig. 5.2, the probabilities of finding the electron in either state are displayed. The chosen time scale is few femtoseconds because the continuum electron revisits the ion after a typical excursion time of about 1 fs interacting with the tuned system. Therefore, we can use the figure for comparison when the entire system is investigated below. For a high-frequency field intensity of $10^{13}\,\mathrm{W/cm^2}$ we see a low excitation probability of the second electron on the order of 10^{-3} for both elements [see Fig. 5.2 (a) and (b)]. Increasing the laser intensity to $10^{16}\,\mathrm{W/cm^2}$ results in a larger Rabi frequency and in an equal propability distribution between the two states on that timescale. The

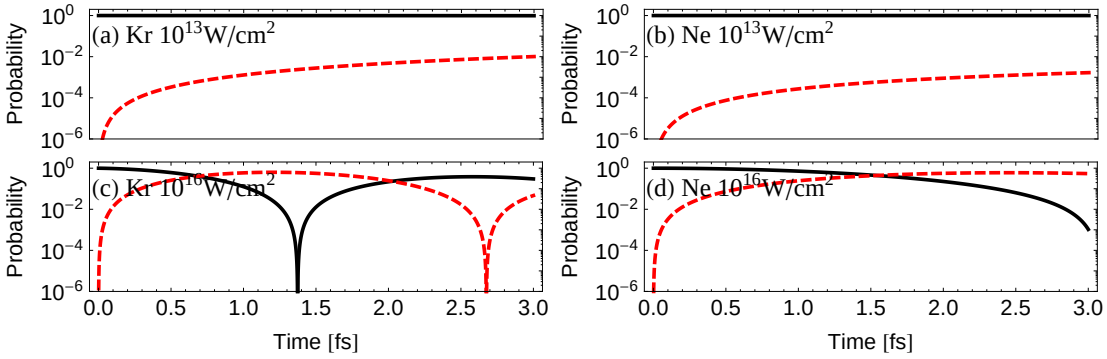

Figure 5.2: The time evolution of the probabilities to find the electron in the valence (solid black line) or core (dashed red line) states are shown for different high-frequency field intensities (as indicated in the graph) and for krypton and neon.

oscillation frequency for krypton is larger than the one for neon because its dipole matrix element between the two involved states in krypton is larger.

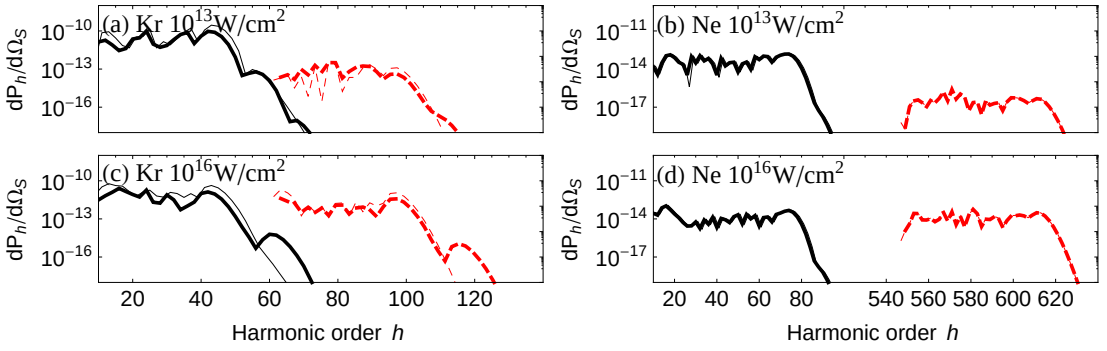

Figure 5.3: HHG photon numbers of the h^{th} harmonic for different high-frequency field intensities from krypton and neon. The black line is for the case of recombination to the valence state whereas the more energetic plateau (red dashed) occurs for core hole recombination. The lines were obtained by integrating the emission probability (5.34) around the finite harmonic peaks. The thin lines in the spectrum are obtained by neglecting ground-state depletion by direct x-ray ionization ($\Gamma_0 = 0$). The pulse duration (T_P) is three optical laser cycles and the detuning $\delta = 0$.

In Fig. 5.3 the HHG spectra for the two x-ray intensities are shown calculated via (5.34). In all cases a second plateau of significant probability appears upshifted in energy by the respective ω_X compared to the first plateau. The second high-energy plateau arises due to recombination with the core state. For the lower x-ray intensity [(a) and (b)], we observe about a suppression of about 3 orders of magnitude between the valence and core plateau in each atomic system. This is in accordance to the valence state population in Fig. 5.2 (a) and (b), which is also about 3 orders of magnitude lower than the core population. The x-ray intensity of $10^{13}\,\mathrm{W/cm^2}$ is not strong enough to excite the system in this short time with a large probability. The situation is different for an x-ray intensity of $10^{16}\,\mathrm{W/cm^2}$

shown in Fig. 5.3 (c) and (d). Here, the valence and core plateaus are of the same order in each system. The tiny difference arises because of different recombination dipole matrix elements for the valence and core states. Thus, we learn that the ratio of the two plateaus in the spectrum can be estimated by looking at the populations of both states for the ordinary case of Rabbi flopping.

The valence and core recombination plateaus do not overlap each other for the chosen laser intensity. In krypton the overlap can be created by increasing the laser intensity and in that way the lengths of both plateaus. A much higher laser intensity would be required to achieve an overlap for neon. The overlap between both plateaus can result in an interference pattern. Moreover, we see by comparing the thin and thick lines that ground-state depletion has minor impact on the HHG spectra even for the case of the strong x-ray field.

5.2.2 Arbitrary high-frequency pulse

So far, the ideal case of a sinusoidal high-frequency field was discussed. High-frequency pulses of these intensities can be generated from free electron laser facilities. The pulses obey only partial coherence and largely deviate from the ideal case of a sinusoidal field. In Section 5.1.2.2 we discussed in detail how the harmonic emission from an arbitrary high-frequency pulse can be approximated. Here, we carry out these calculations.

Model pulses are generated by the method described in Ref. [202] where we choose parameters feasible at FLASH [200] in Hamburg for krypton or at LCLS [201] in Stanford for neon. Briefly described, we choose a *discrete* Gaussian spectrum centered around the respective atomic resonance line with a bandwidth of 0.7% at FWHM (coherence time $\sim 5\,\mathrm{fs}$) for Kr and 1.6% (coherence time $\sim 0.2\,\mathrm{fs}$). Then, the phase of all values in the spectrum is randomized and the new spectrum is Fourier transformed to the time domain. Here, we multiply it by a $\cos^2$ window function which is chosen to be the average pulse envelope. The FWHM of this window function is about 3 fs and the peak intensity $10^{16}\,\mathrm{W/cm^2}$. One sample pulse for both cases is shown in Fig. 5.4 (a) and (b).

In Fig. 5.4 (c) and (d), the resulting continuous HHG spectra are shown in the zeroth-order approximation [see Sec. 5.1.2.3]. As in the case of a sinusoidal x-ray field both plateaus are nearly of the same order. Even when using other model pulses, the plateau height of HHG spectrum hardly changes. Most importantly, the effect is not destroyed by the fluctuating phase of the window function. As the inset in Fig. 5.4 (c) shows, the specific details of the spectrum are very sensitive to the high-frequency pulse. Thus, a retrieval of the high-frequency pulse from the HHG spectrum may be possible.

5.3 Applications

In summary, we have pointed out that by means of a strong high-frequency field the usual HHG spectrum can be upshifted in energy without suffering from significant losses. A new avenue is opened up to transfer the emerging field of attoscience into the x-ray domain. Since the time structure of the HHG process remains unchanged, x-ray attosecond pulses could be generated allowing for pump-probe experiments on that time scale. Indeed, light

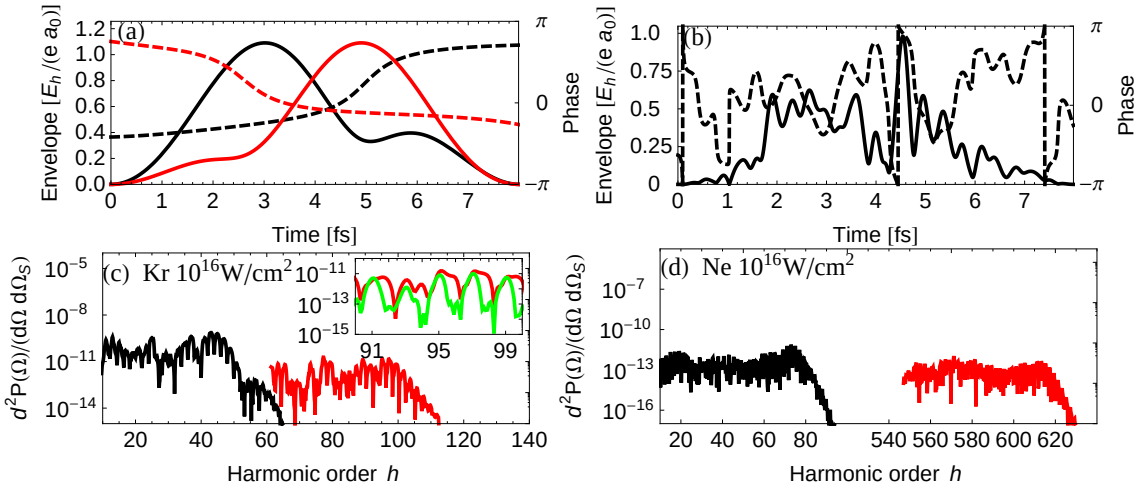

Figure 5.4: The top row displays the SASE sample pulses. The envelopes are solid lines and the phases are dashed lines. The bottom row shows the resulting HHG spectra for Kr (c) and Ne (d). In case of krypton, spectra are calculated for two different pulse samples [see (a)]. The inset shows a comparison between both spectra.

pulses at these frequency are also available from FEL but at the moment only with partial coherence and femtosecond pulse duration.

In the context of the relativistic drift problem (see Sec. 2.1.1), the present scheme is an elegant way to increase the HHG energy without suffering from drift as the laser intensity can be kept non-relativistically. Moreover, the plasma background is much lower compared with the relativistic setups which improves the phase-matching behavior. Moreover, tomographic imaging of core orbitals comes into reach due to the recombination to a core state. Additionally, the effect could also be used as optical gating method to perform frequency resolved optical gating (FROG) [205] to characterize the chaotic light pulses from FELs.

6 Wave–packet engineering in HHG

A new approach is presented as to how the intrinsic chirp in the harmonic generation process can be avoided. The well-established techniques of femtosecond pulse shaping and assistance of an x-ray pulse are employed. Using the scheme the production of zeptosecond pulses is shown to be possible. In the second part, the enhancement of the HHG yield within a chosen spectral window in the spectrum is shown to be possible by using similar techniques.

This chapter is dedicated to the manipulation of the recolliding electronic wave packet in HHG and is divided into two parts. In both parts, we employ x-ray assistance and femtosecond pulse shaping. In Section 6.1, the recolliding wave packet is spatially compressed but with a large energy spread and, accordingly, a large wave-packet chirp. The wave packet generates extremely short HHG pulses without attochirp (no optical chirp). In Section 6.2, the opposite direction is chosen where an approximately monochromatic (chirpless) wave packet recollides resulting in a monochromatic HHG emission.

6.1 HHG without attochirp

6.1.1 Introduction

HHG is the key technology for attosecond science. The shortest pulse durations currently achieved are below 100 as [40, 41, 206]. Bright HHG sources have been demonstrated with a bandwidth of hundreds of electronvolts [97] being large enough to produce pulses of only 10 as duration — as soon as the pulses can be generated without chirp in the future. Many properties of HHG radiation emitted from a gas target can be understood by studying a single atom. The three-step model [28] is the simplest model to describe the single-atom dynamics. The process starts when a strong laser field liberates the electron of an atom and subsequently drives it in the continuum. If ionization happened at the right time, the electron can be accelerated back towards the parent ion after the field has changed its sign and can recombine along with the emission of an energetic photon.

One prominent feature of HHG is that the emitted light has an intrinsic chirp, the so-called attochirp [98, 99]. The origin of the attochirp can be understood from the classical electron trajectories in the laser field: trajectories with different energies recollide at different times. Due to the widespread classical recollision times in a usual sinusoidal laser field, the emitted harmonic pulses have a longer duration than their bandwidth limit, that is the minimum pulse duration for a given spectral bandwidth reached when the spectral phase of the harmonic pulse is constant. To compress the emitted pulse, dispersive elements of either chirped multilayer x-ray mirrors [207], thin metallic films [100, 101] or gaseous media [41, 208] are employed and even the use of grating compressors is attempted [209].

However, these techniques suffer from losses, rely on the material properties and the chirp is not well-controlable in these schemes. Additionally, it is required to select radiation from the positively chirped short trajectory via phase-matching before the compensation element. Other approaches [97, 210] employ driving laser fields with longer wavelengths λ in order to take advantage of the reduced chirp $\alpha_2 \propto \frac{\partial t}{\partial \omega} \propto 1/\lambda$. α_2 decreases because the HHG cutoff energy scales as λ^2 whereas the time recollision window only scales with λ. Therefore, if the employed harmonic bandwidth $\Delta\omega$ is kept constant, a shorter harmonic pulse with duration $\Delta t = \alpha_2 \Delta\omega$ can be obtained without requiring any chirp compensation. On the other hand, when one takes advantage of the quadratically increasing harmonic bandwidth, the pulse duration of the emitted harmonics increases with λ. In [211, 212] it was shown that even without selection of certain trajectories, it is possible to partially reduce the attochirp by adding a weak second-harmonic or subharmonic field. The attochirp problem is expected to get more significant and demanding when photon energies spanning far into the soft x-ray domain are reached in the future.

In this section, we propose a way to engineer the attochirp in a determined manner by altering the harmonic generation process. In terms of the wave function, the following scenario is realized: the wave function localized in the binding potential is continuously freed resulting in a large spread in space and momentum. The electronic quantum dynamics is tuned in a way that after a certain time of propagation, the wave function spatially re-compresses at least along the propagation direction of the wave packet. It has its minimum width exactly at the time of recollision but with a large energy bandwidth gained during propagation in the continuum. We show that when the laser pulse is shaped by adding a small number of low-order harmonics and employing soft x rays for ionization, attosecond pulses with arbitrary chirp can be formed including the possibility of attochirp-free HHG and bandwidth-limited attosecond pulses.

The benefit of assisting the HHG process in a strong laser field with a weak high-frequency field has been demonstrated mainly for the purpose of enhancing the single-atom yield [85–89], improving phase matching [89] or suppressing the relativistic drift [82, 91]. On the other hand, femtosecond pulse shaping has been used to shape the HHG spectrum [94], to increase the HHG cutoff [95, 96] or for relativistic HHG [80, 81]. Here, we employ x rays to ionize the electron with non-zero velocity and combine it with femtosecond pulse shaping to control the spectral phase of the harmonic spectrum.

6.1.2 Classical analysis

The HHG process can be analyzed by taking only a few quatum orbits into account [128] that correspond to classical trajectories. Therefore, a classical analysis is able to give first insight into our idea. In this first part, we start out by considering classical trajectories in a tailored laser field [see Fig. 6.1 (a)] and find the condition when trajectories ionized at different times recollide at the same time. For the considered laser intensities, the classical trajectories have only a component along the polarization direction of the laser field, i.e. 1-dimensional trajectories are shown. We describe the principle of our method by discussing two example trajectories marked by α and β in Fig. 6.1 (b) being ionized separated by a small time span δt_i. We first focus on the point in time when trajectory β just starts. At that time, α has already been driven slightly away from the origin.

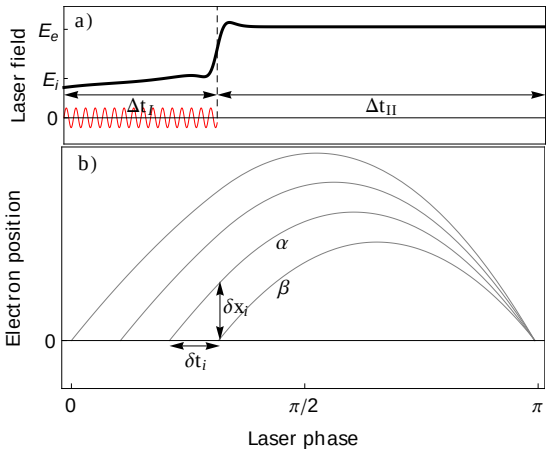

Figure 6.1: Schematic of the recollision scenario: a) A half cycle of the tailored laser field (black). The red line is the assisting x-ray pulse. b) Different classical trajectories in the field of (a) which start into the continuum at different times but revisit the ionic core at the same time.

The distance between the trajectories is $\delta x_i \approx p_i \delta t_i$ where p_i is an initial momentum e.g. mediated via one-photon-ionization (atomic units are used throughout unless stated elsewise). The momentum difference at that time is given by $\delta p_i \approx -E_i \delta t_i$ because α has already been decelerated by the laser field E_i. From now on, the momentum difference $\delta p = \delta p_i$ is constant during the whole propagation time because both experience the same acceleration. The separation of both trajectories at recollision after a time τ is therefore given by $\delta x_e \approx \delta x_i + \delta p\, \tau = (p_i - E_i \tau)\delta t_i$. $\delta x_e = 0$ reflects the condition on the initial momentum and on the electric field at ionization necessary for simultaneous recollision of the two trajectories:

$$E_i \approx p_i / \tau \tag{6.1}$$

The previous discussion applies only to the case of two single trajectories ionized with an infinitely small time separation but is sufficient for demonstration of our principle idea of simultaneous recollision for trajectories ionized from a finite time window.

In Fig. 6.1, we chose the simplest possible laser field to fulfill condition (6.1): a first plateau of strength E_i and duration Δt_I which is followed by a second higher plateau of duration Δt_{II}. In this procedure, the constant field strength E_e of the second plateau is chosen first. It determines τ for trajectories β. In the second step, the first plateau is determined having a small slope. The exact field in Δt_I is calculated by using with a polynomial expression and optimizing the coefficients such that all classical trajectories starting in Δt_I simultaneously recollide [approximately condition (6.1)].

Crucial for the previous scheme is the ionization with a non-zero velocity. The condition can be reached by using x rays of frequency ω_X which are responsible for ionization. In this case, the initial momentum is $p_i = \sqrt{2(\omega_x - I_p)}$ where I_p is the binding potential. The x rays co-propagate with the laser field and are spectrally filtered out before the harmonic radiation reaches the detector. ω_X can be chosen in a way [with the appropriate laser field according to Eq. (6.1)] to meet a resonance of a suitable absorber at ω_X. Alternatively, the x rays could propagate with a tiny angle to the propagation direction of the laser. In

Fig. 6.1, we only consider trajectories ionized within Δt_I and having a direction pointing upwards to the potential (starting in positive direction in Fig. 6.1). The initial momentum could also be directed downwards but in this case, the classical electron would not recollide and no harmonics would be emitted. A second branch of trajectories that are ignored in the figure are those trajectories emerging from the second plateau during Δt_{II}. They re-encounter the core region but all at different times and would break the desired scenario of simultaneous recollision. Therefore, ionization during the second plateau has to be suppressed which demands for the use of an x-ray pulse [sketched as red wiggeld line in Fig. 6.1 (a)] rather than a cw x-ray field. The x-ray pulse must have a non-vanishing field strength only during Δt_I being of order of 1 fs. For the proposed setup, we always employ a gas of ions rather than neutral atoms. The high ionization potential of the ions is required to entirely suppress tunnel ionization. This is because the initial momentum of a tunnel ionized electron is smaller than a x-ray ionized electron which results in a different classical trajectory with modified time of recollision. Thus, the choice of the ion species depends on the field strength of the laser field. The plasma could be generated via laser ionization with a strong pre-pulse to limit the ionization probability.

We briefly comment on the energy distribution of the recolliding trajectories. The classical trajectory marked by β has a distinct role because it experiences approximately a constant laser field. Therefore, it is symmetric to the turning point and also recollides with same momentum p_i as it started. Trajectories starting prior to β recollide with a higher energy but at the same time as β assuming the first plateau-like structure is chosen in agreement with Eq. (6.1) as it is in Fig. 6.1. Trajectory β plays the role of the trajectory with the lowest energy ω_X. The duration of the first plateau Δt_I determines the velocity difference $\Delta p \approx E_i \Delta t_I$ and the energy bandwidth $\Delta\omega_q \approx \frac{1}{2}(\Delta p + p_i)^2 + I_p - \omega_X = \frac{1}{2}\Delta p^2 + \Delta p\, p_i$.

In the optimum case shown in Fig. 6.1, all trajectories recollide simultaneously. However, under real experimental conditions, deviations of the laser and x-ray field from the optimal conditions result in a non-zero time window Δt_e of recollision. The classical model employed a discrete x-ray frequency ω_X rather than a finite bandwidth as a real pulse. The maximum allowed bandwidth can be deduced from the former model. The x rays ionize the electron with an initial velocity and arrange this way the initial displacement δx_i between two trajectories. If ω_X deviates from its optimal value by $\delta\omega_X$, the initial momentum will deviate by $\delta p_i \sim \delta\omega_X/(2p_i)$ and result in a additional displacement $\delta x_i = \delta p_i \delta t_i$ which is not compensated for. Therefore, the final wave packet size is of order $\delta p_i \Delta t_I$ resulting in a time spread of

$$\Delta t_e^{BW} = \delta p_i \Delta t_1 / p = \frac{\delta\omega_X \Delta t_I}{2 p_i p} \tag{6.2}$$

which has to be smaller than the envisaged pulse duration.

6.1.3 Strong-field approximation model

So far, purely classical dynamics was considered. In order to model the single-atom HHG yield, we use the strong-field approximation (SFA) and include the laser field within the

dipole approximation. This way, the Fourier transformed dipole matrix element is given by [82, 88]

$$\tilde{d}_q = i \int_{-\infty}^{\infty} \mathrm{d}t \int_{-\infty}^{t} dt' \int d^3\mathbf{q} \langle \Phi_0(t)|x|\mathbf{p} + \mathbf{A}(t)/c\rangle \mathbf{E}_X(t') \langle \mathbf{p} + \mathbf{A}(t')/c|\mathbf{x}|\Phi_0(t')\rangle \mathrm{e}^{-iS_q(\mathbf{p},t,t')} \tag{6.3}$$

where $\Phi_0(t)$ is the ground state wave function of the employed zero-range potential,

$$S_q(\mathbf{p}, t, t') = \int_{t'}^{t} \{[\mathbf{p} + \mathbf{A}(t'')/c]^2/2 + I_p\} \mathrm{d}t'' + \omega_X t' - q\omega t \tag{6.4}$$

the classical action and q the harmonic number. In the long wavelength regime the highly oscillating integral can be evaluated by using the saddle-point approximation. Expression (6.3) is approximated by a sum

$$\tilde{d}_q = -i \sum_s \sqrt{\frac{(-2\pi i)^5}{\det(\tilde{S}_s)}} \langle \Phi_0(t_e)|x|\mathbf{p}_s + \mathbf{A}(t_e)/c\rangle \mathbf{E}_X(t_i) \langle \mathbf{p}_s + \mathbf{A}(t_i)/c|\mathbf{x}|\Phi_0(t_i)\rangle \mathrm{e}^{-\mathrm{i}S_q(\mathbf{p}_s,t_e,t_i)} \tag{6.5}$$

over the saddle points $s = (\mathbf{p}_s, t_e, t_i)$ defined by

$$\int_{t_i}^{t_e} [\mathbf{p}_s + \mathbf{A}(t'')/c] dt'' = 0 \tag{6.6}$$

$$[\mathbf{p}_s + \mathbf{A}(t_i)/c]^2/2 = \omega_X - I_p \tag{6.7}$$

$$[\mathbf{p}_s + \mathbf{A}(t_e)/c]^2/2 + I_p = \omega_q \tag{6.8}$$

for $\tilde{S}_{(i,j)} = \partial_i \partial_j S$ where $i, j \in \{p_x, p_y, p_z, t, t'\}$ and $\omega_q = q\omega$. In case $\omega_X - Ip$ is positive, all saddle points are real for harmonics below the cutoff and, therefore, t_i and t_e are the ionization and recollision times, respectively, being also a solution of the classical equations of motion.

We analyze the condition required for (near-) bandwidth-limited emission of high harmonics. In classical electrodynamics the intensity of the emitted radiation is proportional to the dipole acceleration. From the previous derivation the spectral dipole moment $|\tilde{d}_{2j+1}|\mathrm{e}^{-i\, S_{2j+1}(\mathbf{p}_s,t_e,t_i)}$ is known. Therefore, the time-dependent intensity of the emitted light bursts is given by

$$I(t) \propto \left| \sum_j \omega_{2j+1}^2 \, |\tilde{d}_{2j+1}| \mathrm{e}^{-i\, S_{2j+1}(\mathbf{p}_s,t_e,t_i)} \mathrm{e}^{-i\omega_{2j+1}t} \right|^2 \tag{6.9}$$

where the phase $S_q(\mathbf{p}_s, t_e, t_i) \approx \alpha_0 + \alpha_1(\omega_q - \omega_c) + \frac{1}{2}\alpha_2(\omega_q - \omega_c)^2 + \ldots$ is crucial for the duration of the attosecond burst. We Taylor-expanded $S_q(\mathbf{p}_s, t_e, t_i)$ about the central harmonic frequency ω_c. As outlined in [98, 99] the linear coefficient of the expansion, the group delay, is simply given by

$$\alpha_1 = \frac{\mathrm{d}}{\mathrm{d}\omega_q} S_q(\mathbf{p}_s, t_e, t_i)\Big|_{\omega_q=\omega_c} = -t_e(\omega_q)\Big|_{\omega_q=\omega_c} \tag{6.10}$$

because the saddle-point equations lead to vanishing partial derivatives. The linear chirp, the group-delay dispersion (GDD), is given by

$$\alpha_2 = -\frac{\mathrm{d}}{\mathrm{d}\omega_q} t_e(\omega_q)\bigg|_{\omega_q=\omega_c} \approx -\frac{\Delta t_e}{\Delta\omega_q} \tag{6.11}$$

being in first approximation responsible for the duration of the harmonic pulse. Hence, the pulse can be considered to be bandwidth-limited if the quadratic term in the Taylor-expansion fulfills the following demand $|\frac{1}{2}\alpha_2(\Delta\omega_q)^2| \ll 2\pi$. This yields a criterion for the classical recollision time window Δt_e resulting from the bandwidth of the trajectories:

$$\Delta t_e \ll \frac{4\pi}{\Delta\omega_q} = \frac{4\pi}{\alpha}\Delta t_p \tag{6.12}$$

with the bandwidth-limited pulse duration $\Delta t_p = \alpha/\Delta\omega_q$ and the parameter α of order of unity determined by the spectrum. This reflects that only an approximate condition $\Delta t_e \approx 0$ is necessary for bandwidth-limited HHG emission. In the previous section, we discussed in detail how the condition of simultaneous recollision of classical trajectories $\Delta t_e \approx 0$ can be fullfilled. We will show that it is sufficient to add only a few low-order Fourier components of the fundamental laser frequency to the laser field in order to achieve an optimized field which fullfills Eq. (6.12). Moreover, Eq. (6.12) demonstrates that the chirp compensation becomes more difficult for larger bandwidth.

In our classical and quantum descriptions, we used the common assumption [85–89] of neglecting the x-ray field for the continuum propagation of the electron. This means dropping the term $S_x(\mathbf{p}, t, t') = \int_{t'}^{t} \mathrm{d}\tau\{[p_x + A(\tau)/c]\ A_x(\tau)/c + \frac{1}{2}A_x^2(\tau)/c^2\}$ in the definition of $S_q(\mathbf{p}, t, t')$. We derive an approximate condition for the maximum electric field strength of the x rays being allowed that this approximation holds and that the HHG pulse duration is not influenced by the x-ray field. When evaluating S_x at the previously determined saddle points, the additional shift of the recollision times by the x-ray field is:

$$\Delta t_{e,x} = \frac{\mathrm{d}}{\mathrm{d}\omega_q} S_x(p_s, t_i, t_e) = \frac{\partial S_x}{\partial t_i}\frac{\partial t_i}{\partial \omega_q} + \frac{\partial S_x}{\partial t_e}\frac{\partial t_e}{\partial \omega_q} + \frac{\partial S_x}{\partial p_s}\frac{\partial p_s}{\partial \omega_q} \tag{6.13a}$$

$$\approx -[p + A(t_i)/c]\ A_x(t_i)/c\frac{\partial t_i}{\partial \omega_q} \approx -\frac{E_x}{\sqrt{\omega_X}}\frac{\partial t_i}{\partial \omega_q} \tag{6.13b}$$

In Eq. (6.13a) we dropped the second term because $\frac{\partial t_e}{\partial \omega_q}$ is negligible due to the simultaneous recollision and the third term because it contains an integration over the heavily oscillating $A_x(\tau)$. Thus, the overall additional recollision time spread

$$\Delta t_{e,x} = \frac{E_x}{\sqrt{\omega_X}}\frac{\Delta t_I}{\Delta\omega_q} \ll \Delta t_e \tag{6.14}$$

has to be much smaller than the recollision time window to justify in our case the neglection of S_x.

In summary, bandwidth-limited HHG emission can be reached when the recollision time window determined by the classical dynamics in the laser field fulfills Eq. (6.12) and the x-ray field satisfies Eq. (6.2) and Eq. (6.14).

6.1.4 Generation of attosecond pulses

In the following, we describe an implementation of the scheme. We start from an optimal field shape determined in the way described above with a fundamental frequency of $\omega = 0.06$ a.u. Then, we represent the field as a Fourier series and only take the $N_F = 8$ lowest frequency components of its spectrum into account. Following this procedure, the pulses in Fig. 6.2 a) (solid black line) were found. Its relevant classical trajectories ionized by a one-photon transition are shown as solid red lines. We can observe that $t_e(\omega_q)$ is approximately constant and, therefore, we can expect bandwidth-limited harmonic emission. We compare it to the traditional case of a sinusoidal laser field with similar

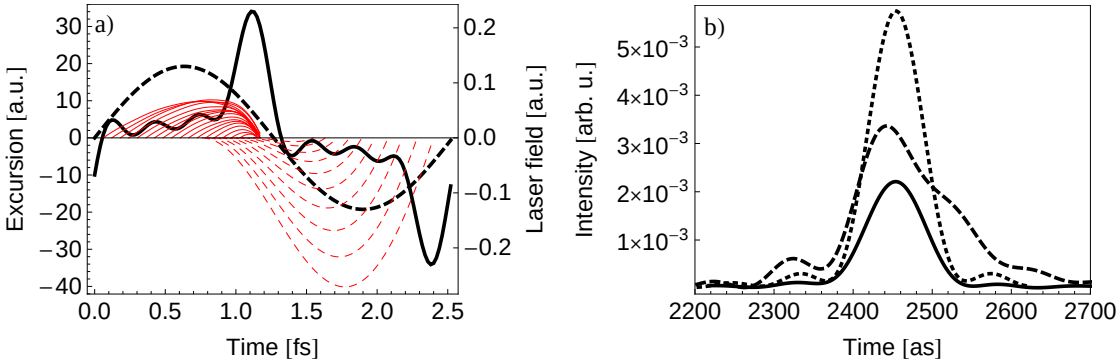

Figure 6.2: a) Classical electron trajectories (red lines) are shown for two different field configurations (thick black lines): The dashed curves are for a conventional sinusoidal laser field and a neutral Ne atom. The full lines are for a shaped laser field consisting of $N_F = 8$ harmonics that is assisted by continuous wave x-rays ($\omega_x = 60$ eV, $I_x = 9 \times 10^{12}$ W/cm^2) triggering ionization from a He$^+$ ion. b) Attosecond pulses emitted from the laser fields proposed in a). The solid line shows the intensity for the case of the proposed scheme whereas the dotted and dashed lines correspond to the attosecond pulses for a conventional field with a 40 eV bandwidth either with or without phase compensation, respectively.

parameters as in [40] (dashed lines). Evaluating the dipole moment within the SFA [Eq. (6.5)], we find the attosecond pulse generated by the fields in Fig. 6.2 (a). The results are shown in Fig. 6.2 (b). The duration of the pulse generated by our method (solid line) is 86 as at full-width half maximum (FWHM) only being slightly longer than a pulse generated by a sinusoidal field in combination with a perfect chirp compensation (78 as) (dotted line). The dashed line shows the uncompensated pulse with a duration of 130 as. In all three cases, the same frequency window between 60 eV and 110 eV was employed and the x-ray field ($\omega_x = 60$ eV, $I_x = 9 \times 10^{12}$ W/cm^2) was chosen to have the same average ionization rates as by tunnel ionization in the sinusoidal field. The two pulses from the sinusoidal pulse were obtained from neon using only the short trajectories whereas in our case He$^+$ has to be employed. The laser frequency is in all cases $\omega = 0.06$ a.u. Although the single-atom emission rate of both examples are on the same order, the photon yield of our setup will be lower because the gas density is restricted by a maximum value of 5×10^{16}/cm^{-3} as determined later. We estimate an emitted photon number per half cycle of 10^7 in the traditional case (density 10^{19}/cm^{-3})

and 10^3 in our case from a volume of 200 μm $\times$ 200 μm $\times$ 1 mm.

So far, the attosecond pulse production with durations little below 100 as was considered. The time difference of the uncompensated ($\sim$ 130 as) and compensated ($\sim$ 80 as) pulses were moderate. Now, we discuss our proposal for future experiments where the bandwidth is of order of keV and Eq. (6.12) imposes a stronger constraint, demanding for a larger phase compensation over a larger frequency spectrum. In the following, we present two examples with production of pulses below 10 as and 1 as, see Fig. 6.3.

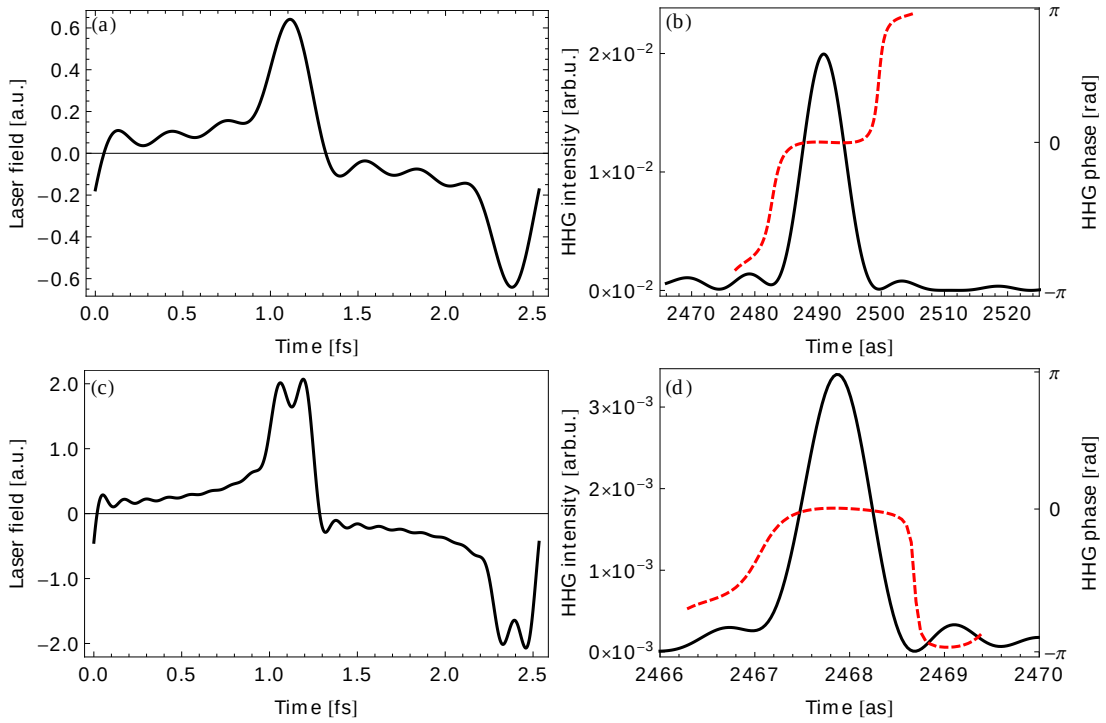

Figure 6.3: (a) shows the laser field composed of only 8 Fourier components that illuminates an Li^{2+} atom with $I_p = 4.5$ a.u.. The parameters of the assisting x-ray field are indicated in the first row of Tab. 6.1. The created 8 as pulse is shown in (b). (c) displays the laser field needed to create a pulse of 800 zs duration from Be^{3+} atoms with $I_p = 8$ a.u. and the parameters indicated in the second row of Tab. 6.1. The respective HHG pulse is shown in (d). The dashed red lines in (b) and (d) are the temporal phases of the harmonic pulses.

The laser field strength and the x-ray frequency have to be increased compared to the example before to obtain a much larger bandwidth and are indicated in Tab. 6.1. We also have to use ions with larger binding potential to suppress tunnel ionization for these even larger electric field strengths. This way, attosecond pulses with a FWHM of 8 as and 800 zs are formed. The pulses are almost bandwidth-limited as can be seen from the constant phase (red dashed line) in the main part of the pulse. When plotting the phase, the linear phase term determined by the central frequency of the pulse was subtracted from the phase. Note, that in the scenario of creating the 800 zs pulse, the laser intensity is in the weakly relativistic regime and the influence of the magnetic component of the laser field is taken into account [69].

N_F	I_L[W/cm^2]	ω_x[eV]	I_X[W/cm^2]	$\Delta\omega_q$[eV]	T_P[as]	ρ_{max}[cm^{-3}]	N_{ph}	ion
8	10^{16}	218	3.5×10^{14}	470	8	2.5×10^{16}	10^{1}	Li^{2+}
20	10^{17}	996	1.4×10^{15}	4.9×10^{3}	0.8	7×10^{14}	10^{-6}	Be^{3+}

Table 6.1: Parameters for the two examples in Fig. 6.3: N_F represents the number of Fourier components contained in the fundamental pulse, I_L its peak intensity, ω_X the x-ray frequency employed for ionization, E_X its field strength, $\Delta\omega_q$ the achieved HHG bandwidth, T_P the HHG pulse duration, ρ_{max} the estimated maximum gas density, N_{ph} an estimate of the emitted HHG photon number per half cycle emitted from a volume of 200 μm $\times$ 200 μm $\times$ 1 mm having the maximum density and the employed ion species.

The photon yield emitted from the target is very low [see Tab. 6.1] but detectable with high repetition rate driving lasers. The small signal and the seven order of magnitude reduction between the two examples in the table arise for several reasons: Firstly, in the two examples, the ionization rate is small because $\omega_X \gg I_p$ due to the required large initial momentum. Ionization cannot be enhanced by increasing the x-ray intensity because it is limited according to Eq. (6.14). One order of magnitude of reduction between the examples of Tab. 6.1 is caused by this effect. Secondly, one-photon ionization with large initial velocities results in a large spread of the ionized wave packet. In our calculations this is included via the functional determinant in (6.5). The transversal momentum uncertainty can be estimated as $\Delta p = \sqrt{2(\omega_X - I_p)}$ and thus spreading scales as $(\omega_X - I_p)$ and causes a reduction of one order of magnitude. Thirdly, the recombination cross section decreases favoring scattering rather than recombination [213] and is responsible for one order of magnitude reduction between the two cases. Finally, the gas density is limited to a small value which will be discussed shortly. Presuming phase-matching, the yield scales quadratically with the density ρ and three orders reduction between both scenarios in the table arise for this reason.

6.1.5 Macroscopic effects

Next, we discuss consequences of applying the scheme to a macroscopic gas target. Due to dispersion, the initially optimal pulse shape will be deformed during propagation. We estimate the impact of the dispersion by investigating the pulse shape after 1-dimensional propagation through a plasma of length L and refractive index $n_q = \sqrt{1 - \frac{4\pi\rho_e}{\omega_q^2}}$ where ρ_e is the electron density. In this case, each Fourier component of frequency ω_q propagates with the phase velocity $v_{ph} = c/n$ and an analytic expression can be obtained:

$$I(t) \propto \left| \sum_j \omega_{2j+1}^2 \, \tilde{d}_{2j+1} \mathrm{e}^{-i\omega_{2j+1}[t+(n_1-n_{2j+1})L/c]} \right|^2 \tag{6.15}$$

The influence of the different atomic transition lines of the medium on the dispersion is omitted because the free electron background forms the largest contribution to the dispersion. When calculating the driving pulse shape of Fig. 6.3 a) after a propagation length of $L = 1$ mm, we find a maximum ion density of $5 \times 10^{16}/\mathrm{cm}^3$ and $7 \times 10^{14}/\mathrm{cm}^3$ to maintain a duration of the harmonic burst below 10 as and 1 as, respectively. Similarly, we

can specify the precision of the phase of the different Fourier components that is required. The allowed fluctuations of the different components in terms of time delay is of the order of 25 as and 2.5 as, respectively, in agreement with the time delays caused by the plasma dispersion discussed before. The sensitivity is lower for harmonics with lower energies.

Apart from causing a deviation from the optimized pulse form, dispersion can also lead to phase mismatching. Due to the rather low gas density, we do not expect a dramatic phase mismatch. To achieve phase matching, we propose either to exploit the geometry of the laser focus or using quasi-phasematching schemes as employing a weak counterpropagating IR field [148, 149], weak static fields [150] or modulated wave guides [151–153].

So far, the recollision scheme was discussed in the spotlight of bandwidth-limited emission of attosecond pulses. The scheme can also be applied as a new type of pump-probe technique where the atom is excited or probed at a precise time by the recolliding electron. The recollision time can be controlled via shaping the driving pulse. Moreover, the spectral diversity of the simultaneously recolliding trajectories is an excellent condition for the observation of continuum-continuum harmonics [184].

6.2 Enhancement of HHG within a spectral window

In this section, we first discuss the chirping factor which arises in SFA HHG amplitudes from the 5-dimensional functional determinant. The factor has been briefly mentioned in Section 4.2.6 in connection with the small HHG yield in the relativistic regime. Now a rigorous mathematical derivation of the factor is presented.

Later, we will use this knowledge to shape the electronic wave packet and propose a scheme to enhance HHG within a small energy window by reducing the chirping factor.

6.2.1 Chirping factor

In the first part of the chapter, we employed Eq. (6.5) to model the single-atom HHG yield within the strong-field approximation (SFA) and saddle-point approximation. The expression contains the 5-dimensional functional determinant $\det(\tilde{S}_s)$ that arises when the 5-dimensional integral [see Eq. (6.3)] is carried out at once by means of the saddle-point approximation. In this case, we find a single-atom spectral emission rate proportional to

$$\frac{dw_N}{d\Omega} \propto |a_{io}|^2 \times \left|\frac{1}{\det(\tilde{S}_s)}\right| \times |a_{rec}|^2. \tag{6.16}$$

Besides the ionization amplitude a_{io} and recollision amplitude a_{rec}, the functional determinant is the third crucial factor in the SFA expression (6.16). The term occurs in many works related to HHG [81, 82, 131] but a precise physical interpretation is still missing. Only a part of it has been analyzed [111] revealing that the functional determinant takes the wave-packet spreading into account. We give a more detailed analysis of the determinant.

To this end, we first analyze the Jacobi matrix $\tilde{S}_s$ of the classical action $S_q(\mathbf{p}, t, t')$ [defined in Eq. (6.4)] from which the determinant is derived. The matrix evaluated at the

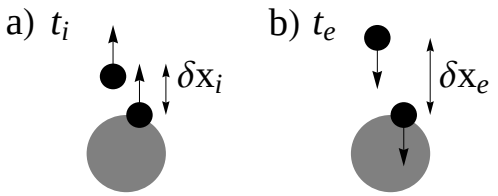

Figure 6.4: Classical electron positions (black circles) are displayed at the initial moment t_i and final moment t_e for two possible trajectories. The position of the parent ion is the gray circle. We compare two electron trajectories. In a) the first electron has already been started at an earlier time whereas the second is just starting. Their spatial separation is denoted by δx_i. In b) the same is shown at recollision

saddle-points defined by Eqs. (6.6)-(6.8) is

$$\tilde{S}_s = \begin{pmatrix} \partial_{px,px}S_q & \partial_{px,py}S_q & \partial_{px,pz}S_q & \partial_{px,t}S_q & \partial_{px,t'}S_q \\ \partial_{py,px}S_q & \partial_{py,py}S_q & \partial_{py,pz}S_q & \partial_{py,t}S_q & \partial_{py,t'}S_q \\ \partial_{pz,px}S_q & \partial_{pz,py}S_q & \partial_{pz,pz}S_q & \partial_{pz,t}S_q & \partial_{pz,t'}S_q \\ \partial_{t,px}S_q & \partial_{t,py}S_q & \partial_{t,pz}S_q & \partial_{t,t}S_q & \partial_{t,t'}S_q \\ \partial_{t',px}S_q & \partial_{t',py}S_q & \partial_{t',pz}S_q & \partial_{t',t}S_q & \partial_{t',t'}S_q \end{pmatrix} \Bigg|_{\mathbf{p}=\mathbf{p}_s, t=t_e, t'=t_i} . \tag{6.17}$$

After carrying out the derivatives and setting $p_{s,y} = p_{s,z} = 0$ according to Eq. (6.6), we find

$$\tilde{S}_s = \begin{pmatrix} \tau & 0 & 0 & p_K(t_e) & -p_K(t_i) \\ 0 & \tau & 0 & 0 & 0 \\ 0 & 0 & \tau & 0 & 0 \\ p_K(t_e) & 0 & 0 & -E(t_e)p_K(t_e) & 0 \\ -p_K(t_i) & 0 & 0 & 0 & E(t_i)p_K(t_i) \end{pmatrix} , \tag{6.18}$$

where $\tau = t_e - t_i$ is the excursion time, $p_K(t) = p_{s,x} + A(t)/c$ the kinetic momentum and $E(t) = -\partial_t A(t)/c$ the electric field strength. Note that the initial kinetic momentum is constant $p_K(t_i) = \sqrt{2(\omega_X - I_p)}$ [see also (6.7)]. Thus, we find an analytical expression for the determinant

$$\det \tilde{S} = \tau^2 p_{K,i} p_{K,e} \big(-E_i p_{K,e} + E_e(-E_i \tau + p_{K,i}) \big). \tag{6.19}$$

For short-hand notation we have introduced the subindizes i and e indicating that the respective quantity is evaluated at the ionization time t_s' or recombination time t_s, respectively, e.g., $p_K(t_s') = p_K(t_i) = p_{K,i}$.

In the following, we briefly show that the functional determinant (6.19) has also an intuitive meaning. We compare the final momentum difference $\delta p_{K,e}$ of two different classical trajectories that start from the origin separated by a time span δt_i and recollide with a delay of δt_f (see Fig. 6.4). The final momentum difference arises in this two time windows and is given by $\delta p_{K,e} = -E_i \delta t_i + E_e \delta t_e$. δt_i is a small free parameter whereas δt_e is determined by the final momentum $p_{K,e}$ and the distance $\delta x_{K,e}$ between the two particles at recombination. The final distance $\delta x_e = (-E_i \tau + p_i)\delta t_i$ (see also Sec. 6.1.2)

contains two terms that account for the spread during propagation due to the different momenta of the two particles and the initial position difference $\delta x_i = p_{K,i}\delta t_i$ between both. Taking all pieces together, we find that the derivative of the final energy with respect to the ionization time is given by

$$\frac{\partial \omega_H}{\partial t_i} \approx p_{K,e}\delta p_{K,e}/\delta t_i = -E_i p_{K,e} + E_f(-E_i\tau + p_{K,i})\,. \tag{6.20}$$

By comparing (6.20) and (6.19), we see that the functional determinant

$$\det \tilde{S} = \tau^2 p_{K,i} p_{K,e} \frac{\partial \omega_H}{\partial t_i} \tag{6.21}$$

includes the chirp of the wave packet. Moreover, the determinant strongly depends on the laser intensity because the chirping factor $\partial\omega_H/\partial t_i$ increases the cutoff and the single-atom yield per harmonic decreases this way. Even though the functional determinant is different in the relativistic regime, the general idea of the chirping factor is not based on the DA or relativistic mass shift and it survives also into the relativistic regime of HHG.

6.2.2 Reduction of the wave–packet chirp

In this section, we propose a scheme as to how the functional determinant can be controlled to enhance the single-atom HHG yield within a chosen frequency window. From Eq. (6.19) and (6.16) it follows that the single-atom yield can be increased by fullfilling two demands: (i) a small initial momentum $p_{K,i}$ and (ii) a small initial electric field E_i at ionization. The demands lead to a small function determinant (6.19) and an enhanced emission probability (6.16). Since the saddle-point approximation is based on the assumption of a non-vanishing functional determinant, our conclusion is only valid as long as the enhanced spectral window is larger than a harmonic peak. For practical reasons we choose laser parameters where our approximation is still valid. The enhancement can be understood as follows: usually, parts of the wave packet ionized at different times will recollide with different energies. However, parts of the wave function ionized in the time window where (i) and (ii) are fullfilled will recollide nearly with the same final energy that is, thus, enhanced in the emission spectrum.

For the optimization we start from a conventional sinusoidal pulse [see red line in Fig. 6.5 (a)] that is going to be shaped to meet the demands. Additionally, a weak x-ray field is required for single-photon-ionization of the electronic wave packet. This way, the ionization mechanism becomes independent of the optical pulse shape. Thus, the initial momentum of a classical trajectory is determined by $p_{K,i} = \sqrt{2(\omega_X - I_p)}$. The x-ray frequency ω_X is chosen to be only a little larger than the ionization threshold to keep the initial momentum $p_{K,i}$ small as requested from condition (i). In the next step, we modify the sinusoidal laser field in two regions: In region 1 we set the laser field close to zero. Thus, trajectories emerging from this time window fullfill also condition (ii). The hump in region 3 is such that an integral over the electric field vanishes to ensure a vanishing DC component of the pulse. The specific shape of this part (region 3) is not important because all trajectories emerging from region 1 recollide within region 2. Moreover, this step can be omitted when applying an additional constant electric laser field instead.

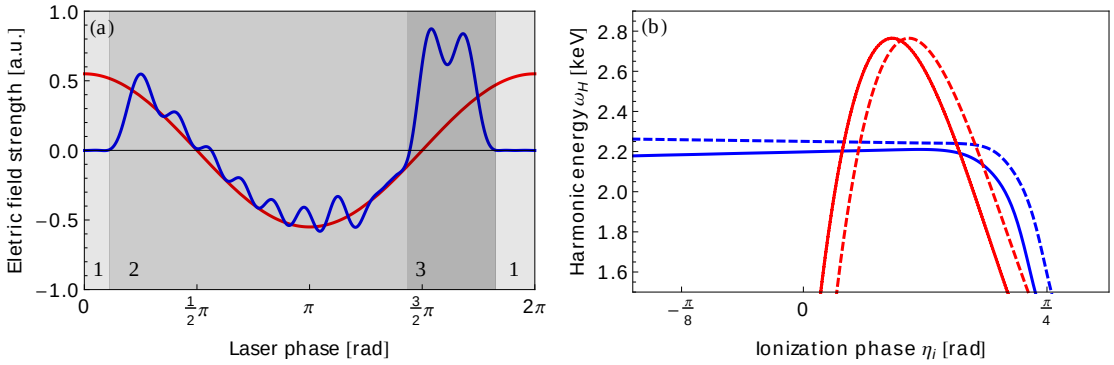

Figure 6.5: (a) displays the optimized tailored laser field (blue) and sinusoidal field (red) with the same period. Both fields are assisted by a weak x-ray field. The optimized field is determined by the procedure described in the text. (b) shows the recollision energies for electrons depending on the ionization phase calculated from the saddle points. The downhill and uphill trajectories are distinguished by a solid or dashed plot style.

The optimized laser field has small oscillations along the whole period because it is composed of a finite Fourier series with $N = 15$ components. For this reason, the field at the border between region 2 and 3 where the enhanced energies recollide is also optimized. Tiny oscillations in region 1 could cause that the chirp of the wave packet is not monotonic, i.e., the same recollision energy is met several times. Possible destructive interferences are avoided by shaping the recollision region (end of region 2). The field is shaped such that each energy is met just once. If the order of the Fourier series is increased, the unwanted oscillations become smaller and it is, therefore, possible to have a narrower and more enhanced frequency window.

The impact of our modifications on the recolliding wave packet can be inspected from Fig. 6.5 (b). The graph displays the final recollision energies versus the ionization time of the classical trajectories. The red lines are for the x-ray assisted conventional sinusoidal field with 4 contributions to each energy: long and short uphill (solid line) and long and short downhill (dashed) trajectories. The left part before the maximum energy are called long trajectories, whereas the right part corresponds to the ionization phases of the short trajectories (see Sec. 2.1). Because of the x-ray ionization the initial momentum direction can be directed with or towards the laser field and leads to the distinction between up- and downhill trajectories (as discussed in Sec. 4.3.1.1). The tailored field modifies the saddle-point equations as can be seen from the blue lines in Fig. 6.5 b). The long trajectory and the high-energy part of the short trajectories are mainly affected as their ionization time lies in region 1 of the laser field which has been modified. All trajectories ionized within that region have nearly the same final recollision energy and thus we expect a small chirping factor $\partial\omega_H/\partial t_i$. The trajectories from this ionization time window differ only due to their ionization direction (up- or downhill). Therefore, a large fraction of the ionized wave packet recollides within these two tiny energy ranges. The energy of these windows is determined by the laser field evolution in region 2 and their bandwidth is given by the chirping factor (6.20). The rising edge between region 1 and 2 has not

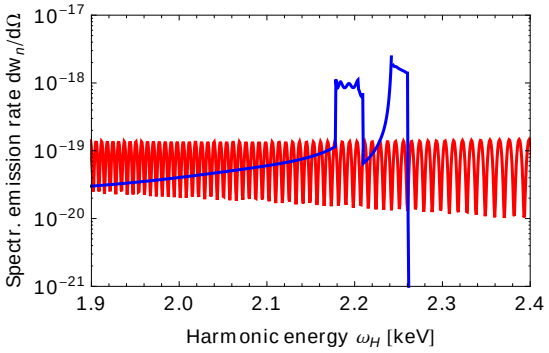

Figure 6.6: Single-atom HHG rate by the shaped pulse (blue) of Fig. 6.5 (a) and a conventional sinusoidal pulse (red) both assisted by an x-ray field.

necessarily to be very steep since all trajectories starting from 1 undergo the same field. For the same reason the shape in region 2 is allowed to deviate from the sinusoidal pulse which allows the low number of Fourier components of the optimized pulse.

For modelling we chose a zero range potential of $I_p = 5.68\,\text{a.u.}$, an x-ray energy of $\omega_X = 5.72\,\text{a.u.}$ and an x-ray electric field strength of $E_X = 0.3\,\text{a.u.}$. The sinusoidal laser field has an electric peak field strength of $E = 0.6\,\text{a.u.}$ and a frequency of $\omega = 0.05\,\text{a.u.}$. The optimized pulse shape in Fig. 6.5 (a) consists of only 15 harmonics of the fundamental laser frequency.

The enhancement of emission yield in the discussed energy regions can be observed in the spectrum, see Fig. 6.6. The most prominent features in the spectrum are the two dips with an enhanced yield of about two orders of magnitude over the low energy part and about one order of magnitude over the spectrum of the sinusoidal pulse. Each of the dips represents a different ionization direction of the electronic wave packet. We continue to discuss the spectrum quantitatively. At 2.2 keV the enhancement of the blue curve compared to the red curve is due to the chirping factor. The chirping factor for the blue curve is $\partial\omega_H/\partial t_i = 0.06\,\text{a.u.}$ whereas the corresponding long trajectory of the red curve has a chirping factor of $\partial\omega_H/\partial t_i = 14\,\text{a.u.}$. The actual enhancement of one order of magnitude is lower than the factor $14/0.06 \approx 230$ which could be expected. This is for two reasons: first, the red curve has contributions from the long and short trajectories whereas the blue originates from a long trajectory only. The amplitudes of short trajectories are about a factor of 2 larger than the amplitudes for the long trajectories. This is because of the different excursion times resulting in a different spreading behavior. Second, in the sinusoidal case, emission happens twice per laser cycle; our scheme fullfills the conditions for enhancement just once per cycle. Note that the ratio of the chirping factors of about 230 can be estimated by the ratio between the cutoff of the sinusoidal field ($\sim 2.8\,\text{keV}$) and the spectral width of the enhanced windows ($\sim 10 - 15\,\text{eV}$).

The oscillations in the dips are associated with the oscillations of the electric field in period 1 where it is close to zero. Accordingly, it could offer a way to determine pulse shapes close for fields close to zero. The cut off is lower than for a sinusoidal field because the rising edge of the shaped pulse (just at the beginning of region 2) is after the point

where the cutoff trajectory starts in the sinusoidal case. In the low energy part of the blue spectrum we do not observe the typical oscillations caused by the interference between the different contributing trajectories. This is because only short trajectories contribute. In fact, interference between the short downhill and uphill trajectories occurs but the oscillations are so slow that they are not visible. The similarity of the up- and downhill trajectories and, thus, the slow oscillation can be recognized by the small parameter $\sqrt{0.5p_i/U_p}$ [88].

In summary, the 5-dimensional functional determinant occurring in HHG SFA amplitudes has been investigated in detail. From this, we find that by tailoring an IR-pulse assisted by an x-ray field, we can increase the single-atom HHG yield in a specific energy window. The enhancement factor is given by the ratio between the cutoff energy of the reference pulse and the enhancement bandwidth subtracted by about one order of magnitude due to the nature of the contributing trajectories.

7 Conclusion and outlook

In this thesis, several strategies were developed to push forward the technique of high-harmonic generation towards higher photon energies and shorter harmonic pulse durations and to elucidate its fundamental mechanism.

The fundamental interference picture of HHG was extended to include the class of continuum-continuum (CC) transitions. By means of the model, it was found that a CC transition can play a dominant role in HHG for laser intensities in the saturation regime. An accurate analytical model was developed to describe the CC transition and the traditional HHG transition in the saturation regime in excellent agreement with numerical results. The new transition can potentially be exploited to gain structural information about atoms or molecules. This idea requires further investigations to address several questions. First, the precise phase-matching conditions to isolate the CC harmonics have to be determined. Second, it has to be investigated how the CC yield behaves in a multi-electron system to explore if it is enhanced as for the traditional CB HHG mechanism [109]. Third, it requires further investigation which structural information could be mapped out from the CC spectrum about the atom or molecule to obtain a new kind of molecular imaging [32, 33].

In Sec. 4, the possibility to generate harmonics in the relativistic regime was discussed and a macroscopic model was developed to describe the harmonic yield from a macroscopic gas target illuminated by relativistic laser intensities. Employing this model, two different single-atom schemes were optimized and advanced to allow for phase-matched emission from a macroscopic gas target: in Sec. 4.2, HHG from counterpropagating attosecond pulse trains was investigated. The existence of an additional phase of the emitted harmonics was found to depend on the delay time between the pulse trains. We showed that the phase can be tuned by varying the laser field intensity to compensate the phase mismatch caused by the free electron background. In the second setup (Sec. 4.3), the relativistic drift was compensated by means of an additional x-ray field. The phase-matching analysis revealed that the IR and x-ray beams have to co-propagate in order to achieve phase-matching in contrast to [82, 91]. Nevertheless, drift compensation can be achieved with a sufficiently high x-ray frequency. To obtain phase-matching on a macroscopic level, an additional weak counterpropagating IR field was employed.

Even when overcoming the relativistic drift and managing phase-matching, only a tiny HHG emission yield was obtained. Several reasons were identified: the phase-matched emission volume is, with a few tens of μm, still up to two orders of magnitude smaller than in many current experiments. This needs to be increased in order to have a practical photon source. When scaling to higher energies, the recolliding wave packet has a smaller probability for recombination. Instead, scattering is favored. Investigations have to be pursued as to how the recombination can be optimized. Moreover, we introduced the chirping factor describing the wave packet spread in terms of energy. It results in further

reduction of the HHG yield when the phase-matching bandwidth is not increased in the same way as the cutoff along with the laser intensity. A first proposal to overcome this reduction was presented in Sec. 6.2. As a future direction for the examination of relativistic harmonics also the theoretical model could be advanced, e.g., by employing a fully 3D propagation model for the laser pulse and using realistic ionic potentials instead of the employed zero-range potential.

Since the straightforward increase of the laser intensity to obtain multi-keV harmonics leads to a number of difficulties, we pursued another approach. In Chapter 5, the HHG energy is increased by rising the ionization potential at recombination. In a two-electron scheme, the recolliding continuum electron is forced to combine to a core hole by x-ray excitation of the core electron. The high ionization energy of the core level increases the HHG photon energy. We proved that the single-atom efficiency is at the same level as HHG from valence hole recombination for a x-ray intensity of $10^{16}\,\mathrm{W/cm^2}$. Through that technique, attosecond pulses in the x-ray domain could potentially be generated. As the new plateau sensitively depends on the shape of the high-frequency pulse, the process could offer the long-sought method to characterize x-ray pulses. It is necessary to find a way to solve this inverse problem. Additionally, phase-matching from the new plateau needs to be considered which is crucial to find experimental conditions for measurement. Moreover, the method could be combined with other ways increasing the HHG cutoff, e.g. long-wavelength drivers [97, 147]. Furthermore, from a theoretical point of view, it would be interesting to investigate the influence of the higher-order correction in our theory since for arbitrary x-ray pulse shapes in Sec. 5.2.2.

In Chapter 6, an approach is proposed as to how the recolliding wave packet can be shaped in position and momentum space. By using this technique certain harmonics in the spectrum can be enhanced and, much more importantly, it offers a possibility to arbitrarily shape the phase of the emitted harmonic pulses and to generate bandwidth-limited attosecond pulses. That technique avoids the requirement of filter elements to compensate the attochirp. If in the future, larger harmonic bandwidths become available, the technique could even be the only possibility to counteract the chirp because appropriate filters may not be available. However, the technique suffers from the fact that ionic gases have to be employed to suppress tunnel ionization. This is experimentally challenging and requires a low gas density to prevent phase-mismatch and deformation of the driving laser pulse. Modifying the scheme to combine it with an atomic gas would render it more interesting for experiment.

Bibliography

[1] National Research Council and Committee on Optical Science and Enginee, *Harnessing Light: Optical Science and Engineering for the 21st Century* (Natl Academy P, 1998).

[2] Lenkungskreis Optische Technologien f. d. 21 Jahrhundert, *Deutsche Agenda Optische Technologien für das 21. Jahrhundert* (VDI Verein Deutscher Ingenieure e.V., 2000).

[3] T. H. Maiman, "Stimulated optical radiation in ruby," Nature (London) **187**, 493–494 (1960).

[4] G. A. Mourou, T. Tajima, and S. V. Bulanov, "Optics in the relativistic regime," Rev. Mod. Phys. **78**, 309–371 (2006).

[5] D. Strickland and G. Mourou, "Compression of amplified chirped optical pulses," Opt. Commun. **56**, 219–221 (1985).

[6] R. W. Hellwarth, "Control of fluorescent pulsations," in "Advances in Quantum Electronics," , J. R. Singer, ed. (1961), p. 334.

[7] H. W. Mocker and R. J. Collins, "Mode competition and self-locking effects in a q-switched ruby laser," Appl. Phys. Lett. **7**, 270–273 (1965).

[8] V. Yanovsky, V. Chvykov, G. Kalinchenko, P. Rousseau, T. Planchon, T. Matsuoka, A. Maksimchuk, J. Nees, G. Cheriaux, G. Mourou, and K. Krushelnick, "Ultra-high intensity 300-TW laser at 0.1 hz repetition rate," Opt. Express **16**, 2109 (2008).

[9] *The Extreme Light Infrastructure European Project (ELI). Scientific Case* (http://www.extreme-light-infrastructure.eu/pictures/ELI-scientific-case-id17.pdf, 2007).

[10] T. Tajima and J. M. Dawson, "Laser electron accelerator," Phys. Rev. Lett. **43**, 267–270 (1979).

[11] V. Malka, S. Fritzler, E. Lefebvre, M. Aleonard, F. Burgy, J. Chambaret, J. Chemin, K. Krushelnick, G. Malka, S. P. D. Mangles, Z. Najmudin, M. Pittman, J. Rousseau, J. Scheurer, B. Walton, and A. E. Dangor, "Electron acceleration by a wake field forced by an intense ultrashort laser pulse," Science **298**, 1596–1600 (2002).

[12] H. Schwoerer, S. Pfotenhauer, O. Jäckel, K. Amthor, B. Liesfeld, W. Ziegler, R. Sauerbrey, K. W. D. Ledingham, and T. Esirkepov, "Laser plasma acceleration of quasi-monoenergetic protons from microstructured targets," Nature (London) **439**, 445–448 (2006).

[13] R. Kodama, P. A. Norreys, K. Mima, A. E. Dangor, R. G. Evans, H. Fujita, Y. Kitagawa, K. Krushelnick, T. Miyakoshi, N. Miyanaga, T. Norimatsu, S. J. Rose, T. Shozaki, K. Shigemori, A. Sunahara, M. Tampo, K. A. Tanaka, Y. Toyama, T. Yamanaka, and M. Zepf, "Fast heating of ultrahigh-density plasma as a step towards laser fusion ignition," Nature (Lodon) **412**, 798–802 (2001).

[14] K. W. D. Ledingham, P. McKenna, and R. P. Singhal, "Applications for nuclear phenomena generated by ultra-intense lasers," Science **300**, 1107–1111 (2003).

[15] C. Müller, A. D. Piazza, A. Shahbaz, T. J. Bürvenich, J. Evers, K. Hatsagortsyan, and C. H. Keitel, "High-energy, nuclear and QED processes in strong laser fields," Las. Phys. **18**, 3 (2008).

[16] C. Müller, K. Z. Hatsagortsyan, and C. H. Keitel, "Particle physics with a laser-driven positronium atom," Physics Letters B **659**, 209 – 213 (2008).

[17] M. Nisoli, S. de Silvestri, and O. Svelto, "Generation of high energy 10 fs pulses by a new pulse compression technique," Applied Physics Letters **68**, 2793–2795 (1996).

[18] M. Nisoli, S. D. Silvestri, O. Svelto, R. Szipöcs, K. Ferencz, C. Spielmann, S. Sartania, and F. Krausz, "Compression of high-energy laser pulses below 5 fs," Opt. Lett. **22**, 522–524 (1997).

[19] B. Schenkel, J. Biegert, U. Keller, C. Vozzi, M. Nisoli, G. Sansone, S. Stagira, S. D. Silvestri, and O. Svelto, "Generation of 3.8-fs pulses from adaptive compression of a cascaded hollow fiber supercontinuum," Opt. Lett. **28**, 1987–1989 (2003).

[20] A. Baltuška, T. Fuji, and T. Kobayashi, "Controlling the carrier-envelope phase of ultrashort light pulses with optical parametric amplifiers," Phys. Rev. Lett. **88**, 133901 (2002).

[21] A. Baltuška, T. Udem, M. Uiberacker, M. Hentschel, E. Goulielmakis, C. Gohle, R. Holzwarth, V. S. Yakovlev, A. Scrinzi, T. W. Hänsch, and F. Krausz, "Attosecond control of electronic processes by intense light fields," Nature (London) **421**, 611–615 (2003).

[22] P. A. Franken, A. E. Hill, C. W. Peters, and G. Weinreich, "Generation of optical harmonics," Phys. Rev. Lett. **7**, 118–119 (1961).

[23] R. W. Boyd, *Nonlinear Optics* (Academic Press, 2008), 3rd ed.

[24] P. Agostini, F. Fabre, G. Mainfray, G. Petite, and N. K. Rahman, "Free-free transitions following six-photon ionization of xenon atoms," Phys. Rev. Lett. **42**, 1127–1130 (1979).

[25] A. l'Huillier, L. A. Lompre, G. Mainfray, and C. Manus, "Multiply charged ions induced by multiphoton absorption in rare gases at 0.53 μm," Phys. Rev. A **27**, 2503–2512 (1983).

[26] D. N. Fittinghoff, P. R. Bolton, B. Chang, and K. C. Kulander, "Observation of nonsequential double ionization of helium with optical tunneling," Phys. Rev. Lett. **69**, 2642–2645 (1992).

[27] A. McPherson, G. Gibson, H. Jara, U. Johann, T. S. Luk, I. A. McIntyre, K. Boyer, and C. K. Rhodes, "Studies of multiphoton production of vacuum-ultraviolet radiation in the rare gases," J. Opt. Soc. Am. B **4**, 595–601 (1987).

[28] P. B. Corkum, "Plasma perspective on strong-field multiphoton ionization," Phys. Rev. Lett. **71**, 1994–1997 (1993).

[29] K. C. Kulander, K. J. Schafer, and J. L. Krause, "Dynamics of short-pulse excitation, ionization and harmonic conversion," in "Presented at the NATO Workshop, Han-Sur-Lesse, Belgium, 8-14 Jan. 1993," , M. G. Blain, G. D. Tipton, W. M. Holber, P. L. Westerfield, and K. L. Maxwell, eds. (1993), pp. 8–14.

[30] E. Seres, J. Seres, and C. Spielmann, "X-ray absorption spectroscopy in the keV range with laser generated high harmonic radiation," Appl. Phys. Lett **89**, 181919 (2006).

[31] M. Lewenstein, P. Salières, and A. L'Huillier, "Phase of the atomic polarization in high-order harmonic generation," Phys. Rev. A **52**, 4747–4754 (1995).

[32] T. Morishita, A.-T. Le, Z. Chen, and C. D. Lin, "Accurate retrieval of structural information from laser-induced photoelectron and high-order harmonic spectra by few-cycle laser pulses," Phys. Rev. Lett. **100**, 013903 (2008).

[33] J. Itatani, J. Levesque, D. Zeidler, H. Niikura, H. Pepin, J. C. Kieffer, P. B. Corkum, and D. M. Villeneuve, "Tomographic imaging of molecular orbitals," Nature **432**, 867–871 (2004).

[34] M. Lein, N. Hay, R. Velotta, J. P. Marangos, and P. L. Knight, "Role of the intramolecular phase in high-harmonic generation," Phys. Rev. Lett. **88**, 183903 (2002).

[35] R. d. Nalda, E. Heesel, M. Lein, N. Hay, R. Velotta, E. Springate, M. Castillejo, and J. P. Marangos, "Role of orbital symmetry in high-order harmonic generation from aligned molecules," Phys. Rev. A **69**, 031804 (2004).

[36] M. Lein, "Attosecond probing of vibrational dynamics with high-harmonic generation," Phys. Rev. Lett. **94**, 053004 (2005).

[37] M. Nisoli and G. Sansone, "New frontiers in attosecond science," Progress in Quantum Electronics **33**, 17 – 59 (2009).

[38] Z. Chang and P. Corkum, "Attosecond photon sources: the first decade and beyond," J. Opt. Soc. Am. B **27**, B9–B17 (2010).

[39] G. Sansone, E. Benedetti, F. Calegari, C. Vozzi, L. Avaldi, R. Flammini, L. Poletto, P. Villoresi, C. Altucci, R. Velotta, S. Stagira, S. D. Silvestri, and M. Nisoli, "Isolated single-cycle attosecond pulses," Science **314**, 443–446 (2006).

[40] E. Goulielmakis, M. Schultze, M. Hofstetter, V. S. Yakovlev, J. Gagnon, M. Uiberacker, A. L. Aquila, E. M. Gullikson, D. T. Attwood, R. Kienberger, F. Krausz, and U. Kleineberg, "Single-cycle nonlinear optics," Science **320**, 1614–1617 (2008).

[41] D. H. Ko, K. T. Kim, J. Park, J. hwan Lee, and C. H. Nam, "Attosecond chirp compensation over broadband high-order harmonics to generate near transform-limited 63 as pulses," New J. Phys. **12**, 063008 (2010).

[42] F. Krausz and M. Ivanov, "Attosecond physics," Rev. Mod. Phys. **81**, 163–234 (2009).

[43] R. Kienberger, M. Uiberacker, M. F. Kling, and F. Krausz, "Attosecond physics comes of age: from tracing to steering electrons at sub-atomic scales," J. Mod. Opt. **54**, 1985–1998 (2007).

[44] A. Scrinzi, M. Y. Ivanov, R. Kienberger, and D. M. Villeneuve, "Attosecond physics," J. Phys. B **39**, R1–R37 (2006).

[45] C. Brif, R. Chakrabarti, and H. Rabitz, "Control of quantum phenomena: past, present and future," New Journal of Physics **12**, 075008 (2010).

[46] T. Ergler, A. Rudenko, B. Feuerstein, K. Zrost, C. D. Schröter, R. Moshammer, and J. Ullrich, "Time-resolved imaging and manipulation of H_2 fragmentation in intense laser fields," Phys. Rev. Lett. **95**, 093001 (2005).

[47] B. Feuerstein, T. Ergler, A. Rudenko, K. Zrost, C. D. Schröter, R. Moshammer, J. Ullrich, T. Niederhausen, and U. Thumm, "Complete characterization of molecular dynamics in ultrashort laser fields," Phys. Rev. Lett. **99**, 153002 (2007).

[48] T. Ergler, B. Feuerstein, A. Rudenko, K. Zrost, C. D. Schröter, R. Moshammer, and J. Ullrich, "Quantum-phase resolved mapping of ground-state vibrational D_2 wave packets via selective depletion in intense laser pulses," Phys. Rev. Lett. **97**, 103004 (2006).

[49] A. Mokhtari, P. Cong, J. L. Herek, and A. H. Zewail, "Direct femtosecond mapping of trajectories in a chemical reaction," Nature (London) **348**, 225–227 (1990).

[50] G. M. Gale, G. Gallot, F. Hache, N. Lascoux, S. Bratos, and J.-C. Leicknam, "Femtosecond dynamics of hydrogen bonds in liquid water: A real time study," Phys. Rev. Lett. **82**, 1068–1071 (1999).

[51] M. Hentschel, R. Kienberger, C. Spielmann, G. A. Reider, N. Milosevic, T. Brabec, P. Corkum, U. Heinzmann, M. Drescher, and F. Krausz, "Attosecond metrology," Nature (London) **414**, 509–513 (2001).

[52] E. Goulielmakis, M. Uiberacker, R. Kienberger, A. Baltuška, V. Yakovlev, A. Scrinzi, T. Westerwalbesloh, U. Kleineberg, U. Heinzmann, M. Drescher, and F. Krausz, "Direct measurement of light waves," Science **305**, 1267 (2004).

[53] I. Thomann, E. Gregonis, X. Liu, R. Trebino, A. S. Sandhu, M. M. Murnane, and H. C. Kapteyn, "Temporal characterization of attosecond wave forms in the sub-optical-cycle regime," Phys. Rev. A **78**, 011806 (2008).

[54] R. Kienberger, E. Goulielmakis, M. Uiberacker, A. Baltuška, V. Yakovlev, F. Bammer, A. Scrinzi, T. Westerwalbesloh, U. Kleineberg, U. Heinzmann, M. Drescher, and F. Krausz, "Atomic transient recorder," Nature (London) **427**, 817 (2004).

[55] M. Drescher, M. Hentschel, R. Kienberger, M. Uiberacker, V. Yakovlev, A. Scrinzi, T. Westerwalbesloh, U. Kleineberg, U. Heinzmann, and F. Krausz, "Time-resolved atomic inner-shell spectroscopy," Nature (London) **419**, 803–807 (2002).

[56] M. Uiberacker, T. Uphues, M. Schultze, A. J. Verhoef, V. Yakovlev, M. F. Kling, J. Rauschenberger, N. M. Kabachnik, H. Schröder, M. Lezius, K. L. Kompa, H.-G. Muller, M. J. J. Vrakking, S. Hendel, U. Kleineberg, U. Heinzmann, M. Drescher, and F. Krausz, "Attosecond real-time observation of electron tunnelling in atoms," Nature (London) **446**, 627–632 (2007).

[57] A. L. Cavalieri, N. Müller, T. Uphues, V. S. Yakovlev, A. Baltusška, B. S. B. Horvath and, L. Blümel, S. H. R. Holzwarth, M. Drescher, U. Kleineberg, P. M. Echenique, R. Kienberger, F. Krausz, and U. Heinzmann, "Attosecond spectroscopy in condensed matter," Nature (London) **449**, 1029–1032 (2007).

[58] S. Chelkowski, P. B. Corkum, and A. D. Bandrauk, "Femtosecond coulomb explosion imaging of vibrational wave functions," Phys. Rev. Lett. **82**, 3416–3419 (1999).

[59] T. Ergler, A. Rudenko, B. Feuerstein, K. Zrost, C. D. Schröter, R. Moshammer, and J. Ullrich, "Spatiotemporal imaging of ultrafast molecular motion: Collapse and revival of the D_2^+ nuclear wave packet," Phys. Rev. Lett. **97**, 193001 (2006).

[60] C. D. Lin, X. M. Tong, and T. Morishita, "Direct experimental visualization of atomic and electron dynamics with attosecond pulses," J. Phys. B **39**, S419 (2006).

[61] A. S. Alnaser, B. Ulrich, X. M. Tong, I. V. Litvinyuk, C. M. Maharjan, P. Ranitovic, T. Osipov, R. Ali, S. Ghimire, Z. Chang, C. D. Lin, and C. L. Cocke, "Simultaneous real-time tracking of wave packets evolving on two different potential curves in H_2^+ and D_2^+," Phys. Rev. A **72**, 030702 (2005).

[62] S. X. Hu and L. A. Collins, "Attosecond pump probe: exploring ultrafast electron motion inside an atom," Phys. Rev. Lett. **96**, 073004 (2006).

[63] H. A. Weidenmüller, "Nuclear excitation by a zeptosecond multi-mev laser pulse," Phys. Rev. Lett. **106**, 122502 (2011).

[64] R. Neutze, R. Wouts, D. van der Spoel, E. Weckert, and J. Hajdu, "Potential for biomolecular imaging with femtosecond x-ray pulses," Nature (London) **406**, 752–757 (2000).

[65] C. H. Keitel, P. L. Knight, and K. Burnett, "Relativistic high-harmonic generation," Euro. Phys. Lett. **24**, 539 (1993).

[66] O. Latinne, C. J. Joachain, and M. Dörr, "Atomic hydrogen in a superintense high-frequency field: Testing the dipole approximation," Euro. Phys. Lett. **26**, 333 (1994).

[67] N. J. Kylstra, R. A. Worthington, A. Patel, P. L. Knight, J. R. Vázquez de Aldana, and L. Roso, "Breakdown of stabilization of atoms interacting with intense, high-frequency laser pulses," Phys. Rev. Lett. **85**, 1835–1838 (2000).

[68] C. C. Chirilă, N. J. Kylstra, R. M. Potvliege, and C. J. Joachain, "Nondipole effects in photon emission by laser-driven ions," Phys. Rev. A **66**, 063411 (2002).

[69] M. W. Walser, C. H. Keitel, A. Scrinzi, and T. Brabec, "High harmonic generation beyond the electric dipole approximation," Phys. Rev. Lett. **85**, 5082–5085 (2000).

[70] G. R. Mocken and C. H. Keitel, "Bound atomic dynamics in the MeV regime," J. Phys. B **37**, L275 (2004).

[71] C. C. Chirilă, C. J. Joachain, N. J. Kylstra, and R. M. Potvliege, "Interaction of superintense laser pulses with relativistic ions," Phys. Rev. Lett. **93**, 243603 (2004).

[72] B. Henrich, K. Z. Hatsagortsyan, and C. H. Keitel, "Positronium in intense laser fields," Phys. Rev. Lett. **93**, 013601 (2004).

[73] K. Z. Hatsagortsyan, C. Müller, and C. H. Keitel, "Microscopic laser-driven high-energy colliders," Euro. Phys. Lett. **76**, 29 (2006).

[74] V. D. Taranukhin, "Relativistic high-order harmonic generation," Las. Phys. **10**, 330–336 (2000).

[75] M. Verschl and C. H. Keitel, "Relativistic recollisions with two consecutive laser pulses," Journal of Physics B: Atomic, Molecular and Optical Physics **40**, F69 (2007).

[76] M. Verschl and C. H. Keitel, "Refocussed relativistic recollisions," Euro. Phys. Lett. **77**, 64004 (2007).

[77] M. Verschl and C. H. Keitel, "Relativistic classical and quantum dynamics in intense crossed laser beams of various polarizations," Phys. Rev. ST Accel. Beams **10**, 024001 (2007).

[78] N. Milosevic, P. B. Corkum, and T. Brabec, "How to use lasers for imaging attosecond dynamics of nuclear processes," Phys. Rev. Lett. **92**, 013002 (2004).

[79] C. Liu, M. C. Kohler, K. Z. Hatsagortsyan, C. Müller, and C. H. Keitel, "Laser-guided relativistic quantum dynamics," New Journal of Physics **11**, 105045 (2009).

[80] M. Klaiber, K. Z. Hatsagortsyan, and C. H. Keitel, "Relativistic ionization rescattering with tailored laser pulses," Phys. Rev. A **74**, 051803 (2006).

[81] M. Klaiber, K. Z. Hatsagortsyan, and C. H. Keitel, "Fully relativistic laser-induced ionization and recollision processes," Phys. Rev. A **75**, 063413 (2007).

[82] K. Z. Hatsagortsyan, M. Klaiber, C. Müller, M. C. Kohler, and C. H. Keitel, "Laser-driven relativistic recollisions," J. Opt. Soc. Am. B **25**, B92–B103 (2008).

[83] M. Klaiber, K. Z. Hatsagortsyan, and C. H. Keitel, "Zeptosecond γ-ray pulses," (2007). arXiv:00707.2900.

[84] P. Koval, F. Wilken, D. Bauer, and C. H. Keitel, "Nonsequential double recombination in intense laser fields," Phys. Rev. Lett. **98**, 043904 (2007).

[85] K. Ishikawa, "Photoemission and ionization of He^+ under simultaneous irradiation of fundamental laser and high-order harmonic pulses," Phys. Rev. Lett. **91**, 043002 (2003).

[86] K. J. Schafer, M. B. Gaarde, A. Heinrich, J. Biegert, and U. Keller, "Strong field quantum path control using attosecond pulse trains," Phys. Rev. Lett. **92**, 023003 (2004).

[87] E. J. Takahashi, T. Kanai, K. L. Ishikawa, Y. Nabekawa, and K. Midorikawa, "Dramatic enhancement of high-order harmonic generation," Phys. Rev. Lett. **99**, 053904 (2007).

[88] C. Figueira de Morisson Faria and P. Salières, "High-order harmonic generation with a strong laser field and an attosecond-pulse train: The Dirac-Delta comb and monochromatic limits," Laser Physics **17**, 390–400 (2007).

[89] M. B. Gaarde, K. J. Schafer, A. Heinrich, J. Biegert, and U. Keller, "Large enhancement of macroscopic yield in attosecond pulse train–assisted harmonic generation," Phys. Rev. A **72**, 013411 (2005).

[90] S. V. Popruzhenko, D. F. Zaretsky, and W. Becker, "High-order harmonic generation by an intense infrared laser pulse in the presence of a weak uv pulse," Phys. Rev. A **81**, 063417 (2010).

[91] K. Z. Hatsagortsyan, M. Klaiber, C. Müller, and C. H. Keitel, "Coherent hard x rays from attosecond pulse train-assisted harmonic generation," Opt. Lett. **33**, 411–413 (2008).

[92] A. Fleischer, "Generation of higher-order harmonics upon the addition of high-frequency XUV radiation to IR radiation: Generalization of the three-step model," Phys. Rev. A **78**, 053413 (2008).

[93] A. Fleischer and N. Moiseyev, "Amplification of high-order harmonics using weak perturbative high-frequency radiation," Phys. Rev. A **77**, 010102 (2008).

[94] T. Pfeifer, D. Walter, C. Winterfeldt, C. Spielmann, and G. Gerber, "Controlling the spectral shape of coherent soft x-rays," Appl. Phys. B **80**, 277–280.

[95] S. B. P. Radnor, L. E. Chipperfield, P. Kinsler, and G. H. C. New, "Carrier-wave steepened pulses and gradient-gated high-order harmonic generation," Phys. Rev. A **77**, 033806 (2008).

[96] L. E. Chipperfield, J. S. Robinson, J. W. G. Tisch, and J. P. Marangos, "Ideal waveform to generate the maximum possible electron recollision energy for any given oscillation period," Phys. Rev. Lett. **102**, 063003 (2009).

[97] M.-C. Chen, P. Arpin, T. Popmintchev, M. Gerrity, B. Zhang, M. Seaberg, D. Popmintchev, M. M. Murnane, and H. C. Kapteyn, "Bright, coherent, ultrafast soft x-ray harmonics spanning the water window from a tabletop light source," Phys. Rev. Lett. **105**, 173901 (2010).

[98] Y. Mairesse, A. de Bohan, L. J. Frasinski, H. Merdji, L. C. Dinu, P. Monchicourt, P. Breger, M. Kovačev, R. Taïeb, B. Carré, H. G. Muller, P. Agostini, and P. Salières, "Attosecond synchronization of high-harmonic soft x-rays," Science **302**, 1540–1543 (2003).

[99] S. Kazamias and P. Balcou, "Intrinsic chirp of attosecond pulses: Single-atom model versus experiment," Phys. Rev. A **69**, 063416 (2004).

[100] K. T. Kim, C. M. Kim, M.-G. Baik, G. Umesh, and C. H. Nam, "Single sub-50-attosecond pulse generation from chirp-compensated harmonic radiation using material dispersion," Phys. Rev. A **69**, 051805 (2004).

[101] R. López-Martens, K. Varjú, P. Johnsson, J. Mauritsson, Y. Mairesse, P. Salières, M. B. Gaarde, K. J. Schafer, A. Persson, S. Svanberg, C.-G. Wahlström, and A. L'Huillier, "Amplitude and phase control of attosecond light pulses," Phys. Rev. Lett. **94**, 033001 (2005).

[102] A. Pukhov, S. Gordienko, and T. Baeva, "Temporal structure of attosecond pulses from intense laser-atom interactions," Phys. Rev. Lett. **91**, 173002 (2003).

[103] M. Y. Emelin, M. Y. Ryabikin, and A. M. Sergeev, "Single attosecond burst generation during ionization of excited atoms by intense ultrashort laser pulses," JETP **106**, 203 (2008).

[104] W. Becker, A. Lohr, M. Kleber, and M. Lewenstein, "A unified theory of high-harmonic generation: Application to polarization properties of the harmonics," Phys. Rev. A **56**, 645–656 (1997).

[105] M. Y. Kuchiev and V. N. Ostrovsky, "Quantum theory of high harmonic generation as a three-step process," Phys. Rev. A **60**, 3111–3124 (1999).

[106] D. B. Milošević, "A semi-classical model for high-harmonic generation," in "Super-Intense Laser-Atom Physics," , vol. 12 of *NATO Science Series II: Mathematics, Physics and Chemistry*, B. Piraux and K. Rzazewski, eds. (Kluwer, Dordrecht, 2001), vol. 12 of *NATO Science Series II: Mathematics, Physics and Chemistry*, pp. 229–238.

[107] L. Plaja and J. A. Pérez-Hernández, "A quantitative S-Matrix approach to high-order harmonic generation from multiphoton to tunneling regimes," Opt. Express **15**, 3629 (2007).

[108] J. A. Pérez-Hernández and L. Plaja, "Quantum description of the high-order harmonic generation in multiphoton and tunneling regimes," Phys. Rev. A **76**, 023829 (2007).

[109] A. Gordon, F. X. Kärtner, N. Rohringer, and R. Santra, "Role of many-electron dynamics in high harmonic generation," Phys. Rev. Lett. **96**, 223902 (2006).

[110] R. Santra and A. Gordon, "Three-step model for high-harmonic generation in many-electron systems," Phys. Rev. Lett. **96**, 073906 (2006).

[111] M. Y. Ivanov, T. Brabec, and N. Burnett, "Coulomb corrections and polarization effects in high-intensity high-harmonic emission," Phys. Rev. A **54**, 742–745 (1996).

[112] S. Augst, D. Strickland, D. D. Meyerhofer, S. L. Chin, and J. H. Eberly, "Tunneling ionization of noble gases in a high-intensity laser field," Phys. Rev. Lett. **63**, 2212–2215 (1989).

[113] S. Palaniyappan, I. Ghebregziabher, A. DiChiara, J. MacDonald, and B. C. Walker, "Emergence from nonrelativistic strong-field rescattering to ultrastrong-field laser-atom physics: A semiclassical analysis," Phys. Rev. A **74**, 033403 (2006).

[114] E. S. Sarachik and G. T. Schappert, "Classical theory of the scattering of intense laser radiation by free electrons," Phys. Rev. D **1**, 2738–2753 (1970).

[115] M. W. Walser, D. J. Urbach, K. Z. Hatsagortsyan, S. X. Hu, and C. H. Keitel, "Spin and radiation in intense laser fields," Phys. Rev. A **65**, 043410 (2002).

[116] M. Klaiber, K. Z. Hatsagortsyan, and C. H. Keitel, "Above-threshold ionization beyond the dipole approximation," Phys. Rev. A **71**, 033408 (2005).

[117] Y. I. Salamin, S. X. Hu, K. Z. Hatsagortsyan, and C. H. Keitel, "Relativistic high-power laser matter interactions," Phys. Rep. **427**, 41–155 (2006).

[118] L. V. Keldysh, "Ionization in the field of a strong electromagnetic wave," Sov. Phys. JETP **20**, 1307 (1965).

[119] F. H. M. Faisal, "Multiple absorption of laser photons by atoms," Journal of Physics B Atomic Molecular Physics **6**, L89–L92 (1973).

[120] H. R. Reiss, "Effect of an intense electromagnetic field on a weakly bound system," Phys. Rev. A **22**, 1786–1813 (1980).

[121] H. G. Muller, "Numerical simulation of high-order above-threshold-ionization enhancement in argon," Phys. Rev. A **60**, 1341–1350 (1999).

[122] D. Bauer and P. Koval, "Qprop: A Schrödinger-solver for intense laser-atom interaction." Comput. Phys. Commun. **174**, 396 (2006).

[123] M. Ruf, H. Bauke, and C. H. Keitel, "A real space split operator method for the Klein-Gordon equation," J. Comput. Phys. **228**, 9092–9106 (2009).

[124] G. R. Mocken and C. H. Keitel, "FFT-split-operator code for solving the Dirac equation in 2+1 dimensions," Comput. Phys. Commun. **178**, 868–882 (2008).

[125] D. Bauer, D. B. Milošević, and W. Becker, "Strong-field approximation for intense-laser–atom processes: The choice of gauge," Phys. Rev. A **72**, 023415 (2005).

[126] A.-T. Le, T. Morishita, and C. D. Lin, "Extraction of the species-dependent dipole amplitude and phase from high-order harmonic spectra in rare-gas atoms," Phys. Rev. A **78**, 023814 (2008).

[127] K. C. Kulander, "Time-dependent theory of multiphoton ionization of xenon," Phys. Rev. A **38**, 778–787 (1988).

[128] M. Lewenstein, P. Balcou, M. Y. Ivanov, A. L'Huillier, and P. B. Corkum, "Theory of high-harmonic generation by low-frequency laser fields," Phys. Rev. A **49**, 2117–2132 (1994).

[129] G. G. Paulus, W. Nicklich, H. Xu, P. Lambropoulos, and H. Walther, "Plateau in above threshold ionization spectra," Phys. Rev. Lett. **72**, 2851–2854 (1994).

[130] W. Becker, S. Long, and J. K. McIver, "Modeling harmonic generation by a zero-range potential," Phys. Rev. A **50**, 1540–1560 (1994).

[131] D. B. Milošević and W. Becker, "Role of long quantum orbits in high-order harmonic generation," Phys. Rev. A **66**, 063417 (2002).

[132] W. Gordon, "Der Comptoneffekt nach der Schrödingerschen Theorie," Z. Phys. **50**, 117 (1926).

[133] D. M. Volkov, "Über eine Klasse von Lösungen der Diracschen Gleichung," Z. Phys. **94**, 250 (1935).

[134] H. R. Reiss, "Complete keldysh theory and its limiting cases," Phys. Rev. A **42**, 1476–1486 (1990).

[135] H. R. Reiss, "Relativistic strong-field photoionization," J. Opt. Soc. Am. B **7**, 574–586 (1990).

[136] M. Klaiber, K. Z. Hatsagortsyan, and C. H. Keitel, "Gauge-invariant relativistic strong-field approximation," Phys. Rev. A **73**, 053411 (2006).

[137] D. B. Milošević, S. Hu, and W. Becker, "Quantum-mechanical model for ultrahigh-order harmonic generation in the moderately relativistic regime," Phys. Rev. A **63**, 011403 (2000).

[138] G. B. Arfken and H. J. Weber, *Mathematical methods for physicists* (Elsevier Academic Press, New York, 2005), sixth ed.

[139] H. G. Muller, "An efficient propagation scheme for the time-dependent Schrödinger equation in the velocity gauge," Las. Phys. **9**, 138 (1999).

[140] H. Feshbach and F. Villars, "Elementary relativistic wave mechanics of spin 0 and spin 1/2 particles," Rev. Mod. Phys. **30**, 24–45 (1958).

[141] E. Esarey, P. Sprangle, J. Krall, and A. Ting, "Self-focusing and guiding of short laser pulses in ionizing gases and plasmas," IEEE J. Quantum Electron. **33**, 1879–1914 (1997).

[142] M. B. Gaarde, J. L. Tate, and K. J. Schafer, "Macroscopic aspects of attosecond pulse generation," J. Phys. B **41**, 132001 (2008).

[143] V. V. Strelkov, V. T. Platonenko, and A. Becker, "High-harmonic generation in a dense medium," Phys. Rev. A **71**, 053808 (2005).

[144] C. G. Durfee, A. R. Rundquist, S. Backus, C. Herne, M. M. Murnane, and H. C. Kapteyn, "Phase matching of high-order harmonics in hollow waveguides," Phys. Rev. Lett. **83**, 2187–2190 (1999).

[145] G. Tempea, M. Geissler, M. Schnürer, and T. Brabec, "Self-phase-matched high harmonic generation," Phys. Rev. Lett. **84**, 4329–4332 (2000).

[146] M. Geissler, G. Tempea, and T. Brabec, "Phase-matched high-order harmonic generation in the nonadiabatic limit," Phys. Rev. A **62**, 033817 (2000).

[147] T. Popmintchev, M.-C. Chen, A. Bahabad, M. Gerrity, P. Sidorenko, O. Cohen, I. P. Christov, M. M. Murnane, and H. C. Kapteyn, "Phase matching of high harmonic generation in the soft and hard x-ray regions of the spectrum," Proc. Nat. Acad. Sci. USA **106**, 10516–10521 (2009).

[148] J. Peatross, S. Voronov, and I. Prokopovich, "Selective zoning of high harmonic emission using counter-propagating light," Opt. Express **1**, 114–125 (1997).

[149] O. Cohen, X. Zhang, A. L. Lytle, T. Popmintchev, M. M. Murnane, and H. C. Kapteyn, "Grating-assisted phase matching in extreme nonlinear optics," Phys. Rev. Lett. **99**, 053902 (2007).

[150] C. Serrat and J. Biegert, "All-regions tunable high harmonic enhancement by a periodic static electric field," Phys. Rev. Lett. **104**, 073901 (2010).

[151] I. Christov, H. Kapteyn, and M. Murnane, "Quasi-phase matching of high-harmonics and attosecond pulses in modulated waveguides," Opt. Express **7**, 362–367 (2000).

[152] A. Paul, R. A. Bartels, R. Tobey, H. Green, S. Weiman, I. P. Christov, M. M. Murnane, H. C. Kapteyn, and S. Backus, "Quasi-phase-matched generation of coherent extreme-ultraviolet light," Nature (London) **421**, 51–54 (2003).

[153] E. A. Gibson, A. Paul, N. Wagner, R. Tobey, D. Gaudiosi, S. Backus, I. P. Christov, A. Aquila, E. M. Gullikson, D. T. Attwood, M. M. Murnane, and H. C. Kapteyn, "Coherent soft x-ray generation in the water window with quasi-phase matching," Science **302**, 95–98 (2003).

[154] M. Protopapas, D. G. Lappas, C. H. Keitel, and P. L. Knight, "Recollisions, bremsstrahlung, and attosecond pulses from intense laser fields," Phys. Rev. A **53**, R2933–R2936 (1996).

[155] D. B. Milošević and F. Ehlotzky, "Scattering and reaction processes in powerful laser fields," Adv. At. Mol. Opt. Phys. **49**, 373 (2003).

[156] D. G. Lappas, M. V. Fedorov, and J. H. Eberly, "Spectrum of light scattered by a strongly driven atom," Phys. Rev. A **47**, 1327–1335 (1993).

[157] K. Burnett, V. C. Reed, J. Cooper, and P. L. Knight, "Calculation of the background emitted during high-harmonic generation," Phys. Rev. A **45**, 3347–3349 (1992).

[158] R. Heck, "Erzeugung hoher Harmonischer durch Interferenz freier Elektronenwellenpakete / Charakterisierung und Einrichtung eines Toroidalspiegels," Bachelor thesis, University of Heidelberg (2010).

[159] D. Gabor, J. Inst. Electr. Eng. **93**, 429 (1946).

[160] W. C. Lang and K. Forinash, "Time-frequency analysis with the continuous wavelet transform," Am. J. Phys. **66**, 794 (1998).

[161] A. M. Perelomov, V. S. Popov, and M. V. Terent'ev, "Ionization of atoms in an alternating electric field," Sov. Phys. JETP **23**, 924 (1966).

[162] M. V. Ammosov, N. B. Delone, and V. P. Krainov, "Tunnel ionization of complex atoms and of atomic ions in an alternating electromagnetic field," Sov. Phys. JETP **64**, 1191 (1986).

[163] X. M. Tong and C. D. Lin, "Empirical formula for static field ionization rates of atoms and molecules by lasers in the barrier-suppression regime," J. Phys. B **38**, 2593 (2005).

[164] D. Bauer and P. Mulser, "Exact field ionization rates in the barrier-suppression regime from numerical time-dependent Schrödinger-equation calculations," Phys. Rev. A **59**, 569–577 (1999).

[165] A. Gordon and F. X. Kärtner, "Quantitative modeling of single atom high harmonic generation," Phys. Rev. Lett. **95**, 223901 (2005).

[166] A. Gordon and F. Kärtner, "Scaling of kev HHG photon yield with drive wavelength," Opt. Express **13**, 2941–2947 (2005).

[167] C. C. Chirilă, "Analysis of the strong field approximation for harmonic generation and multiphoton ionization in intense ultrashort laser pulses," Ph.D. thesis, The University of Durham, Department of Physics (2004).

[168] P. Balcou, A. S. Dederichs, M. B. Gaarde, and A. L'Huillier, "Quantum-path analysis and phase matching of high-order harmonic generation and high-order frequency mixing processes in strong laser fields," J. Phys. B **32**, 2973–2989 (1999).

[169] S. X. Hu, D. B. Milošević, W. Becker, and W. Sandner, "High-efficiency high-order harmonic generation without tunneling," Phys. Rev. A **64**, 013410 (2001).

[170] S. X. Hu, A. F. Starace, W. Becker, W. Sandner, and D. B. Milošević, "Nontunnelling high-order harmonics from ultra-intense laser-driven tightly bound systems," J. Phys. B **35**, 627 (2002).

[171] D. C. Yost, T. R. Schibli, J. Ye, J. L. Tate, J. Hostetter, K. J. Schafer, and M. B. Gaarde, "Below-threshold harmonics for vuv frequency combs," Phys. Rev. Lett. (2009).

[172] E. P. Power, A. M. March, F. Catoire, E. Sistrunk, K. Krushelnick, P. Agostini, and L. F. DiMauro, "XFROG phase measurement of threshold harmonics in a keldysh-scaled system," Nature Photon. **4**, 352 (2010).

[173] Q. Lin, S. Li, and W. Becker, "High-order harmonic generation in a tightly focused laser beam," Opt. Lett. **31**, 2163–2165 (2006).

[174] E. Priori, G. Cerullo, M. Nisoli, S. Stagira, S. De Silvestri, P. Villoresi, L. Poletto, P. Ceccherini, C. Altucci, R. Bruzzese, and C. de Lisio, "Nonadiabatic three-dimensional model of high-order harmonic generation in the few-optical-cycle regime," Phys. Rev. A **61**, 063801 (2000).

[175] "Radiation spectra of laser-driven quantum relativistic electrons," Comp. Phys. Comm. **166**, 171 – 190 (2005).

[176] J. D. Jackson, *Classical Electrodynamics*, vol. 3 (Wiley, 1998).

[177] L. D. Landau and E. M. Lifshitz, *The classical theory of fields, by L. D. Landau and E. M. Lifshitz. Translated from the Russian by Morton Hamermesh* (Pergamon Press; Addison-Wesley Pub. Co., Oxford, Reading, Mass.,, 1962), rev. 2d ed. ed.

[178] J. Bjorken and S. Drell, *Relativistic Quantum Mechanics* (McGraw-Hill Book Company, San Francisco, 194), 1st ed.

[179] D. B. Milošević, S. X. Hu, and W. Becker, "Relativistic ultrahigh-order harmonic generation," Las. Phys. **12**, 389–397 (2002).

[180] O. Smirnova, M. Spanner, and M. Ivanov, "Analytical solutions for strong field-driven atomic and molecular one- and two-electron continua and applications to strong-field problems," Phys. Rev. A **77**, 033407 (2008).

[181] Y. Nomura, R. Hörlein, P. Tzallas, B. Dromey, S. Rykovanov, Z. Major, J. Osterhoff, S. Karsch, L. Veisz, M. Zepf, D. Charalambidis, F. Krausz, and G. D. Tsakiris, "Attosecond phase locking of harmonics emitted from laser-produced plasmas," Nature Physics **5**, 124–128 (2009).

[182] B. Dromey, D. Adams, R. Hörlein, Y. Nomura, S. G. Rykovanov, D. C. Carroll, P. S. Foster, S. Kar, K. Markey, P. McKenna, D. Neely, M. Geissler, G. D. Tsakiris, and M. Zepf, "Diffraction-limited performance and focusing of high harmonics from relativistic plasmas," Nature Physics **5**, 146–152 (2009).

[183] G. D. Tsakiris, K. Eidmann, J. M. ter Vehn, and F. Krausz, "Route to intense single attosecond pulses," New Journal of Physics **8**, 19 (2006).

[184] M. C. Kohler, C. Ott, P. Raith, R. Heck, I. Schlegel, C. H. Keitel, and T. Pfeifer, "High harmonic generation via continuum wave-packet interference," Phys. Rev. Lett. **105**, 203902 (2010).

[185] D. Bauer, P. Mulser, and W. H. Steeb, "Relativistic ponderomotive force, uphill acceleration, and transition to chaos," Phys. Rev. Lett. **75**, 4622–4625 (1995).

[186] A. I. Akhiezer and R. V. Polovin, "Theory of wave motion of an electron plasma," JETP **3**, 696 (1956).

[187] S. Chen, M. Rever, P. Zhang, W. Theobald, and D. Umstadter, "Observation of relativistic cross-phase modulation in high-intensity laser-plasma interactions," Phys. Rev. E **74**, 046406 (2006).

[188] P. Salieres, B. Carre, L. Le Deroff, F. Grasbon, G. G. Paulus, H. Walther, R. Kopold, W. Becker, D. B. Milosevic, A. Sanpera, and M. Lewenstein, "Feynman's Path-Integral Approach for Intense-Laser-Atom Interactions," Science **292**, 902–905 (2001).

[189] H. K. Avetissian, K. Z. Hatsagortsian, A. G. Markossian, and S. V. Movsissian, "Generalized eikonal wave function of a dirac particle interacting with an arbitrary potential and radiation fields," Phys. Rev. A **59**, 549–558 (1999).

[190] I. I. Rabi, "On the process of space quantization," Phys. Rev. **49**, 324–328 (1936).

[191] L. C. Allen and J. H. Eberly, *Optical Resonance and Two-Level Atoms* (Dover Pubn Inc, 1988).

[192] C. Cohen-Tannoudji, B. Diu, and F. Laloë, *Quantum Mechanics* (John Wiley & Sons, New York, 1977).

[193] P. Meystre and M. Sargent III, *Elements of quamtum optics* (Springer, Berlin, 1999), 3rd ed.

[194] N. Rohringer and R. Santra, "Resonant auger effect at high x-ray intensity," Phys. Rev. A **77**, 053404 (2008).

[195] "Los Alamos National Laboratory Atomic Physics Codes," (2000). See aphysics2.lanl.gov/cgi-bin/ION/runlanl08a.pl.

[196] J. Als-Nielsen and D. McMorrow, *Elements of modern x-ray physics* (John Wiley & Sons, New York, 2001).

[197] V. P. Krainov, "Ionization rates and energy and angular distributions at the barrier-suppression ionization of complex atoms and atomic ions," J. Opt. Soc. Am. B **14**, 425–431 (1997).

[198] C. Buth and R. Santra, "Theory of x-ray absorption by laser-dressed atoms," Phys. Rev. A **75**, 033412 (2007). arXiv:physics/0611122.

[199] E. Merzbacher, *Quantum mechanics* (John Wiley & Sons, New York, 1998), 3rd ed.

[200] M. Altarelli, R. Brinkmann, M. Chergui, W. Decking, B. Dobson, S. Düsterer, G. Grübel, W. Graeff, H. Graafsma, J. Hajdu, J. Marangos, J. Pflüger, H. Redlin, D. Riley, I. Robinson, J. Rossbach, A. Schwarz, K. Tiedtke, T. Tschentscher, I. Vartaniants, H. Wabnitz, H. Weise, R. Wichmann, K. Witte, A. Wolf, M. Wulff, and M. Yurkov, eds., *The Technical Design Report of the European XFEL*, DESY 2006-097 (DESY XFEL Project Group, Deutsches Elektronen-Synchrotron (DESY), Notkestraße 85, 22607 Hamburg, Germany, 2006).

[201] J. Arthur and *et. al*, *Linac coherent light source (LCLS): Conceptual design report*, SLAC-R-593, UC-414 (2002). www-ssrl.slac.stanford.edu/lcls/cdr.

[202] T. Pfeifer, Y. Jiang, S. Düsterer, R. Moshammer, and J. Ullrich, "Partial-coherence method to model experimental FEL pulse statistics," Opt. Lett. **35**, 3441–3443 (2010).

[203] E. L. Saldin, E. A. Schneidmiller, and M. V. Yurkov, "Statistical and coherence properties of radiation from x-ray free-electron lasers," New J. Phys. **12**, 035010 (2010).

[204] M. Jurvansuu, A. Kivimäki, and S. Aksela, "Inherent lifetime widths of Ar $2p^{-1}$, Kr $3d^{-1}$, Xe $3d^{-1}$, and Xe $4d^{-1}$ states," Phys. Rev. A **64**, 012502 (2001).

[205] R. Trebino, *Frequency-resolved optical gating: the measurement of ultrashort laser pulses* (Kluwer Academic Publishers, Boston, Dordrecht, London, 2000).

[206] F. Ferrari, F. Calegari, M. Lucchini, C. Vozzi, S. Stagira, G. Sansone, and M. Nisoli, "High-energy isolated attosecond pulses generated by above-saturation few-cycle fields," Nat. Photonics **4**, 875–879 (2010).

[207] A.-S. Morlens, P. Balcou, P. Zeitoun, C. Valentin, V. Laude, and S. Kazamias, "Compression of attosecond harmonic pulses by extreme-ultraviolet chirped mirrors," Opt. Lett. **30**, 1554–1556 (2005).

[208] K. T. Kim, K. S. Kang, M. N. Park, T. Imran, G. Umesh, and C. H. Nam, "Self-compression of attosecond high-order harmonic pulses," Phys. Rev. Lett. **99**, 223904 (2007).

[209] L. Poletto, F. Frassetto, and P. Villoresi, "Design of an extreme-ultraviolet attosecond compressor," J. Opt. Soc. Am. B **25**, B133–B136 (2008).

[210] G. Doumy, J. Wheeler, C. Roedig, R. Chirla, P. Agostini, and L. F. DiMauro, "Attosecond synchronization of high-order harmonics from midinfrared drivers," Phys. Rev. Lett. **102**, 093002 (2009).

[211] Y. Zheng, Z. Zeng, P. Zou, L. Zhang, X. Li, P. Liu, R. Li, and Z. Xu, "Dynamic chirp control and pulse compression for attosecond high-order harmonic emission," Phys. Rev. Lett. **103**, 043904 (2009).

[212] P. Zou, Z. Zeng, Y. Zheng, Y. Lu, P. Liu, R. Li, and Z. Xu, "Coherent control of broadband isolated attosecond pulses in a chirped two-color laser field," Phys. Rev. A **81**, 033428 (2010).

[213] M. C. Kohler, M. Klaiber, K. Z. Hatsagortsyan, and C. H. Keitel, "Phase-matched coherent hard x-rays from relativistic high-order harmonic generation," Euro. Phys. Lett. **94**, 14002 (2011). arXiv:1008.0511.

Acknowledgements

Zuallerst möchte ich meinem Doktorvater, Herrn Prof. C. H. Keitel, danken für die Aufnahme in seine Arbeitsgruppe, seine Förderung über die vergangenen Jahre, die Freiräume eigene Entscheidungen treffen zu können, für das in mich gesetzte Vertrauen, die exzellente wissenschaftliche Betreuung und die unentbehrliche Hilfe beim wissenschaftlichen Publizieren.

Vielen Dank an Herrn Prof. D. Dubbers für die Übernahme des Zweitgutachtens.

Ganz viel Dank geht an Karen Hatsagortsyan für die Ausbildung in theoretischer Physik, für seine Bereitschaft sich immer Zeit zu nehmen und mit großer Geduld gemeinsam Lösungswege zu suchen. Ich konnte von seinem enormen Fachwissen immens profitieren.

Thomas Pfeifer danke ich für die ergiebige Zusammenarbeit. Unser gemeinsames Projekt war die schönste und erfolgreichste Zeit während meiner Promotion, auch dank seinem eindrucksvollen physikalischen Gespür.

An Christian Buth für die früchtetragende Zusammenarbeit, für die vielseitige Unterstützung und das sorgfältige Korrekturlesen der Arbeit ein großes Dankeschön.

Für die tatkräftige Unterstützung von technischer und organisatorischer Seite in unserer Abteilung möchte ich mich bei Peter Brunner, Sibel Babacan und Vera Beyer bedanken.

Vielen Dank an unseren Bibliothekar Gernot Vogt für die prompte Bereitstellung der umfangreichen Literatur über die Jahre.

Danke an Heiko Bauke für unzählige Lösungshilfen bei Computerproblemen.

Ein ganz großes Dankeschön an die Korrekturleser der Arbeit: Dominika Becker, Jessica Drexler, Benjamin Galow, Katharina Goossen, Lea Herfs, Ben King, Michael Klaiber, Christian Müller, Christian Ott, Adriana Pálffy, Sandra Schmid, Bas Wegh, Isabella Zemanek.

Ein herzliches Dankeschön an die Laufgruppe um Claus Dieter, José und Klaus für die vielen schönen gemeinsamen Trainingseinheiten, ganz besonders für das gemeinsame Vorbereitungsprogramm auf den Heidelberger Halbmarathon.

Weiterhin möchte ich mich bei allen Kollegen am Max-Planck-Institut für Kernphysik für das angenehme Arbeitsklima bedanken. Ganz besonders bei meinen Bürokollegen Hsiang-Shun Chou, Héctor Castañeda Cortés, Gabor Darvasi, Hossein Ebadi und Matthias Ruf.

Zuletzt möchte ich meiner Familie danken, die alles erst ermöglicht hat.

Erklärung

Diese Arbeit ist von mir selbstständig verfasst worden, und ich habe keine anderen als die angegebenen Quellen und Hilfsmittel benutzt.

Heidelberg, 15.04.2011 .....

Unterschrift